VIBRATIONS
IN PHYSICAL SYSTEMS

VOLUME 31, No. 1

VPS VIBRATIONS IN PHYSICAL SYSTEMS

VPS VIBRATIONS IN PHYSICAL SYSTEMS

CONTENTS

Determination of the Sound Power Level of Modular Machines with Cyclic Operation Mode – Case Study

Bartosz JAKUBEK

Poznan University of Technology, Faculty of Mechanical Engineering,
3 Piotrowo St, 60-965 Poznan, bartosz.jakubek@put.poznan.pl

Roman BARCZEWSKI

Poznan University of Technology, Faculty of Mechanical Engineering,
3 Piotrowo St, 60-965 Poznan, roman.barczewski@put.poznan.pl

Abstract

The sound power level as a parameter characterizing a sound source, as opposed to the sound pressure level, should theoretically not depend on the place of measurement and distance from the source. Therefore, it is often used as a basis for comparing machines and equipment in terms of noise emissions. Manufacturers usually specify this parameter in the technical documentation or on the equipment. The sound power level is also a necessary parameter for modelling the natural and working environment in terms of acoustics. The standards for methods of determining the sound power level define three classes of accuracy depending on the method and environment of measurement. The paper outlines the problems associated with determining the sound power level of non-standard machines in situ. The case study concerns a machine, a modular SRP (shelf ready packaging) production system that can be part of an extensive production line. Specific for this type of machine is the coexistence of many local sources generating sound of different nature, cyclic mode of operation and the possibility to set different capacity.

Keywords: sound power level, in situ measurements, survey method, tray former, forming machine

1. Introduction

The sound power level as a parameter characterizing the sound source, as opposed to the sound pressure level, does not depend on the place of measurement and distance from the source. The obligation to determine and declare the sound power level L_{WA} of machines and devices rests with the manufacturers, provided that the equivalent A-weighted sound pressure level at the workplace exceeds 85 dB [1, 2]. However, this does not mean that no acoustic tests are carried out on devices that generate significantly lower noise levels. Wherever the recipient expects the product to work quietly, manufacturers can strive to reduce the noise emitted by the device. The results of such acoustic tests are usually confirmed in the manufacturer's declaration and pose a challenge to the competition. Biomedical devices such as a smoke evacuator [3] or nebulizer [4] can be examples.

The sound power level can be determined based on measurements of sound pressure, sound intensity or velocity of a vibrating surface [5]. The standards for methods for determining the sound power level define three classes of method accuracy depending on the method and measurement environment. These are: precision methods guaranteeing accuracy up to 0.5 dB, engineering methods - 1.5 dB and survey methods of 3 dB.

The choice of the method for determining the sound power level depends, among others, on:

- the stationarity of the emitted sound, in the case of non-stationary noise in terms of amplitude and frequency, a sufficiently long averaging time is required,
- the distance between the noise level emitted by the machinery and the acoustic background; this is important when testing machinery with a low level of vibro-acoustic emission [6] and when testing in rooms with a high level of background noise, it may be necessary to switch off other sound sources in the test room,
- the presence of many local sound sources in the tested machine (device) and their location relative to each other, if relocation of these sources is possible they should be placed close together, e.g. in the case of testing vacuum cleaners the main unit and the suction nozzle should be placed next to each other and such a system should be treated as one sound source [7, 8],
- the possibility of autonomous operation (without cooperating devices),
- the possibility of transport to rooms with acoustic and size adaptation; this concerns mainly large machines [9, 10].

The aim of the study was to outline problems with meeting the standard requirements when determining the sound power level L_{WA} of a modular machine, a tray former using the survey method [11], and to propose a way to solve these problems.

2. Test object and measuring room

The object of the study was a horizontal tray former FTHT 6. It is dedicated for erecting trays of different shape and dimensions using a hot melt (an adhesive). The former is able to work as an independent unit or as a part of goods flow system. The former is shown in Figure 1. Pink gradient was added in the picture to increase visibility of guards.
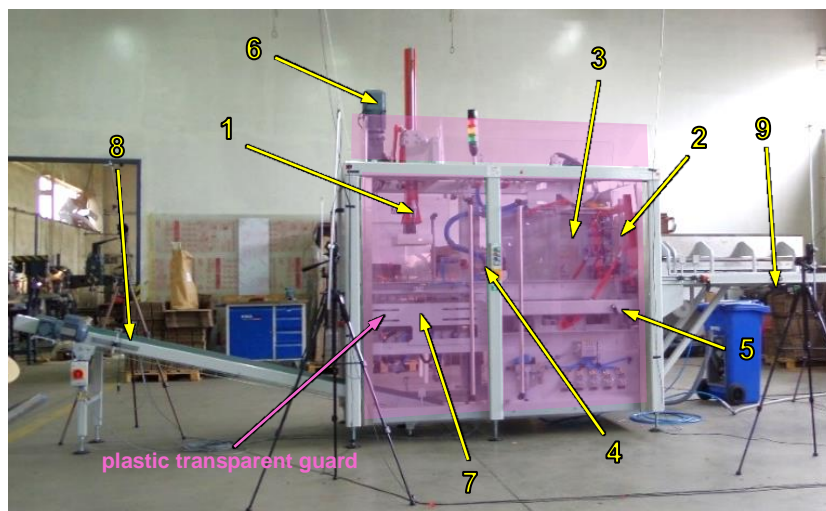

Figure 1. View of the FTHT6 former before starting noise measurements

The object is characterized by numerous local noise sources. They are:
1) a punch emitting impulse noise associated with the cardboard forming process,
2) suction cups for cardboard manipulator,
3) manipulator movement (low-frequency noise),
4) gluing system (broadband noise),
5) a servo drive for cardboard travel,
6) manipulator drives (asynchronous motors with fixed or variable speed gears),
7) a bender and pneumatic clamp (broadband impulse noise).

When determining the L_{WA} in accordance with ISO 3746 [11], it is important to consider the influence of the measurement room in the following aspects: the reflected sounds and the level of background noise.

The former is connected with a conveyor belt (Fig. 1. No. 8) which receives finished trays and in its vicinity, in the measuring room, there is a compressor (Fig. 1. No. 9) supplying the machine with compressed air. The belt and compressor are functionally linked to the former. The presence of this type of auxiliary devices being external sound sources requires verification whether they have an impact on the results of noise measurements and the determined sound power level. While the operation of the conveyor belt drive (see Fig. 1.) does not affect the value of the background noise correction K_1, the influence of the compressor operating nearby was significant. For this reason, the air compressor was switched off during the test cycle and the former was fed with compressed air accumulated in the compressor tank.

The K_2 correction determining the effect of reflected sounds in the test room, based on the experimentally measured reverberation time, was 3.8 dB. The application of the approximate method for determining the mean sound absorption coefficient $\alpha = 0.15$ (for a room with furniture; rectangular machinery room; rectangular industrial room), however, gives a higher result equal to 5.2 dB. The application of this simplification results in an overestimation of the K_2 value by 1.4 dB and consequently an underestimation of the sound power level.

Due to the high level of background noise and relatively high probability of numerous acoustic events with significant sound levels in the case under consideration, determining the sound power level of the former required switching off all the devices installed in the measuring room. In this case, measurements were carried out in the room after production had stopped. This allowed to obtain a distance between the noise level of the former and the background noise level of above 20 dB and to assume the value of $K_1 = 0$ dB. Such a procedure is not always possible under *in situ* measurements [12]. However, the aforementioned individual components of the machine work sequentially, and some of them change their position within the machine. This specific design and operation of the former in space requires a relatively long averaging time to obtain reliable measurement results. Moreover, it makes practically impossible to use the sound intensity measurements [13, 14], and in particular the sweeping method [15] to determine the L_{WA}.

3. Testing methodology

Taking into account the conditions described in chapter 2, it was only possible to apply the survey method for determining L_{WA}. However, during the determination of the L_{WA} of the former some issues were encountered related to:

- high level of background noise,
- determination of the equivalent sound absorption area of the room – A,
- the presence of additional sound-emitting equipment, indispensable in the operation of the former,
- dimensions of the reference box,
- determination of the measurement surface and space,
- selection of measuring distance – d,
- the non-stationary in the sense of amplitude and frequency emitted sound related to cyclical machine operation,
- high efficiency of the machine (limited test duration due to the number of trays produced),
- the presence of numerous local impulse noise sources with different spectral composition and sound level in the machine.

The tested object should be inscribed in the reference box. When determining the dimensions of the reference box, those elements which are not significant sound emitters may be omitted [11]. The dimensions of the reference box are marked on the CAD model and are shown in Figure 2.

$l_1 = 2500$ mm
$l_2 = 1500$ mm
$l_3 = 2500$ mm
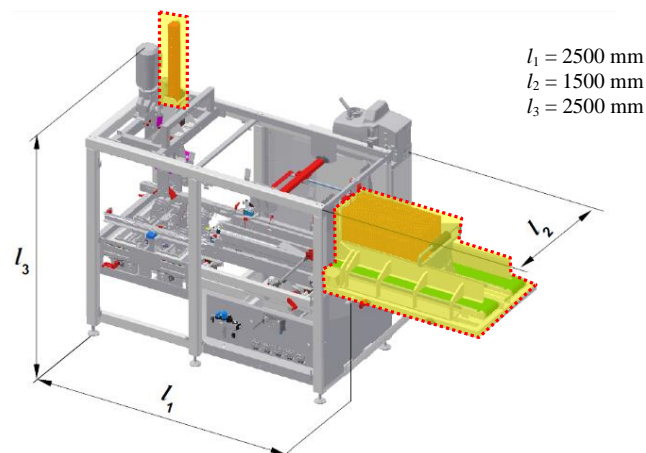
Figure 2. CAD model of the FTHT 6 former with the dimensions of the reference box

In the case of the FTHT 6 former, the punch guide, which is movable, and the cardboard feeder on the right hand side are omitted. The feeder is not a source of noise and the cardboard boxes placed thereon slightly suppress the sound. Both omitted elements have been highlighted in Figure 2.

When determining the L_{WA} by the survey method, it is recommended that the measuring distance d is equal to 1 m or more. In justified cases, however, it can be reduced

to 15 cm [11]. The positions of the microphones (measuring points) and the measuring surface with dimensions are given in Figure 3. The adoption of the measuring distance d is a key problem determining the size of the measuring surface, taking into account the influence of reflected sounds and the number of measuring points. In the described case, the measuring distance $d = 1.5$ m was adopted. It is the shortest possible distance at which it is possible to carry out measurements in eight points according to the procedure for the determination of the L_{WA} using the survey method (according to ISO 3746 [11]).

Dimension	Value
l_1	2.50 m
l_2	1.50 m
l_3	2.50 m
a	2.75 m
b	2.25 m
c	4.00 m
d	1.50 m
h_1	2.00 m
S	104.75 m^2

Acoustic parameters of the testing room:
$\alpha = 0.247$
$A = 300.2$ m^2

Figure 3. Arrangement of measuring points on the measuring surface

The view of the former and testing equipment prepared for measurements is shown in Figure 4. In the picture, the microphones are marked with yellow dots.

Figure 4. View of the tested object - FTHT 6 former, after preparation for sound pressure measurements (measurement points 3 and 4 are behind the former)

Increasing the distance d increases the area of the measuring surface S. It is important when determining the L_{WA}, which in this case was determined from the formula:

$$L_{WA} = 10\log_{10}\left[\frac{1}{8}\sum_{i=1}^{8}10^{0.1L_{pi}}\right] - 10\log_{10}\left(1 + 4\frac{S}{A}\right) + 10\log_{10}\frac{S}{S_0} \tag{1}$$

where: L_{pi} – A-weighted sound pressure level at the i-th measuring point,
S – measuring surface area,
S_0 – reference surface area of 1 m^2,
A – the equivalent sound absorption area of the room.

The above formula does not take into account the K_1 correction since its value was 0 dB. It should also be noted that if the sound power level is determined by the survey method, the K_2 correction (second component of formula 1) must meet the relationship: $K_2 < 7$dB. Adopting $d = 1.5$ m and taking into account the size of the measuring area and the sound absorption of the measuring room guaranteed that this condition was met, $K_2 = 3.8$ dB.

The measurement time was 80 s each time, which guaranteed that at least 30 forming cycles were recorded. The adoption of such a measurement time (averaging) was due to the non-stationary, cyclical operation of 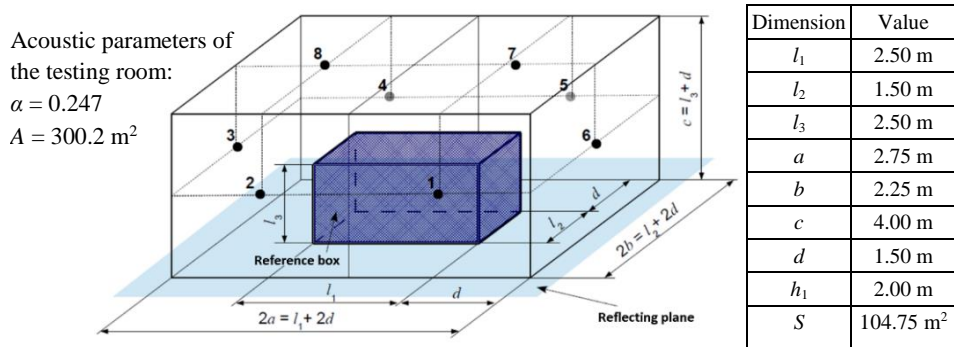the machine and the limited supply of accumulated compressed air in the compressor tank. As part of the study, spectral analyses were performed simultaneously: octave and short-time ones. This approach also makes it possible to determine the directionality of the noise emitted by the former. The tests were carried out for 4 different machine capacities measured in number of cycles (trays produced) per minute: 25, 31.5, 35.8, 39.8. The capacity depends, among other things, on the complexity of a tray or packaging (e.g. number of folds). Under actual production conditions, the folding rate of the cartons must be adapted to the rate of production of a flow production line.

Due to the high capacity of the former and the resulting need to reduce testing time, it was advisable to use a microphone array for synchronous recording. An alternative approach could be to use a microphone antenna [16]. However, this solution duplicates the disadvantages of iterative measurements when testing objects that generate non-stationary noise. However, the main reason for the 8-channel synchronous pressure recording would be in case of other solutions the need to guarantee a huge amount of prefabricated elements and the impossibility of receiving finished trays in case of an former not connected to the process line.
The following were used to record, measure and analyse noise:
- 8 free field microphones Roga RG-50 ICP®,
- 8-channel recording unit TEAC LX–10,
- dedicated recording, measurement and analysis application developed in the DASYLab (*Data Acquisition System Laboratory*) environment.

4. Summary of research results and discussion

The test results showing the specifics of the noise emitted by the former relate to the rated operation of the machine at 25 cycles per minute.

The fact that the tested former generates non-stationary noise is exemplified by the changes in instantaneous sound pressure values recorded above the machine (measuring point 7) shown in Figure 5. The figure presents changes in the instantaneous peak and rms sound pressure values at the point where the average instantaneous peak pressure $\bar{p}_{IPEAK}$ defined in [17] was the highest.
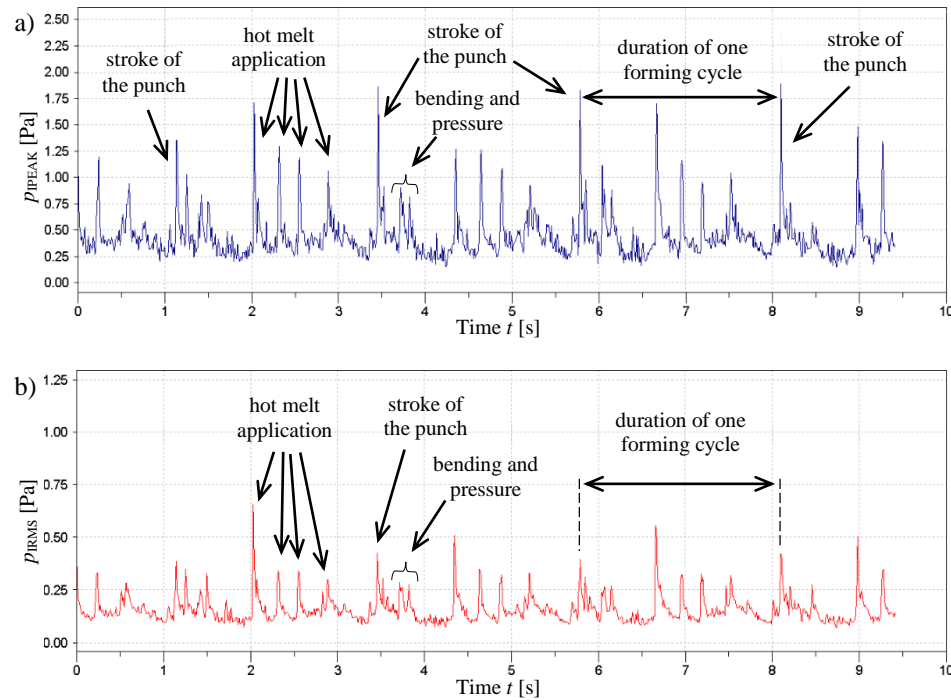
Figure 5. Instantaneous values a) peak, b) rms of sound pressure measured at measuring point No. 7 above the FTHT6 former at 25 cycles/min

It is easy to identify subsequent work cycles on the charts. The highest instantaneous peak sound pressure values p_{IPEAK} (see Fig. 5a) accompany punch strokes. After the punch stroke, the cardboard is bent and the pneumatic pressure is applied. Simultaneously with the working movement of the punch, the cardboard manipulator places another cardboard blank on the conveyor. When moving hot melt is sprayed onto the cardboard at the bonding point, which takes place each time about 1 second after punching. Different values of sound pressure at the same events in successive cycles of the former confirm the need to adopt such time of signal recording that covers a greater number of cycles and to average the results. It should be noted that increasing the capacity of the machine consists mainly in shortening the intervals between component operations.

The recorded signals allowed not only to determine the sound power level L_{WA}, but also to determine the octave and average spectra of sound pressure levels and A-sound

levels sequentially. Figure 6 shows the sound levels for eight measuring points located on the measuring surface (see Fig. 3.) - averaging time: 80s.
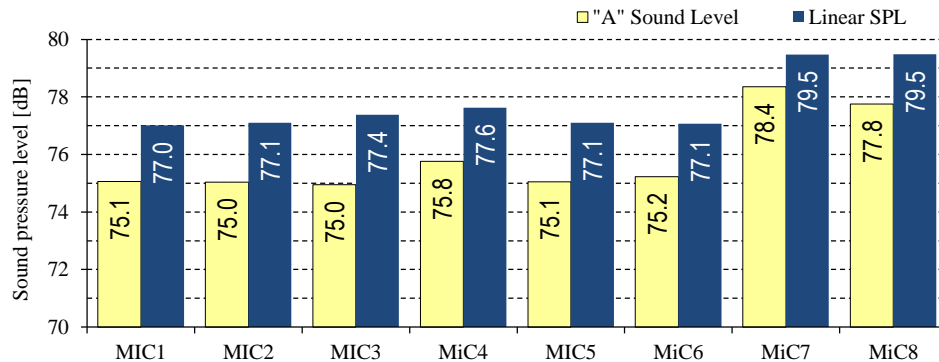
Figure 6. Linear (uncorrected) sound pressure level and A-weighted sound level at measuring points on the measuring surface

The highest pressure levels were recorded at measurement points 7 and 8. This is due to the lack of covers at the top of the former. Transparent plastic guards fitted in the outer frame of the former (see Figure 1, pink gradient), in addition to their safety function, reduce the noise propagation outside the machine. The pressure level at measurement point No. 6 is very close to the levels at points 1 - 5, which confirms the correctness of omitting the cardboard feeder when determining the dimensions of the reference cuboid.

The pressure levels averaged on the measuring surface in octave bands are given in Figure 7.
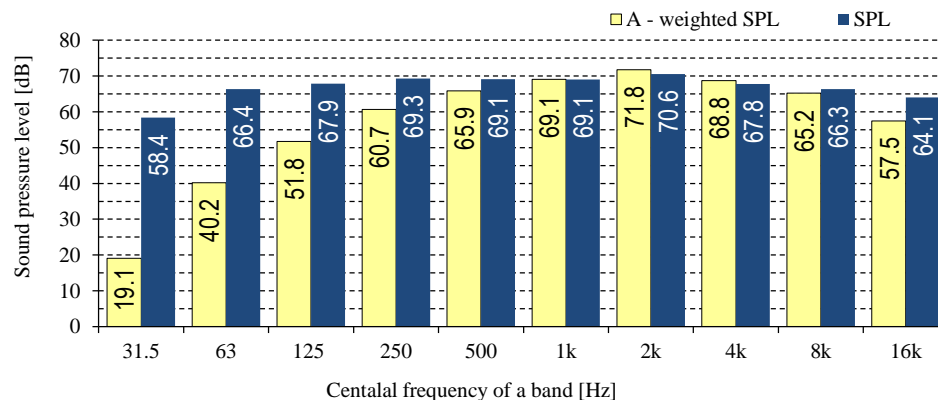
Figure 7. Octave spectrum - averaged sound pressure levels on the measuring surface (uncorrected and A-weighted) in the octave bands

From the octave spectrum it can be concluded that the machine generates broadband noise. The highest levels were recorded in the band of the highest sensitivity of the human hearing organ. This was mainly due to the operation of pneumatically driven systems.

The second important aspect of the research was to determine the relationship between the capacity parameter – cycles per minute of the machine and the sound power level. The determined sound power levels as a function of the set capacity are shown in Figure 8.
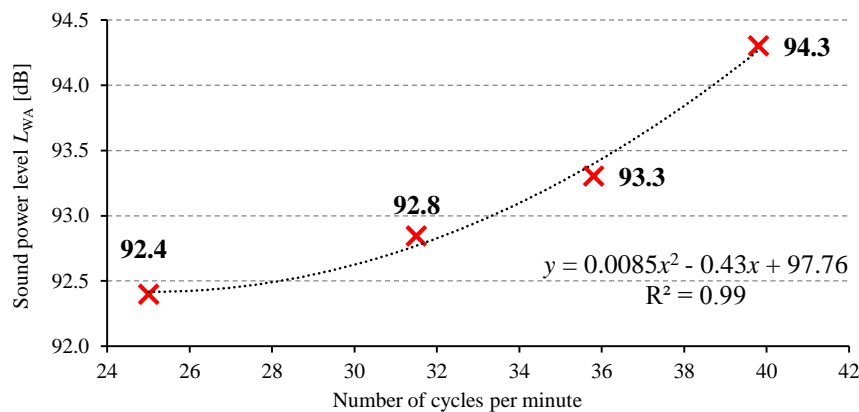
Figure 8. The sound power level of the FTHT6 former as a function of the number of cycles per minute

It should be noted that the noise generated by individual events during operation of the former is almost constant and does not depend on the number of cycles per minute (performance). However, as a consequence of reducing the duration of the work cycle (increasing the number of short-time events per unit of time), the average level of emitted noise increases. Analyzing the data (Fig. 8) it can be stated that the sound power level of the FTHT6 former depends quadratically on the capacity and increases with its increase (coefficient of determination R^2 is 0.99).

This relationship therefore makes it possible to estimate the sound power level for various forming capacities. Another benefit of conducting the recording according to the presented methodology is obtaining a set of data which additionally enables to determine the directivity of noise emitted by the former. On this basis it is possible to identify noise hazard zones and safety zones and to optimize machine construction in acoustic aspect. Sequential short-time parameterization and analysis gives information about the duration of individual events and their spectral composition (flows, knocks, gluing, impulse strokes - benders). Such a set of results can be the basis for undertaking actions to minimize the emission of noise by the machine by e.g. installation of an additional housing or suppressing noise with sound-absorbing materials and identification and silencing components having a key share in the final L_{WA} value. In order to formulate conclusions from the research carried out it was helpful to compare the conditions of conducting sound pressure measurements for the purpose of determining the L_{WA} by means of a survey method for typical machines / devices with - in the discussed case - a specific machine, which is a former. This comparison is shown in Table 1.

Table 1. Comparison of measurement conditions for the purposes of determining L_{WA} in a typical and the discussed cases

	Typical case	This case – Horizontal tray former
Sound source	1 or more placed close together	Multi-source design, sources can change location in space
Auxiliary devices	Do not occur	Necessary verification of the significance of the influence of auxiliary equipment
Operating mode	Continuous operation	Cyclical operation, possible capacity change
Emitted noise	Stationary	Transient
Restrictions on working / testing time	None	Time of work / research limited by the availability of the semi-finished product and receipt of finished products
Background noise	Background level at least 10 dB lower than the average sound level on the measurement surface	Tests after stopping the work of other devices in the measuring room
Type of measuring surface	Hemisphere or parallelepiped	Parallelepiped
Measuring distance d	d not less than 0.15 m, preferably 1 m	d = 1.5 m – determined by the dimensions of the machine
Number of measuring channels	At least 1	The need for synchronous multi-channel signal recording
Number of measuring points	Depends on the type of measuring surface and distance d	Limited by the number of measurement channels for synchronous recording (8 measurement points)
Spectral composition of the noise	Quasi-stationary	Non-stationary, cyclically variable in time
Measuring equipment	At least 1 sonometer	A set of 8 microphones, an 8-channel signal recorder and signal analysis system
Possibility to relocate the machine to a room with acoustic adaptation	Usually, yes	No
Length of the recorded signal	No requirements, just a few seconds	Possibly long recorded signal, at least 30 cycles
Environmental correction K_2	The average sound absorption coefficient α can be read from the table	Determined experimentally on the basis of measurement of reverberation time
Reference box	It is tangential to the outer edges of the device	Determined excluding the machine parts which are not sources of noise

Generally, it is required that the sound power level L_{WA} declared by manufacturers be determined under the most stable operating conditions [11]. Due to the specifics of the former, providing one L_{WA} value does not give complete information about the acoustic parameters of the machine. The emitted noise may change not only due to the set capacity but also depending on the equipment installed (different types of cartons). It is necessary to consider that the technical documentation regarding noise emissions should contain not only one number - L_{WA}, but a set of L_{WAi} values for different variants of capacity. Providing extended information for this class of machines will enable more detailed design of acoustic climate in the work environment [18].

When determining the sound power level L_{WA} of this class of machines, with many local noise sources and cyclical operation mode, it is important to:

- record signals synchronously at all measuring points,
- analyze the stationarity of the signal to determine the time of recording (averaging) the signal,
- select the measuring distance d based on two criteria: so that d is as small as possible and the number of measuring points does not exceed the possible number of channels for synchronous signal recording,
- omit the parts of the machine which are not related to noise emissions when determining the reference box,
- determine additionally the equivalent sound absorption area of the room A based on the measurement of reverberation time in order to obtain more reliable results.

5. Summary

It is not advisable to include in the technical documentation the sound power level L_{WA} of machines with cyclic operation mode with the possibility of setting capacity (CPM) as a single value. Moreover, this does not provide a basis for reliable forecasting of acoustic interactions and modelling of the environment or acoustic climate in industrial halls. The sound power level emitted by the former can have different values depending on the equipment installed (different types of cardboard trays) or its capacity. It should be considered to provide extended information on the L_{WA} for different accessory variants, capacities and types of formed packaging in the technical documentation. The observations from the acoustic testing of the former can be useful to teams testing machines with similar design and functional characteristics. During testing, it is important to take into account additional accessories and equipment emitting noise which are essential for the proper functioning of the device. It is worth noting that if the influence of these devices cannot be omitted, we may be dealing with a DESS (Device with Extensive Soud Sources) class source.

Acknowledgment

References

1. Directive 98/37/EC of the European Parliament and of the Council of 22 June 1998 on the approximation of the laws of the Member States relating to machinery.
2. J. Jacques, *European standardization in the field of noise with special focus on machines and workplaces*, Bezpieczeństwo Pracy, **5** (2004) 27 – 32 (in Polish).
3. B. Jakubek, R. Barczewski, *Determination of acoustic parameters of devices with extensive sound sources*, Vibrations in Physical Systems, **27** (2016) 129 – 134.
4. B. Jakubek, W. Rukat, K. Grochalski, *The noise of biomedical devices for domiciliary use on the example of a nebulizer*, Vibrations in Physical Systems, **29** (2018) 2018017-1 – 2018017-6.

5. ISO 3740:2019, *Acoustics — Determination of sound power levels of noise sources — Guidelines for the use of basic standards.*

6. R. Barczewski, B. Jakubek, *Problems of in-situ vibroacoustic testing of low-vibroactive devices*, Vibration in Physical Systems, **25** (2012) 59 – 64.

7. IEC 60704-2-1:2014; *Household and similar electrical appliances. Test code for the determination of airborne acoustical noise. Particular requirements for vacuum cleaners.*

8. W. Rukat, B. Jakubek, A. Madej, *The noise emitted by a vacuum cleaner treated as a device with extensive sound sources*, Vibrations in Physical Systems, **29** (2018) 2018015-1 – 2018015-8.

9. J. Karel, F. Monhart, *Noise measurement diagnostics for large electric machines*, Euronoise 2018 the 11th European Congress and Exposition on Noise Control Engineering - Conference Proceedings (2018) 757 – 763.

10. C. Tomozei, A. Astofli, V. Nedeff, G. Lazar, *Noise sources characterization inside and outside factory*, Environmental Engineering and Management Journal, **3** (2012) 701 – 708.

11. ISO 3746:2011, *Acoustics – Determination of sound power levels of noise sources using sound pressure – Survey method using an enveloping measurement surface over a reflecting plane.*

12. M. Aliabadi, R. Golmohammadi, A. Ohadi, *Empirical comparison of the in situ methods for determining sound power of typical embroidery machine located in industrial workroom*, International Journal of Occupational Hygiene, **5**(3) (2013) 89 – 95.

13. S. Weyna, *Effective Diagnostic of Local Noise Sources with Acoustic Imaging*, Vibrations in Physical Systems, **30**(2) (2019) 2019201-1 – 2019201-8.

14. B. Jakubek, R. Barczewski, M. Tabaszewski, *Localization of noise sources in electric cookers based on sound pressure and intensity measurements*, Vibrations in Physical Systems, **30**(2) (2019) 2019223-1 – 2019223-14.

15. ISO 9614-2:1996 *Acoustics — Determination of sound power levels of noise sources using sound intensity — Part 2: Measurement by scanning*

16. G. Bogisławski, J. M. Kopania, P. Gaj, K. Wójcik, *Determination of Sound Power Level by Using a Microphone Array and Conventional Methods*, Vibrations in Physical Systems, **30**(1) (2019) 2019139-1 – 2019139-8.

17. B. Jakubek, R. Barczewski, *The influence of kinematic viscosity of a lubricant on broadband rolling bearing vibrations in amplitude terms*, Diagnostyka, **20**(1) (2019) 93 – 102.

18. D. Augustyńska, *Strategy for protecting employees against noise according to new European and national legislation*, Bezpieczeństwo Pracy, **3** (2006) 4 – 7 (in Polish).

Influence of Mechanical and Electromagnetic Phenomena on Electric Motor Vibrations in Different Power Supply Options

Mateusz WRÓBEL

Poznan University of Technology, Faculty of Mechanical Engineering,
3 Piotrowo St, 60-965 Poznan, mateusz.wrobel@put.poznan.pl

Roman BARCZEWSKI

Poznan University of Technology, Faculty of Mechanical Engineering,
3 Piotrowo St, 60-965 Poznan, roman.barczewski@put.poznan.pl

Bartosz JAKUBEK

Poznan University of Technology, Faculty of Mechanical Engineering,
3 Piotrowo St, 60-965 Poznan, bartosz.jakubek@put.poznan.pl

Wojciech RUKAT

Poznan University of Technology, Faculty of Mechanical Engineering,
3 Piotrowo St, 60-965 Poznan, wojciech.rukat@put.poznan.pl

Abstract

Results of research about influence of mechanical and electromagnetic phenomena on electric motor vibration in different supply options has been shown in this paper. Three different supply options have been taken under consideration: typical star connection, single-phase connection with work capacitor and connection through an inverter. Vibration signals recorded on electric motor end shield and frame has been digitally processed using Multi-Synchronous Averaging (MSA). This technique allowed to decompose total vibration signal into signals associated with mechanical and electromagnetic phenomena occurring in electric motor. The comparison of rms values and spectra shapes of total and decomposed vibration signals has been made. Energy shares of previously mentioned phenomena in vibration signal for different supply options has been also estimated.

Keywords: electric motor, vibration, supply, star, single-phase, inverter, multi-synchronous averaging

1. Introduction

Asynchronous electric motors (AEM) are used as drive units in over 90% of machinery and devices [1, 2]. The common use of this type of motors is due to their reliability, simplicity of construction and a small number of elements susceptible to mechanical damage (mainly rotor and roller bearings), as well as a relatively low price. As a result of the widespread use of electric motors, it is important to keep them in good technical condition and to reduce the number of defective units released on the market. In practice, various techniques and methods are used to test electric motors, such as specialist electrical measurements, e.g. MCSA method (Motor Current Signature Analysis) [3, 4], specialized electric analyses and measurements [4-6], measurements and analyses of vibrations [7, 8] and noise [9, 10], measurements and analyses of magnetic field [11, 12], thermal measurements [13, 14] and others [15].

Defects and damage of asynchronous electric motors can affect both mechanical and electrical parts. Rolling bearing damage, rotor unbalance, misalignment and bending of the motor shaft can occur in the mechanical part. Furthermore, the damage and defects of the electrical part may include: inter-winding short circuits, interruption of stator windings, connection errors and occurrence of undesirable electromagnetic phenomena [16, 17]. Each of the above-mentioned defects and damage affect motor vibrations to varying degrees. Usually the intensity of vibrations recorded on the frame or end shields may indicate the degree of damage and the general technical condition of the motor. Therefore, the vibration signal can be used as a source of information on the technical condition of the electric motor for post-production testing and operational diagnostics.

On the other hand, vibrations resulting from electromagnetic phenomena occurring in electric motors can be largely related to the way the motor is connected to the power supply. In diagnostic applications which use vibrations recorded on the motor frame to assess the technical condition of electric motors it is important to determine the signal components associated with defects or damage to individual motor elements which are movable mechanical parts (e.g. bearings, rotor) and those related to electrical phenomena as well as the way of operation and construction of electromagnetic circuits (slot frequency, magnetostriction phenomenon).

The aim of the research presented in this article was to show qualitative (spectral composition) and quantitative (rms values of motor frame and end shield vibration acceleration) differences resulting from the change in the way the engine is powered. The knowledge of these conditions can be a starting point for the development of diagnostic methods basing on the measurement and analysis of vibroacoustic signals used in both post-production and operational diagnostics. The tests were carried out for the following types of three-phase asynchronous electric motor connections:

- direct star connection to a three-phase power supply; this type of connection is used in the case of continuous operation without the possibility of speed control, however, it is characterized by high starting current,
- connecting a three-phase motor as a single-phase motor using a run capacitor; it enables continuous operation without the possibility of speed control; this solution does not allow to achieve the rated engine power, there is also an undesirable effect in the form of increased engine temperature,
- connection to a three-phase network via an inverter; it makes possible to control the engine rotation speed.

Application of Multi-Synchronous Averaging (MSA) technique allowed to separate the vibration signal into signals related to mechanical and electromagnetic phenomena [18, 19]. The results of decomposition were the basis for estimating the energy share of these phenomena for different options of motor power supply. It also shows to what extent this share depends on the location of vibration transducers (frame, end shield).

2. Tested electric motor and its power supply options

The object of the research was a three-phase asynchronous electric motor type Sh71-4A. The view of the motor with vibration acceleration sensors and an eddy current sensor (tachometer probe) is shown in Fig. 1. The motor is mounted on a concrete block with a mass of 12 kg. Between the motor feet and the block and between the block and the ground there were rubber spacers. Their task was to separate vibrations from the ground. The basic technical parameters of the tested motor are shown in Tab. 1.

Table 1. Basic technical parameters of the tested asynchronous electric motor type Sh71-4A

Rated power	0.25 kW
Supply voltage (Δ / Y)	230 / 400 V
Rotation speed	1380 rpm
Efficiency	66 %
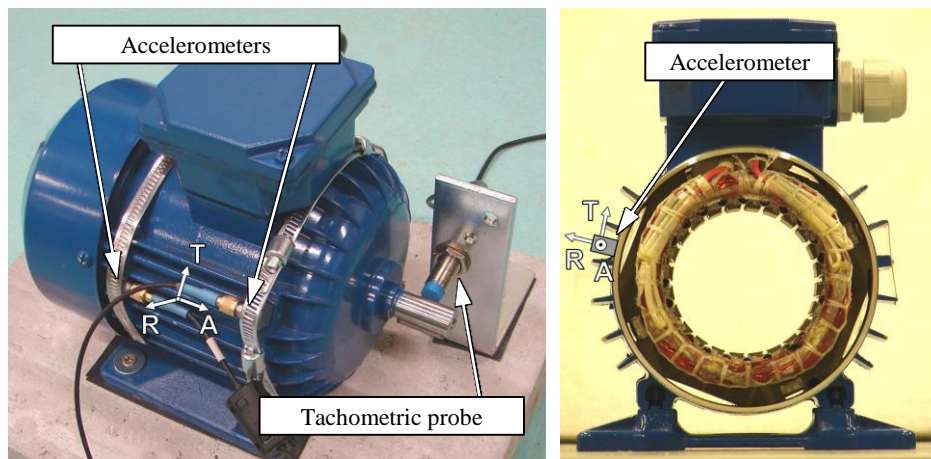
Figure 1. Arrangement of accelerometers and marking of measuring directions as well as a view of the motor frame after dismounting of end shields and the rotor with marked place of mounting of the accelerometer

Fig. 2 shows three alternative ways to connect the motor to the power supply: a typical three-phase star connection, a connection via an inverter and a connection as a single-phase motor with a run capacitor.

a) typical star connection   b) connection using inverter   c) one phase connection
with work capacitor
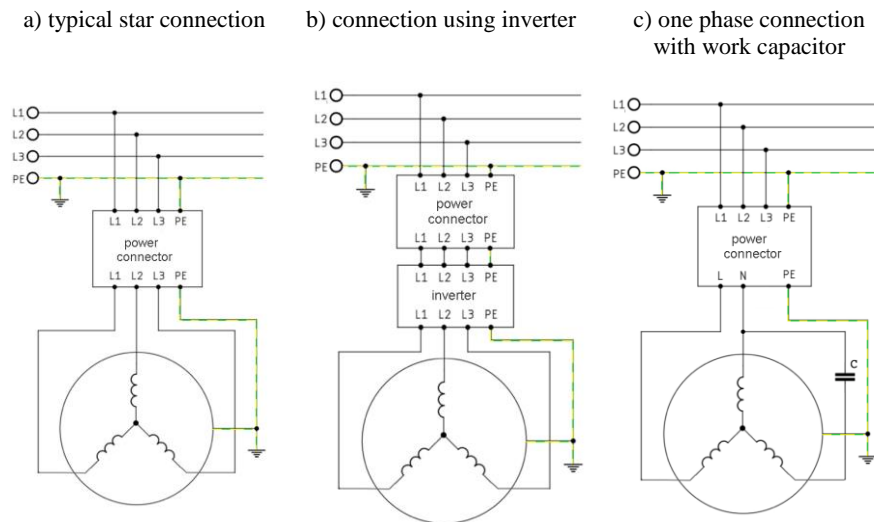
Figure 2. Power supply options of the tested AEM

3. Research methodology

During the tests, synchronous recording of vibrations of the motor frame and the end shield was carried out for each of the previously mentioned types of connections. Vibration accelerations were recorded using two DYTRAN 3023M2 triaxial accelerometers. One of the sensors was mounted on the front end shield and the other on the motor frame. The experiment conducted in this way made it possible to determine the impact of changing the power supply option on vibrations in these locations and in individual directions. Fig. 1b shows the places where the stator has no contact with the motor frame. An accelerometer was mounted at one of these points.

Three directions of vibration recording were adopted: radial R (normal to the frame), tangential to the frame T and axial A (Fig. 1a). The measurement chain was supplemented with dedicated electronic devices for measuring the rotational frequency of the rotor and for tracking the frequency of the 230V power supply. These signals were used as synchronizing signals in the process of multi-synchronous decomposition. The vibration acceleration signal and the tachometer and supply frequency signals were recorded synchronously using TEAC LX-10 8-channel data recording system. The application for recording and analysis of vibration signals was developed in the DASYLab[1] environment. A diagram of the measurement chain is shown in Fig. 3.

---

[1] DASYLab – Data Acquisition System Laboratory
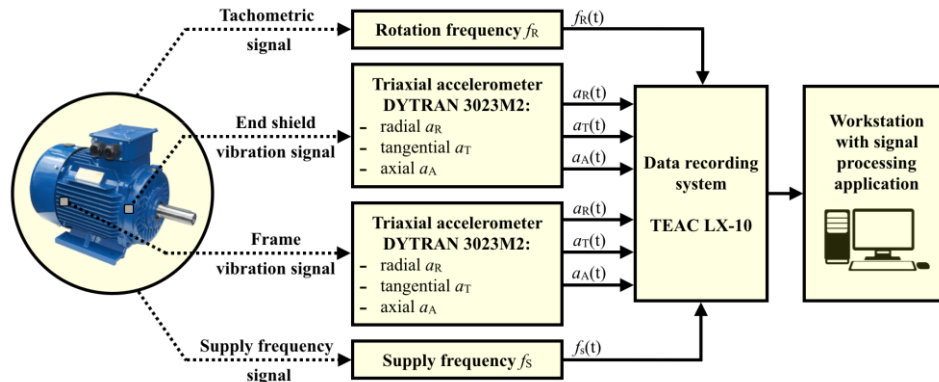
Figure 3. Diagram of the measurement chain

The vibration signal coming from an accelerometer mounted on the motor frame or end shield can be treated as a superposition of signals related to phenomena of mechanical nature (synchronous with rotor frequency f_r), electromagnetic nature (synchronous with mains frequency f_s), as well as components non-synchronous with f_s and f_r and noise. The form of acceleration of such a signal can therefore be written as:

$$a(t) = a^M(t) + a^E(t) + a^N(t), \tag{1}$$

where:

$a(t)$ – recorded vibration acceleration signal,
$a^M(t)$ – signal components related to mechanical phenomena (synchronous with f_r),
$a^E(t)$ – signal components related to electromagnetic phenomena (synchronous with f_s),
$a^N(t)$ – signal components non-synchronous with f_s and f_r and noise.

In the discretization process (ADC), the signal described by formula 1 takes the form of a time series:

$$a_i = a_i^M + a_i^E + a_i^N, \tag{2}$$

where:

i – consecutive number of a signal sample.

Multi-synchronous averaging (MSA) was used for decomposition of vibration signals [18, 19]. The simplified idea of MSA is shown in Fig. 4.
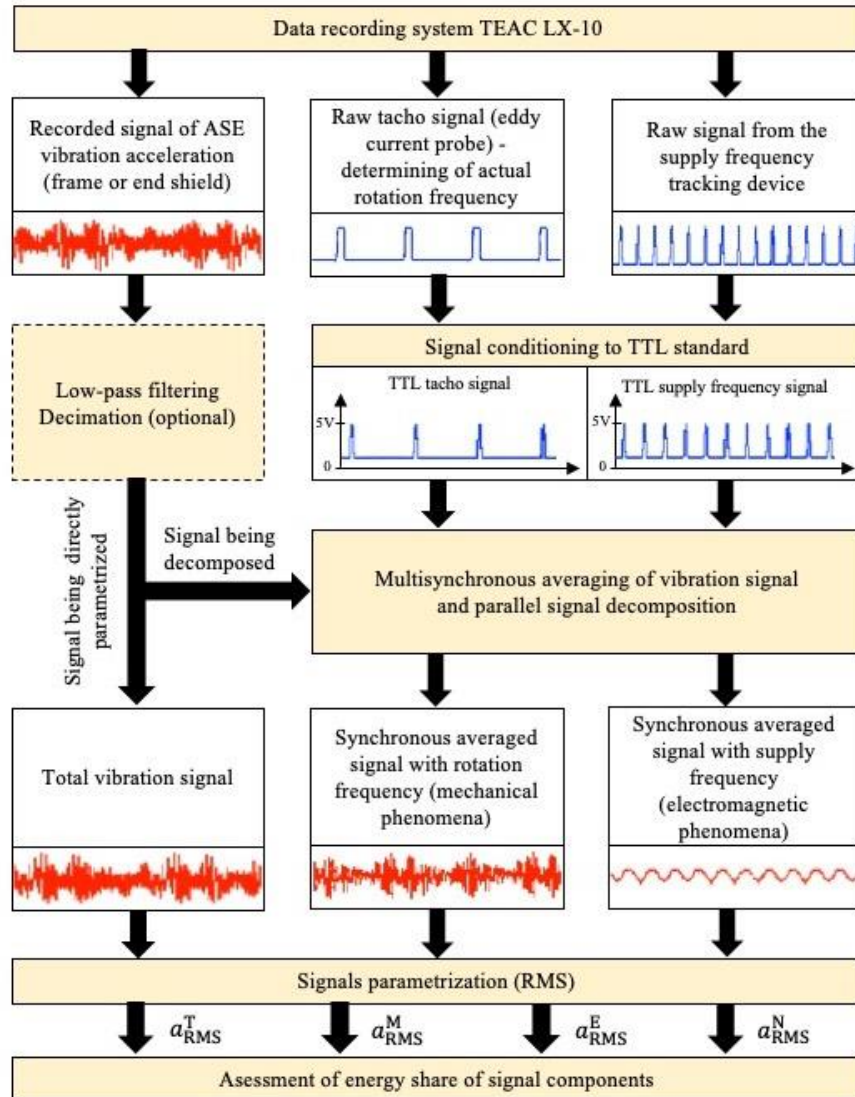
Figure 4. Simplified idea of decomposition of vibration acceleration signals of an asynchronous electric motor by the multi-synchronous averaging technique (MSA)

MSA enables multi-threaded signal decomposition and obtaining mono-periodic polyharmonic signals a_i^M and a_i^E. An example of functioning of the MSA procedure and reduction of non-synchronous components with f_s and f_r is shown in Fig. 5, which illustrates changes in spectral composition observed in subsequent iterations of synchronous averaging of signals.

a) synchronization with rotation frequency (f_r)   b) synchronization with supply frequency (f_S)
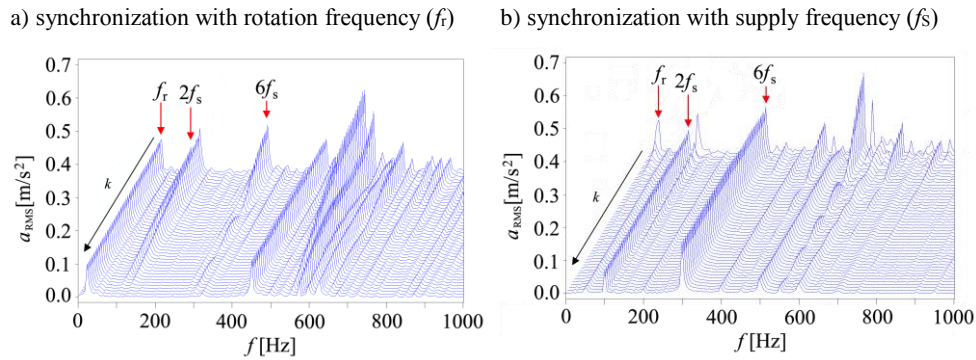
Figure 5. Changes in the spectral composition of vibration acceleration signals averaged synchronously; process synchronized with the supply frequency f_s and rotational frequency of the rotor f_r (k - subsequent iterations of synchronous averaging)

The effective reduction of the $2f_s$ and $6f_s$ frequency components (non-synchronous with f_r) is clearly visible in Fig. 5a, while the reduction of the f_r frequency component is observed in Fig. 5b for averaging synchronization with the f_s frequency. To synchronize the decomposition process, the tachometric signal (associated with f_r) and the supply frequency signal (f_s) were used respectively. In the process of synchronous averaging we obtain signal components $\bar{a}_j^M$ and $\bar{a}_j^E$ representing signals a_i^M and a_i^E in the form of a time series with a finite number of samples $j = 0, 1, ..., N - 1$. The correctness of such mapping increases with the number of k ($k = 1, 2, ..., K$) averaged sequences in the MSA process. The number of averaged K sequences can be determined arbitrarily assuming the desired reduction of non-synchronous components and noise in the averaged signal according to the relationship [20]:

$$K > \left(\frac{1}{R}\right)^2 \tag{3}$$

where:

R – assumed reduction of noise and non-synchronous components (e.g. $R = 0.01$).

Synchronously averaged signals associated with f_r and f_s can be written as:

$$\bar{a}_j^M = \frac{1}{K}\sum_{k=1}^{K} a_{k,j}^M \; ; \; \bar{a}_j^E = \frac{1}{K}\sum_{k=1}^{K} a_{k,j}^E , \tag{4}$$

where:

k – consecutive number of sequence of the signal to be averaged ($k = 1, 2, …, K$),
j – signal sample number in sequences ($j = 0, 1, …, N – 1$),
N – number of signal samples in the sequences of the signals to be averaged.

In the next processing step, the rms values of the signal subjected to decomposition a_i and signals $\bar{a}_j^M$ and $\bar{a}_j^E$ synchronously averaged are determined:

$$a_{RMS}^T = \sqrt{\frac{1}{L}\sum_{i=0}^{L-1} a_i^2} \; ; \; a_{RMS}^M = \sqrt{\frac{1}{N}\sum_{j=0}^{N-1} (\bar{a}_j^M)^2} \; ; \; a_{RMS}^E = \sqrt{\frac{1}{N}\sum_{j=0}^{N-1} (\bar{a}_j^E)^2} \; , \tag{5}$$

where:
L – number of samples of the total signal to be decomposed (it is justified that $L \geq N \cdot K$).

Bearing in mind the signal form described by formulas 1 or 2, the following relationship can be formulated in terms of signal power:

$$P^T = P^M + P^E + P^N, \tag{6}$$

where:
P^T – power of total signal a_i,
P^M, P^E, P^N – powers of signal components associated with mechanical (M), electromagnetic phenomena, respectively (E) and other components (N) - non-synchronous with f_s and f_r, and noise.

It can be assumed that relation 6 for $K \rightarrow \infty$ in terms of rms values will take form:

$$(a_{RMS}^T)^2 = (a_{RMS}^M)^2 + (a_{RMS}^E)^2 + (a_{RMS}^N)^2. \tag{7}$$

On this basis, for a finite number of averagings $k = K$, the rms value of non-synchronous signals and noise can be estimated according to the relation:

$$a_{RMS}^N \cong \sqrt{(a_{RMS}^T)^2 - (a_{RMS}^M)^2 - (a_{RMS}^E)^2}. \tag{8}$$

With the rms values and powers of the total and decomposed vibration acceleration signals, a multivariant analysis of the influence of asynchronous power supply method of an electric motor on the vibrations of its frame and end shield was performed.

4. Results

Based on the summary of the rms values of the total vibration acceleration signal (Tab. 2 and Fig. 6), recorded both on the front end shield of the motor and on its frame, it can be stated that:

- the typical star connection allows the smallest motor vibroactivity to be achieved; the vibration acceleration values in the 10-10000 Hz band for individual directions are close to 0.5 m/s^2; the dominant amplitude components of the signals are in the band up to approx. 1000 Hz (Fig. 5);
- the single-phase connection with a run capacitor results in approx. 2.5-fold increase in the rms values of the vibration accelerations (vector sum), both on the end shield and the motor frame, with the greatest changes in the axial direction;

- the use of an inverter has resulted in an approx. 7-fold increase in the rms values of vibration acceleration compared to the star connection; this is mainly due to the appearance of additional amplitude dominant components in the 4-6 kHz and 9-11 kHz bands (Fig. 7) related to the specific operation of the applied inverter, and more precisely to the frequency of the generated PWM signal [21, 22]; in the above-mentioned bands a 5 kHz pulse frequency and modulation side bands are included.

Table 2. Results summary of rms values of vibration signal after multi-synchronous decomposition measured on end shield and motor frame in different supply options

| STAR CONNECTION | vibration acceleration a_{RMS} [m/s^2] | | | | | | | |
| | end shield | | | | frame | | | |
	axial	tang.	radial	vect. sum	axial	tang.	radial	vect. sum
total	**0.53**	**0.58**	**0.56**	**0.97**	**0.59**	**0.59**	**0.36**	**0.91**
mechanical phenomena	0.23	0.26	0.26	0.44	0.25	0.28	0.17	0.41
electromagnetic phenomena	0.17	0.30	0.19	0.40	0.20	0.32	0.12	0.39
residual	0.44	0.42	0.47	0.77	0.49	0.41	0.30	0.71
SINGLE-PHASE CONNECTION	end shield				frame			
	axial	tang.	radial	vect. sum	axial	tang.	radial	vect. sum
total	**1.69**	**1.18**	**0.98**	**2.28**	**1.86**	**1.18**	**0.93**	**2.39**
mechanical phenomena	0.60	0.28	0.38	0.76	0.63	0.57	0.39	0.93
electromagnetic phenomena	1.30	0.92	0.54	1.69	1.45	0.67	0.59	1.70
residual	0.90	0.67	0.72	1.33	0.98	0.78	0.61	1.40
INVERTER	end shield				frame			
	axial	tang.	radial	vect. sum	axial	tang.	radial	vect. sum
total	**5.32**	**4.78**	**3.27**	**7.87**	**2.99**	**5.52**	**2.28**	**6.68**
mechanical phenomena	0.62	0.66	0.43	1.00	0.40	0.70	0.31	0.86
electromagnetic phenomena	0.89	1.10	0.63	1.55	0.57	1.01	0.44	1.24
residual	5.21	4.61	3.18	7.65	2.90	5.38	2.22	6.50
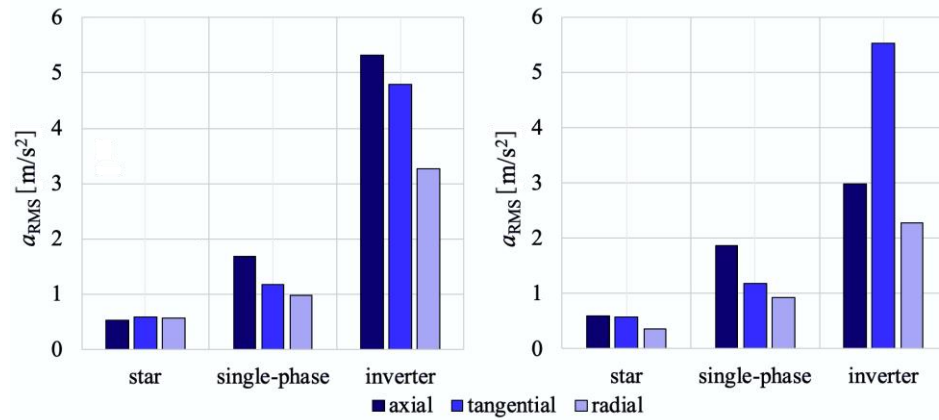
Figure 6. Vibration accelerations of the end shield and motor frame in three directions for different types of connection of motor to the power supply
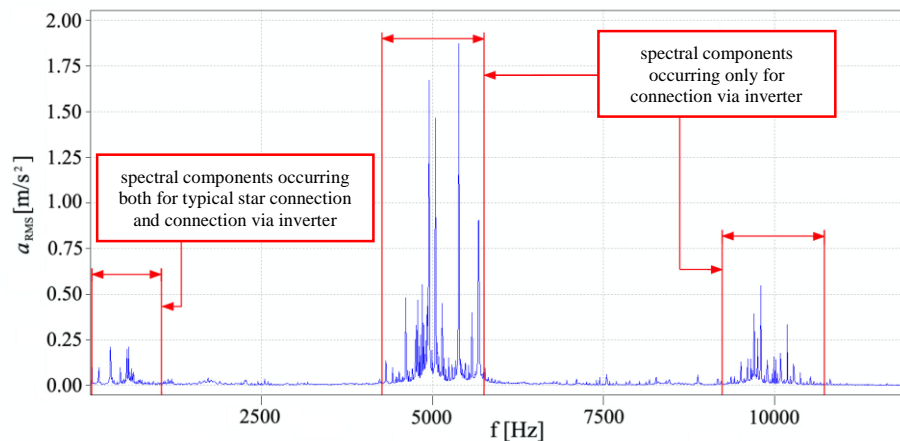
Figure 7. Example of a motor frame vibration acceleration spectrum illustrating the appearance of additional signal components resulting from the use of an inverter

Considering the use of vibrations as a carrier of information in diagnostics (e.g. post-production or operational), it would be justified to base diagnostic inference procedures on rms values obtained as a result of the MSA decomposition. The results of the decomposition are given in the Tab. 2. In addition to the rms values of vibration accelerations of mechanical and electromagnetic phenomena, rms values of components of signals non-synchronous with f_s and f_r and noise (residual components) determined in accordance with formula 8 are also provided.

Based on this data and Fig. 8-9 containing the power shares of individual signal components, the following conclusions can be drawn:

- the largest share of components synchronous with f_s and f_r at the star connection was recorded both on the motor body and on the bearing shield for measurements in the tangential direction (approx. 50%); this means that for this type of connection we obtain the best SNR ratio; also, for this direction the shares of components related to mechanical and electromagnetic phenomena are comparable (in the order of 20% - 30%),
- the single-phase connection causes a significant increase in the share of components associated with electromagnetic phenomena, depending on the direction, up to approx. 60%; this is due to an increase in the $2f_s$ component (100 Hz - magnetostriction),
- the use of the inverter in the motor power supply system results in the appearance of additional high-energy components non-synchronous with f_s and f_r, which is visible in a radical increase in their share in the signal (up to over 90%); this may cause masking of components related to mechanical and electromagnetic phenomena associated with f_s and f_r.

	axial direction	tangential direction	radial direction
typical star connection	18% 12% 70%	22% 29% 49%	21% 10% 68%
single-phase connection	11% 28% 61%	23% 32% 44%	18% 43% 40%
inverter	4% 2% 95%	3% 2% 95%	4% 2% 95%

■ mechanical phenomena ■ electromagnetic phenomena
□ signal not synchronous with f_s and f_r and noise
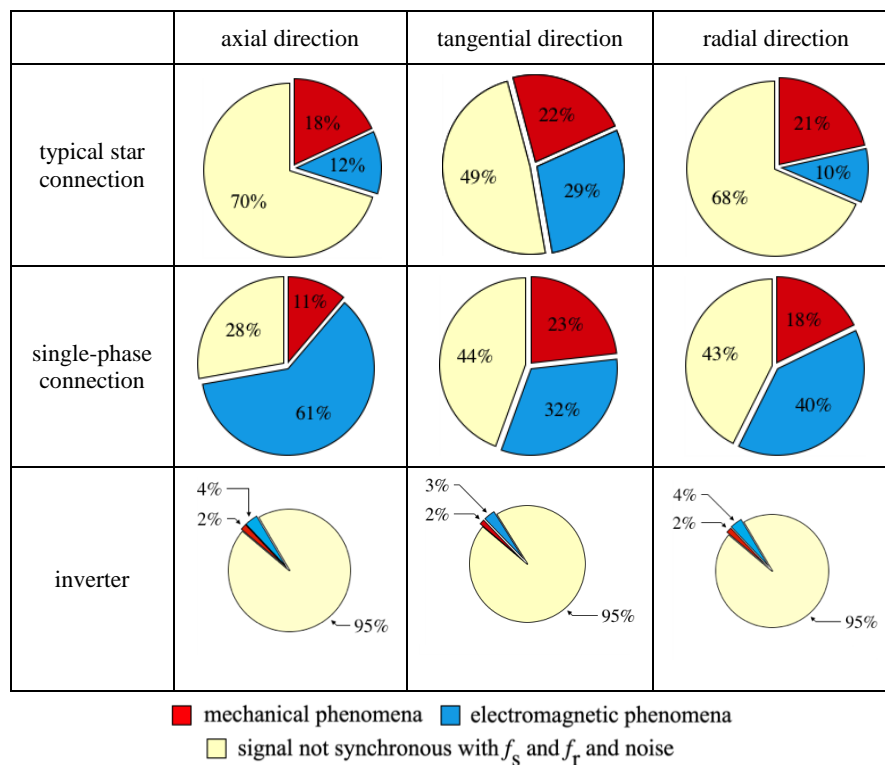
Figure 8. Summary of results of multi-synchronous decomposition of the vibration acceleration signal recorded on the motor frame
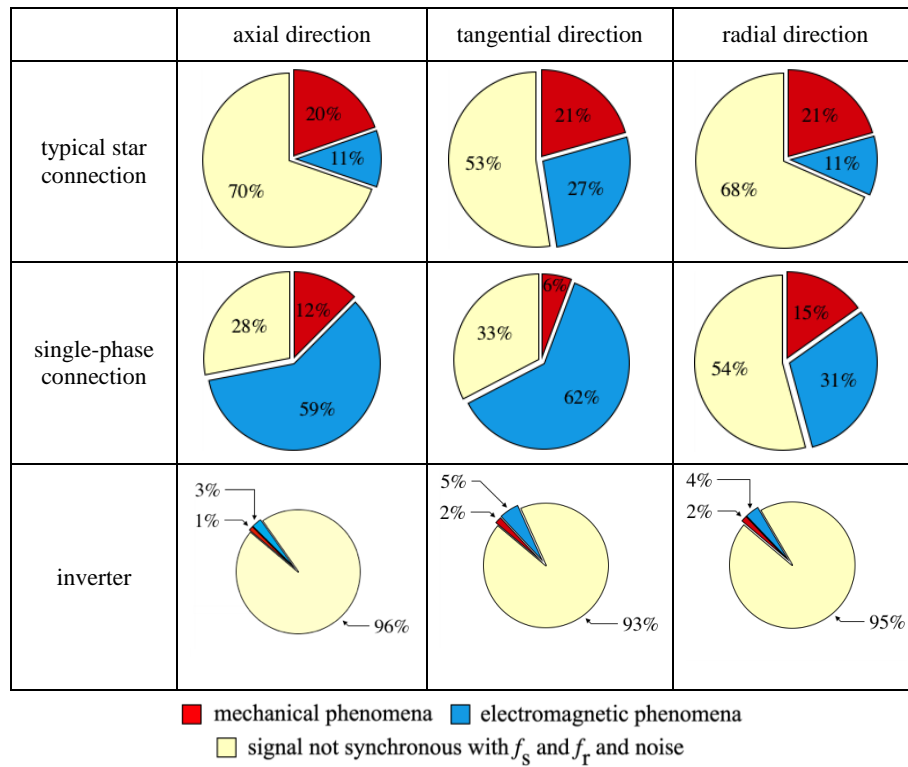
Figure 9. Summary of results of multi-synchronous decomposition of the vibration acceleration signal recorded on the front end shield of the motor

5. Conclusions

The conducted research allowed us to conclude that the application of the process of multi-synchronous decomposition in the diagnostics of asynchronous electric motors gives positive effects. It is possible to extract information on mechanical and electromagnetic phenomena from the vibration signal.

Considering the test results obtained, it is advisable to diagnose motors when they are connected in a star; this is supported by obtaining comparable rms values regardless of the location of the measuring transducer. Connection by an inverter potentially gives information about the motor's susceptibility to vibrations mainly in the band of approx. 5 kHz. This may be particularly important if the motor structure will have its own natural frequencies in this band. This may result in an increased noise level. The 5 kHz frequency band coincides with the most sensitive band of the human hearing organ [22].

Carrying out tests on a larger number of motors of the same type would make it possible to specify these regularities and, in terms of application, would provide the basis for determining the thresholds for classifying the motor quality in terms of electrical

and mechanical performance. In further tests of motors connected to the power supply via an inverter, it is justified to use a third signal synchronizing the multi-synchronous decomposition process related to the pulse frequency of the inverter obtained from the PWM signal. As a result, a three-stream MSA decomposition would be possible.

Acknowledgments

References

1. T. Glinka, *Diagnosing of electrical machinery* (in Polish), in: Inżynieria diagnostyki maszyn, Ed. B. Żółtowski, C. Cempel, PIB, Radom 2004, 633 – 654.

2. F. Ohnacker, *Maintenence of Electrical Equipment*, in: Maintenance Engineering Handbook, Ed. L.R. Higgins, Nowy Jork 1988, 7-1 – 7-28.

3. D. Miljković, *Brief Reviev of Motor Current Signature Analysis*, HDBKR Info Magazin, **5** (2015) 14 – 26.

4. K. Roczek, T. Rogala, *Induction Motor Diagnosis with use of electric parameters*, Diagnostyka, 20 (2019) 65 – 74.

5. S. A. Bednarz, M. Dybkowski, *Induction motor windong faults detection using flux-error based MRAS estimators*, Diagnostyka, **20** (2019) 87 – 96.

6. M. Boudiaf, L. Cherroun et al., *Real-time diangosisof three-phase induction motor machine using Arduino-UNO card based on Park's circle method*, Diagnostyka, **19** (2018) 63 – 71.

7. H. Çalis, *Vibration and motor current analysis of induction motors to diagnose mechanical faults*, Journal of Measurements in Engineering, **2** (2014) 190 – 198.

8. H. Bate, *Vibration Diagnostics for Industrial Electric Motor Drives*, Bruel & Kjaer Application Note, BO-0269-12, 1990.

9. P. A. Delgado-Arredondo, D. Morinigo-Sotelo et al., *Methodology for fault detection in induction motors via sound and vibration signals*, Mechanical Systems and Signal Processing, **83** (2017) 568 – 589.

10. M. Serrazin, S. Gillijns et al., *Vibro-acoustic measurements and techniques for electric automotive applications*, Proceedings of 43rd International Congress on Noise Control Engineering Internoise, 2014, 5128 – 5137.

11. J. Tulicki, J. Petryna et al., *Fault diagnosis of induction motors in selected working conditions based on axial flux signals*, Technical Transactions: Electrical Engineering, **3-E** (2016) 99 – 113.

12. J. Petryna, M. Sułowicz et al., *The use of axial flux in dynamic states testing of low and high power induction machines* (in Polish), Zeszyty Problemowe – Maszyny Elektryczne, **2** (2014) 165 – 171.

13. I. Gavranic, M. Vrazic et al., *Induction motor rotor cage faults as ignition sources of explosive atmosphere – research on heating*, Technicki Vjesnik, **24** (2017) 1025 – 1031.

14. D. Staton, L. Šušnjić, *Induction Motor Thermal Analysis*, Strojarstvo, **51** (2009) 623 – 631.

15. A. Regaz, B. Zegnini, et al., *Detection of faults in the asynchronous machine by the use of smart materials*, Diagnostyka, **19** (2018) 43 – 54.

16. K. K. Pandey, P. H. Zope et al., *Review on Fault Diagnosis in Three-Phase Induction Motor*, MEDHA, **1** (2012), 53 – 58.

17. M. R. Mehrjou, N. Mariun et al., *Rotor fault condition monitoring techniques for squirrel-cage induction machine — A review*, Mechanical Systems and Signal Processing, **25** (2011) 2828 – 2848.

18. M. Lebold, K., McClintic et al., *Review of vibration analysis methods for gearbox diagnostics and prognostics*, Proceedings of the 54th Meeting of the Society for Machinery Failure Prevention Technology, (2000) 623 – 634.

19. I. Bravo-Imaz, H. Ardakani et al., *Motor current signature analysis for gearbox condition monitoring under transient speeds using wavelet analysis and dual-level time synchronous averaging*, Mechanical Systems and Signal Processing, **94** (2017) 73 – 84.

20. S. Brown, *Discover Signal Processing – An Interactive Guide for Engineers*, John Wiley & Sons Ltd, Chichester 2008, 265 – 269.

21. Hitachi Industrial Equipment Systems Co., Ltd., *User manual: SJ200 inverter* (in Polish), **NB650XA** (2004).

22. J. Guziński, Z. Krzemiński, *Output filter of voltage inverter* (in Polish), Napędy i Sterowanie, **4** (2005) 43 – 44.

23. Z. Żyszkowski, *Basics of electroacoustics* (in Polish), Wydawnictwo Naukowo-Techniczne, Warszawa 1984, 228 – 261.

Urban Traffic Noise of Heavy Vehicles in Octave Bands

Andrzej BĄKOWSKI

Kielce University of Technology, Aleja Tysiąclecia Państwa Polskiego 7,
25314 Kielce, Poland, abakowski@tu.kielce.pl

Vladimir DEKÝŠ

University of Žilina, Univerzitná 8215/1, 010 26 Žilina, Slovakia,
vladimir.dekys@fstroj.uniza.sk

Leszek RADZISZEWSKI

Kielce University of Technology, Aleja Tysiąclecia Państwa Polskiego 7,
25314 Kielce, Poland, lradzisz@tu.kielce.pl

Paweł ŚWIETLIK

Kielce University of Technology, Aleja Tysiąclecia Państwa Polskiego 7,
25314 Kielce, Poland, pswietlik@tu.kielce.pl

Abstract

In this paper same results of heavy vehicles traffic measurements were used to simulate the noise measurands by the CNOSSOS-EU method for this purpose. The heavy vehicles traffic volume and velocity were recorded by permanent automatic monitoring station. The noise was calculated in octave bands according to the CNOSSOS-EU method. The positional and not positional measures of traffic noise were proposed for data scattering. The results was described using parameters such as the median, average peak noise, average maximum noise, average background level, first and third quartiles and relative measures of noise. Analyzes carried out for the tested section of the road showed that the traffic of heavy vehicles is not always the main source of road noise. It has been shown that maximum values of the acoustic pressure occur for the frequency of $f_0 = 500$ Hz. The dispersion of noise and type A uncertainty of the results were evaluated.

Keywords: urban noise, CNOSSOS-EU method, heavy vehicles

1. Introduction

A common noise prediction model was adopted by the member states of EU and is specified in Directive 2015/996/EC. The ultimate scope is to enhance the reliability and comparability of noise data in EU [1, 2]. Traffic noise and vehicle monitoring systems using permanent monitoring terminals were installed in some cities e.g. Lisbon to record the values of the measurands throughout the year. Such systems were constructed in Kielce - an example of a medium-size town (a population of approximately 200,000) located in the southern part of central Poland. Kielce has more than ten such stations, both in the centre and on the outskirts. The measurements results of heavy vehicle traffic flow from two vehicular lanes running towards the town and two lanes running towards Kraków were analysed. Computer simulation of the acoustic pressure in octave bands, in accordance with the CNOSSOS-EU model were carried out.

2. Traffic volume and noise measurements

Traffic noise and volumes analyzed in this study were measured by the permanent station recording traffic volume and sound pressure levels, located in Krakowska Street in Kielce. This street is the main part of the outward route from the center of Kielce towards Kraków, and carries both urban, suburban and transit traffic. The measurements from two vehicular lanes running towards the town (lane 1-2) and two lanes running towards Kraków (lane 3-4) were analysed. The station includes a road radar box, a sound level meter and a weather station. The traffic volume and speed were measured by WAVETRONIX digital radar with an operating frequency of 245 MHz. The acoustic microphone was positioned at a distance of 4 m from the edge of the lane 1-2 at a height of 4 m.

The measurements were documented at one hour intervals throughout the entire 24 hours of the day (1:00-24:00) throughout the year 2013. The traffic volume and speed data were recorded every 1 minute (buffer) and the averaged results were reported every 1 hour. The counts were used to calculate the traffic flow (understood as the sum of the number of vehicles recorded within a time interval) and speed, split into hours.

Detailed analyzes were carried out for the day sub-interval (date registered from 6.00 to 18.00) of a 24-hour period because it is the most burdensome time interval of the whole day. The results analyzed contained heavy vehicle traffic flow together with vehicle average speeds measurements. In this work analysis was based on the measurements in working days. The study showed that measurements carried out only on one working day (e.g. Wednesday), may not be representative.

3. Simulation of traffic noise measurands according with CNOSSOS-EU Method calculations

In many cities, traffic measurement systems only record traffic volume and speed. To make full use of the data obtained in this way to assess environmental pollution, a noise model is still needed. In the CNOSSOS-EU model the sound power level was divided on two parts – propulsion and rolling noise [3]. Propulsion sound power level is given by:

$$L_{WP,i,m}(v_m) = A_{P,i,m} + B_{P,i,m} \cdot \left(\frac{v_m - v_{ref}}{v_{ref}} \right) + \Delta L_{WP,i,m} \tag{1}$$

where:
- i – number of octave bands, from $i = 2$ for $f_0 = 125$ Hz up to $i = 7$ for $f_0 = 4000$ Hz,
- m – vehicle categories ($m = 1$-light motor vehicles, $m = 2$-medium heavy vehicles, $m = 3$-heavy vehicles, $m = 4$-powered two-wheelers),
- v_m – rolling speed of vehicle category m,
- v_{ref} – reference speed equal to 70 km/h,
- $A_{P,i,m}$, $B_{P,i,m}$ – coefficient for each octave band and for each vehicle category at the reference conditions,
- $\Delta L_{WP,i,m}$ – sum of correction coefficients for deviations from reference conditions.

Rolling sound power level:

$$L_{WR,i,m}(v_m) = A_{R,i,m} + B_{R,i,m}\log\left(\frac{v_m}{v_{ref}}\right) + \Delta L_{WR,i,m} \tag{2}$$

where:

$A_{R,i,m}$, $B_{R,i,m}$ − coefficient for each octave band and for each vehicle category at the reference conditions,

$\Delta L_{WR,i,m}$ − sum of correction coefficients for deviations from reference conditions.

Correction coefficients were not taken into account in the paper. The sound power level emitted by one of the vehicle category m and in octave band number i is:

$$L_{W,i,m}(v_m) = 10\cdot\log\left(10^{L_{WR,i,m}(v_m)/10} + 10^{L_{WP,i,m}(v_m)/10}\right) \tag{3}$$

If a steady traffic flow of vehicles of category m per hour is assumed with an average speed v_m the directional sound power level per 1 meter length per frequency band i of the source line determined by the vehicle flow is defined by:

$$L_{Weq,i,m} = L_{W,i,m}(v_m) + 10\cdot\log\left(\frac{Q_m}{1000 \cdot v_m}\right) \tag{4}$$

where:

Q_m − traffic flow of vehicles of category m per hour with an average speed v_m.

The acoustic pressure to the second power, measured by microphone, generated by vehicles category m in octave band i we can calculate according to formula:

$$p_{i,m}{}^2 = \sum_{j=1}^{Q_t} p_0^2 \cdot 10^{\left(L_{Weq,i,m} + 10\cdot\log\left(\frac{l_S}{Q_t}\right)-20\log(R_j)-8\right)\cdot 0.1} \tag{5}$$

where:

l_S − length of a source line with homogeneous traffic,

Q_t − amount of source line segments,

p_0 − reference sound pressure equal to $2\cdot 10^{-5}$ Pa,

j − index of source line segments,

R_j − distance of the center of the j source line segments from the measuring microphone.

In the paper, the tests for the variable components contained in the signals were based on measures [4]:

- median C_{50} − defined as the sound pressure value exceeded by the signal in 50% of the measurement period,
- the percentile C_{10} − defined as sound pressure value exceeded by the signal in 90% of the measurement period was used to assess average background noise level,
- the percentiles C_{25} and C_{75} are defined as the values of sound pressure value exceeded by the signal respectively in 75% or 25 % of the measurement period,

- to assess the average peak level the percentile C_{90}, defined as sound pressure value exceeded by the signal in 10% of the measurement period was used,
- to assess the average maximum noise the percentile C_{99}, defined as sound pressure value exceeded by the signal in 1% of the measurement period was used,
- range between 10 and 90 percentile, in which 80% of all data is included

$$C_{[10,90]} = [C_{10}(p_i), C_{90}(p_i)] \tag{6}$$

Standard uncertainty of the acoustic pressure, determined in the Type A evaluation, can be calculated from the following relationship:

$$u_A = \sqrt{\frac{1}{n(n-1)} \sum_1^n (p_i - \bar{p_i})^2} \tag{7}$$

where *n* is the amount of data.

In this study, the authors analysed acoustic pressure values p_i expressed in terms of pascals to be able to easily compare the fixed components (median) and variable components of the acoustic pressure signals. The tests for the variable components contained in the signals were based on the measures: coefficient of variation [5], quartile deviation (Q_{31}), quartile variation coefficient ($V_{Q_{31}}$), and quartile coefficient of dispersion (V_{Q1Q3}). The influence by atypical data, taken into account in the analyses is less significant when positional measures are used. The measure of dispersion of the variable is the average quartile deviation:

$$Q_{31} = 0.5 \cdot [C_{75}(p_i) - C_{25}(p_i)] \tag{8}$$

Quartile deviation is an absolute measure that defines the average variance of half of the measurement data around the median (after rejecting 25% data with the lowest values and 25% data of the highest values of sound pressure). By relating it to the median, the positional coefficient of variation is calculated from (9):

$$V_{Q_{31}} = \frac{Q_{31}}{Med} \cdot 100\% \tag{9}$$

It is a dimensionless relative measure that can be used to directly compare the variable components in its several realisations.

The quartile coefficient of dispersion is a relative measure of variance, that can be calculated from (10):

$$V_{Q1Q3} = \frac{Q_3 - Q_1}{Q_1 + Q_3} \cdot 100\% \tag{10}$$

The positional coefficient of variation and the quartile coefficient of dispersion are positional measures of the data between the first and third quartiles. Thus, atypical data exert less influence on these coefficients. It has to be noted, however, that the data under

analysis represent the measurements collected within 24-hour periods, thereby atypical data cannot be regarded as erroneous measurements. Those measures determine the variability of acoustic pressure. It was assumed in this paper that the acoustic source are:

- entry traffic on two lanes, that leads from Kraków towards Kielce– denoted as lanes 1-2,
- exit traffic on two lanes, that leads from Kielce towards Kraków – denoted as lanes 3-4.

It has been assumed in accordance with the CNOSSOS-EU noise model that the linear acoustic source is located along the symmetry axis of the respective lanes. Thus, the work analyzed the results of computer simulations of acoustic pressure in the place where the measuring microphone is located, i.e. at a distance of 4 m from lanes 1-2 and at a height of 4 m for two incoherent acoustic sources using measurements of relevant parameters of road vehicles. The acoustic pressures generated by these sources were also added up, which allows to assess the total noise generated by the examined road section. In [6], the values of the equivalent sound level (for all vehicles) experimentally measured and calculated according to the CNOSSOS-EU method were compared by calculating the root mean square error (RMSE) parameter. The calculated value of this parameter is about 1 dB.

4. Results

Figure 1 presents the averaged results of traffic volume measurements for heavy vehicles in subsequent hours of working days. Comparing figure 1a with 1b, there are some significant differences. In both drawings there is a local maximum of traffic volume at 9.00 (the so-called morning peak). In contrast, the afternoon peak occurs only in figure 1b (at 17.00).
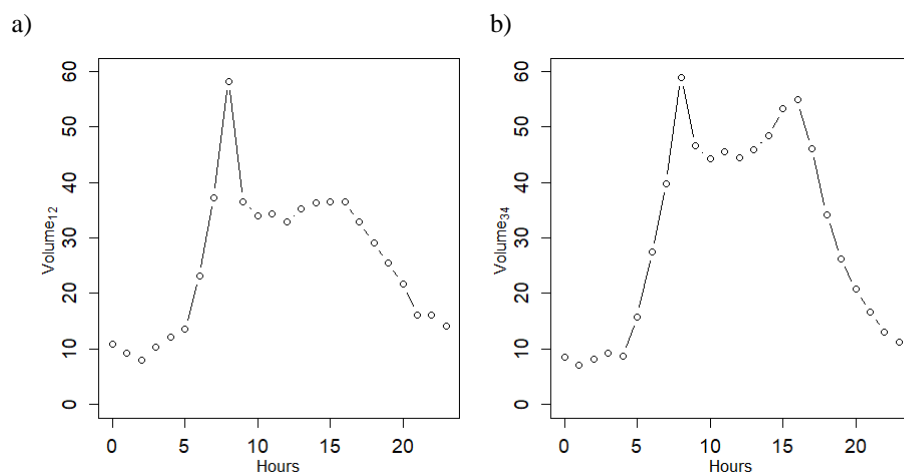
a) b)

Figure 1. Average values of traffic flow (on working days in 2013) for heavy vehicles: a) on lanes 1-2, b) on lanes 3-4

Heavy vehicles traffic flow graphs on arbitrarily selected two Wednesdays in 2013 are shown in Figure 2. The graphs show that the measured traffic flow over the 24 hours may not be representative of the entire year. This conclusion justifies the need for long-term monitoring of heavy vehicles traffic.
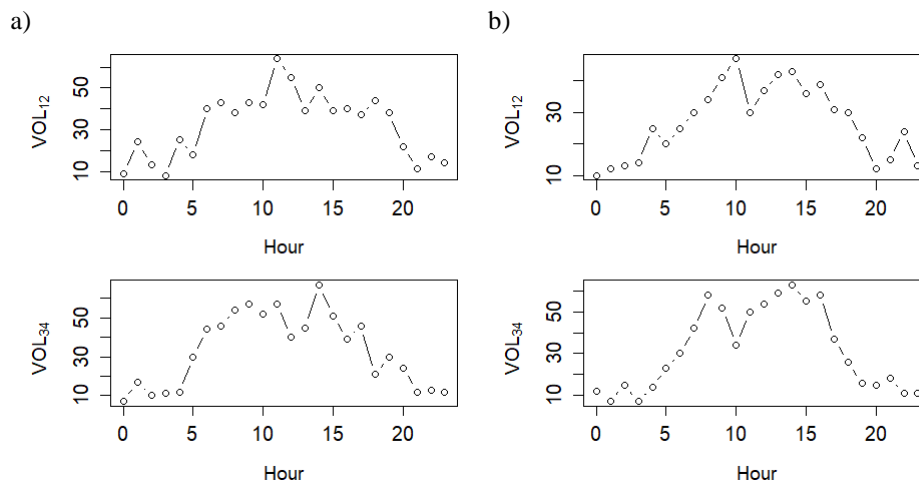
Figure 2. Traffic flow for heavy vehicles on lanes 1-2 or 3-4:
a) on Wednesday - 26 06.13, b) on Wednesday - 03.07.13

Shapiro-Wilk and Jarque-Bera tests showed that the acoustic pressure distributions generated by heavy vehicles are not compatible with the normal distribution. Histograms of acoustic pressure distributions on working days of 2013 for heavy vehicles including a 1-2 or 3-4 lane confirmed deviations from the normal distribution. Examples of histograms in the octave band $f_0 = 500$ Hz are shown in figure 3. Values of selected data distribution parameters are: for figure 3a: skewness is 2.6 and kurtosis is 15.7, for figure 3b: skewness is 0.03 and kurtosis is 6.5. Note the diverse forms of these distributions on each lane.

Table 1 summarizes the results of the data analysis for values of acoustic pressure parameters in selected octave bands, on working days for the day sub-interval , generated by vehicles of all categories calculated by the CNOSSOS-EU method. Maximum values of median as well as percentiles C_{10} and C_{90} were obtained in an octave with a central frequency of $f_0 = 1000$ Hz. The minimum values of these parameters were obtained in an octave with frequency $f_0 = 4000$ Hz. The values of the parameter C_{99} in relation to the value of C_{90}, for lanes 1-2: in an octave with frequency $f_0 = 125$ Hz are 80% higher. In other octave bands these differences are not so significant. For the frequency $f_0 = 1000$ Hz they are about 5%. Values of coefficients of variation are in the range from 3% to 5% and uncertainty u_A is less than 0.10 mPa. Differences in the values of the same parameters (C_{90} and C_{99}) but for lanes 3-4 are smaller and for the octave band $f_0 = 1000$ Hz they are about 6 %. Values of coefficients of variation for lanes 3-4 are from 4.5% to 6%. The value of the C_{99} parameter is greater than C_{90} by about 6% to 8%. The maximum values of the parameters of the sum of the acoustic pressure generated by lanes 1-2 and 3-4 occur in the

octave band $f_0 = 1000$ Hz. Only the maximum value of the C_{99} parameter in the $f_0 = 125$ Hz band is higher than C_{90} by about 50 %.

a) b)
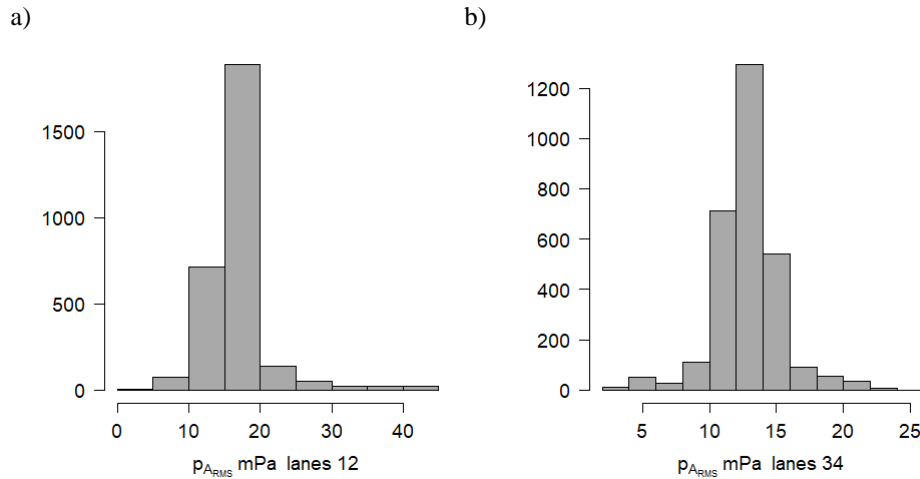
Figure 3. Acoustic pressure distribution in octave band $f_0 = 500$ Hz in working days 2013: a) on lanes 1-2, b) on lanes 3-4

Table 1. The values of sound pressure parameters on working days for the day sub-interval, generated by vehicles of all categories calculated by the CNOSSOS-EU method, in selected octave bands

Central frequency band f_0 [Hz]	Med. [mPa]	Q_{31} [mPa]	Vq [%]	V_{Q1Q3} [%]	u_A [mPa]	C_{10} [mPa]	C_{90} [mPa]	C_{99} [mPa]
values of sound pressure parameters generated by all vehicles on lanes 1-2								
125	27.98	1.26	4.50	4.49	0.10	25.36	31.19	55.76
500	31.69	1.38	4.36	4.36	0.07	28.67	34.66	47.23
1000	42.85	1.23	2.88	2.88	0.06	39.49	45.14	47.47
values of sound pressure parameters generated by all vehicles on lanes 3-4								
125	21.63	1.30	6.01	5.96	0.05	18.82	24.66	26.97
500	25.78	1.41	5.46	5.43	0.06	22.34	28.90	31.16
1000	32.43	1.49	4.58	4.57	0.06	28.58	35.61	37.45
values of sound pressure parameters generated by all vehicles on lanes 1-2 and 3-4								
125	35.48	1.59	4.48	4.47	0.10	32.23	39.45	60.81
500	40.99	1.76	4.30	4.31	0.09	37.14	44.74	55.23
1000	53.88	1.72	3.19	3.20	0.08	49.62	56.94	59.25

Table 2 compiles the analysis results for acoustic pressure parameters in selected octave bands, on working days for the day sub-interval, generated by heavy vehicles calculated by the CNOSSOS-EU method. The calculations show that maximum values of median as well as percentiles C_{10} and C_{90} were obtained in an octave with a central frequency of

$f_0 = 500$ Hz. The minimum values of these parameters were obtained in an octave with frequency $f_0 = 4000$ Hz. The values of the parameter C_{99} in relation to the value of C_{90}, for lanes 1-2: in an octave with frequency $f_0 = 125$ Hz are 172 % higher and for frequency $f_0 = 500$ Hz or $f_0 = 1000$ Hz about 100 %. For the frequency $f_0 = 2000$ Hz they are about 110 %. Values of coefficients of variation are about 9 % and uncertainty u_A is less than 0.10 mPa. Differences in the values of the same parameters (C_{90} and C_{99}) but for lanes 3-4 are smaller and for the octave band $f_0 = 1000$ Hz they are about 4 mPa. Values of coefficients of variation for lanes 3-4 are about 9 %. The value of the C_{99} parameter is greater than C_{90} by about 30%. The maximum values of the parameters of the sum of the acoustic pressure generated by lanes 1-2 and 3-4 occur in the octave band $f_0 = 500$ Hz. Only the maximum value of the C_{99} parameter in the $f_0 = 125$ Hz band is higher than C_{90} by about 135%. Statistical analysis of the acoustic pressure values shows that the values of Q_{31} for heavy vehicles fall within the range 1.0 mPa to 1.6 mPa.

Table 2. The values of sound pressure parameters on working days for the day sub-interval, generated by heavy vehicles calculated by the CNOSSOS-EU method, in selected octave bands

Central frequency band f_0 [Hz]	Med. [mPa]	Q_{31} [mPa]	Vq [%]	V_{Q1Q3} [%]	u_A [mPa]	C_{10} [mPa]	C_{90} [mPa]	C_{99} [mPa]
values of sound pressure parameters generated by heavy vehicles on lanes 1-2								
125	13.21	1.21	9.16	9.11	0.10	10.96	16.35	44.58
500	16.28	1.44	8.87	8.86	0.08	13.51	19.63	38.90
1000	14.88	1.30	8.76	8.74	0.07	12.34	17.82	34.80
values of sound pressure parameters generated by heavy vehicles on lanes 3-4								
125	10.24	0.97	9.45	9.46	0.04	8.29	12.43	16.81
500	12.88	1.15	8.96	8.99	0.05	10.40	15.30	20.60
1000	11.85	1.06	8.90	8.93	0.04	9.57	14.01	18.76
values of sound pressure parameters generated by heavy vehicles on lanes 1-2 and 3-4								
125	16.73	1.33	7.97	7.94	0.10	14.24	20.04	47.67
500	20.75	1.58	7.62	7.61	0.09	17.71	24.36	43.52
1000	19.04	1.44	7.54	7.54	0.08	16.23	22.16	39.09

The share of acoustic pressure generated by heavy vehicles in the total acoustic pressure generated by road vehicles of all categories can be calculated according to

$$\frac{p_{hv}(f_0, C_X)}{p_{av}(f_0, C_X)} \cdot 100 \% = R(f_0, C_X) \tag{11}$$

where

p_{hv} – acoustic pressure of heavy vehicles,
p_{av} – acoustic pressure of all vehicles.

It depends on the center frequency of the octave band ($f_0 = 125, 250, ... 4000$ Hz) and the percentile number ($X = 10, 50, 90, 99$). The calculations show that this value varies from 28 % to 80 %, as shown in the table 3.

Table 3. The share of acoustic pressure generated by heavy vehicles in the total acoustic pressure generated by road vehicles of all categories

f_0	$R(f_0, C_{10})$ [%]	$R(f_0, C_{50})$ [%]	$R(f_0, C_{90})$ [%]	$R(f_0, C_{99})$ [%]
125 Hz	43	49	50	79
250 Hz	47	50	52	77
500 Hz	49	51	53	80
1000 Hz	32	35	39	66
2000 Hz	28	30	31	61
4000 Hz	33	38	39	70

The highest values of the $R(f_0, C_X)$ parameter occur in the octave band $f_0 = 500$ Hz and for the C_{99} percentile, i.e. the average maximum acoustic pressure.

5. Conclusions

The traffic volume analysis carried out on lanes 1-2 and 3-4 shows that for all vehicles and heavy vehicles there are differences in the flow of cars entering and leaving the city. These differences indicate that some drivers treat Krakowska Street as a transit road despite the existing Kielce bypasses.

The study showed that measurements carried out only on one working day (e.g. Wednesday), may not be representative.

Despite differences in the value of vehicle traffic intensity on lanes 1-2 and 3-4, there is a similarity in noise changes (calculated according to the CNOSSOS-EU model) as a function of time. The octave bands in which the greatest acoustic pressure is generated are the $f_0 = 500$ Hz and $f_0 = 1000$ Hz band. The values of acoustic pressure parameters in this bands dominate both for heavy and all vehicles.

It has been shown that for working days and in octave band $f_0 = 1000$ Hz 80% of the data are in the range of limit values: for all vehicles (50 mPa, 57 mPa) while for heavy vehicles in the range of limit values (16 mPa, 22 mPa). But in octave band $f_0 = 500$ Hz 80% of the data are in the range of limit values: for all vehicles (37 mPa, 45 mPa) while for heavy vehicles in the range of limit values (18 mPa, 24 mPa).

For heavy vehicles, the maximum values for median and percentiles C_{10} and C_{90} were obtained in octave band with a center frequency of $f_0 = 500$ Hz. The minimum values of these parameters were obtained in the octave band with center frequency $f_0 = 4000$ Hz. The values of the parameter C_{99} in relation to the value of C_{90} (for lanes 1-2): in the octave band with frequency $f_0 = 125$ Hz are higher by about 170% and for the frequency $f_0 = 500$ Hz or $f_0 = 1000$ Hz by about 100%.

The values of the coefficients of variation V_q and V_{Q1Q3} are similar in all octave bands but depend on the vehicle category and the central frequency f_0.

The share of acoustic pressure generated by heavy vehicles in the total acoustic pressure generated by road vehicles of all categories depends on the center frequency of the octave band and the percentile number and ranges from 28% to 80%. The highest values occur in the band $f_0 = 500$ Hz and for the C_{99} percentile of acoustic pressure.

References

1. G. Dutilleuks, B. Soldano, *Matching directive 2015/996/EC (Cnossos-EU) and the French emission model for road pavements,* Euronoise 2018 Conferece Proceedings, (2018) 1213 – 1218.

2. K. J. Waluś, Ł. Warguła, P. Krawiec, J. M. Adamiec, *Legal regulations of restrictions of air pollution made by non-road mobile machinery – the case study for Europe,* A review. Environmental Science and Pollution Research, **25** (2018) 3243 – 3259.

3. S. Kephalopoulos, M. Paviotti, F. Anfosso-Lédée, D. Van Maercke, S. Shilton, N. Jones, *Advances in the development of common noise assessment methods in Europe: The CNOSSOS-EU framework for strategic environmental noise mapping*, Science of The Total Environment, 482–483 (2014) 400-410.

4. B. Przysucha, W. Batko, A. Szeląg, *Analysis of the accuracy of uncertainty noise measurement,* Archives of Acoustics, **40**(2) (2014) 183 – 189.

5. A. Bąkowski, L. Radziszewski, M. Žmindak, *Analysis of the coefficient of variation for injection pressure in a compression ignition engine*, Procedia Engineering, **177** (2017) 297 – 302.

6. A. Bąkowski, V. Dekýš, L. Radziszewski, Z. Skrobacki, *Validation Of Traffic Noise Models*, AIP Conference Proceedings, 2077, 020005, 2019.

Energy Harvesting Shock Absorber with Linear Generator and Mechanical Motion Amplification

Nitin SATPUTE

Faculty of Mechanical Engineering, Vishwakarma University, Pune,
nitin.satpute@vupune.ac.in

Marek IWANIEC

Faculty of Mechanical Engineering and Robotic, AGH University of Science and
Technology, Al. Adama Mickiewicza 30, 30-059 Kraków, Poland, iwaniec@agh.edu.pl

Ramesh NARINA

AGH University of Science and Technology, Faculty of Mechanical Engineering and
Robotics, Department of Process Automation,
Al. Adama Mickiewicza 30,30-059 Kraków, Poland, narina@agh.edu.pl

Sarika SATPUTE

MSEDCL, Office of Regional Director, Pune, India, sarikasatpute16@gmail.com

Abstract

Energy harvesting shock absorbers can generate about 15-20 W of electric power for normal suspension velocities. However, higher weight, fail safe characteristics and space limitations have restricted development of regenerative shock absorbers to research prototypes. Power to weight ratio of regenerative shock absorbers can be improved by incorporating motion amplification. In the presented work, an innovative design of energy harvesting shock absorber has been presented that uses motion amplification for improving harvesting efficiency. Apart from improving electric power, the proposed solution is fail safe and can be easily incorporated in existing vehicles with only marginal change in suspension layout. Study includes detailed numerical analysis for vibration transmissibility to investigate comfort and safety. Further, a prototype has been fabricated and experimentation has been performed to compute electric power generated and comfort. Simulations have been performed on real size model with utilization of harvested electric power which indicates about 19% of overall harvesting efficiency.

Keywords: motion amplification, electric power, energy harvesting, efficiency, numerical simulation

1. Introduction

Energy harvesting shock absorbers constitutes an electric generator, which is used as the dissipative element instead of conventional fluid damper and can harvest up to 15-20 W of electric power [1, 2]. However, lower power to weight ratio, bulky design, non-linear damping force and inferior fail safe characteristics have limited the scope of regenerative shock absorbers to research prototypes. Recently, hybrid version of regenerative shock absorbers use the electric generator as the power harvesting element, that supplements vibration energy dissipation, in addition to that of the fluid damper. Hybrid electromagnetic shock absorbers have better fail safe characteristics and can provide the necessary damping coefficient for a real size application with compact size [3].

Furthermore, velocity amplification is being preferred to ensure better power to weight ratio [4, 5].

Numerical simulation has been used to derive the optimum configuration of electric generators used in energy harvesting shock absorbers [6, 7]. The energy harvested by the shock absorber can be used for charging electric battery in the vehicle [8]. Indirect drive type of regenerative electric shock absorbers are preferred over that of the direct drive version due to compact design and efficient operation [9, 10]. Theoretical simulations on hydraulic electromagnetic shock absorber, implemented in a railway suspension, estimated that 300-500 W of peak power can be harvested [11, 12]. A hybrid regenerative shock absorber harvested 0.25 W of power for 0.004 m/s of suspension velocity [13]. Energy harvesting shock absorber with additional energy storage device can increase range of electric vehicles [14]. Electromagnetic regenerative shock absorber with rack-pinion mechanism and fluid elements can be used for amplification of the coil relative velocity [15]. Quarter car simulations and finite element analysis have been used to evaluate regenerative shock absorbers for power harvested and vibration isolation performance [16, 17].

Vibration energy dissipation by the electric generator used in real size shock absorber applications, is limited due to practical constraints on size and weight. Therefore, to make up the additional requirement of energy dissipation, a fluid damper is added to the system. Although number of hybrid shock absorbers has been reported in the literature, their practical implementation is limited due to the following reasons.

- Electromechanical damping force is non-linear in nature, accordingly comfort and safety is compromised with higher electromechanical damping force. However, reducing the damping also reduces power harvested. Therefore there is a need to increase the electrical power and at the same time keep the resultant vertical component of the damping force to minimum.
- Most of the indirectly driven electrical generators utilize mechanical gears which are prone to be damaged under parasitic loading conditions encountered in case of suspensions.
- Real case incorporation of the hybrid shock absorber needs to be demonstrated particularly in case of smaller C-segment car, to study the practical effect on comfort of the vehicle and fail safe characteristics.

An attempt has been made in the presented paper to overcome the above limitations of existing indirectly driven hybrid regenerative shock absorbers, with an innovative design, hereafter referred as Hydraulic ElectroMagnetic Shock Absorber (HEMSA). A link based mechanism has been used to drive a linear generator with amplified coil relative velocity. Numerical model of the shock absorber has been presented that estimates power harvested, comfort and safety of the vehicle. Further, a prototype has been fabricated and incorporated in a C-segment car suspension to experimentally evaluate electrical energy harvested and effect of the regenerative suspension on comfort of the vehicle.

2. Mathematical modelling

A quarter car model shown in Figure 1 has been used for numerical simulation of HEMSA,. It comprises of sprung mass (m_1), unsprung mass (m_2), suspension spring (stiffness: K_s), fluid damper (damping coefficient: C_s) and the tyre (with vertical stiffness: K_t). Further the link based amplification mechanism has been fitted between the sprung and unsprung masses. The amplification mechanism has links as illustrated in Figure 1 and it operates with vertical relative velocity between the sprung and un sprung masses to drive the linear generator assembly in horizontal direction. The linear generator assembly as illustrated in Figure 1 has the armature coils carried by one side of the amplification mechanism whereas the other side is connected to the magnet and spacer assembly. The presented arrangement ensures 320% amplification in the generator coil relative velocity. Governing differential equations for the system are given as:

$$m_1\ddot{z} = -K_s(z - y) - C_s(\dot{z} - \dot{y}) - F_{\text{lg}} \sin\left[2\sin^{-1}\frac{h - |y - z|}{2l}\right] \tag{1}$$

$$m_1\ddot{y} = -K_t(y - x) + K_s(z - y) + C_s(\dot{z} - \dot{y}) + F_{\text{lg}} \sin\left[2\sin^{-1}\frac{h - |y - z|}{2l}\right] \tag{2}$$

where:
F_{lg} – electromagnetic braking force on the linear generator coils,
l – amplification mechanism link length.

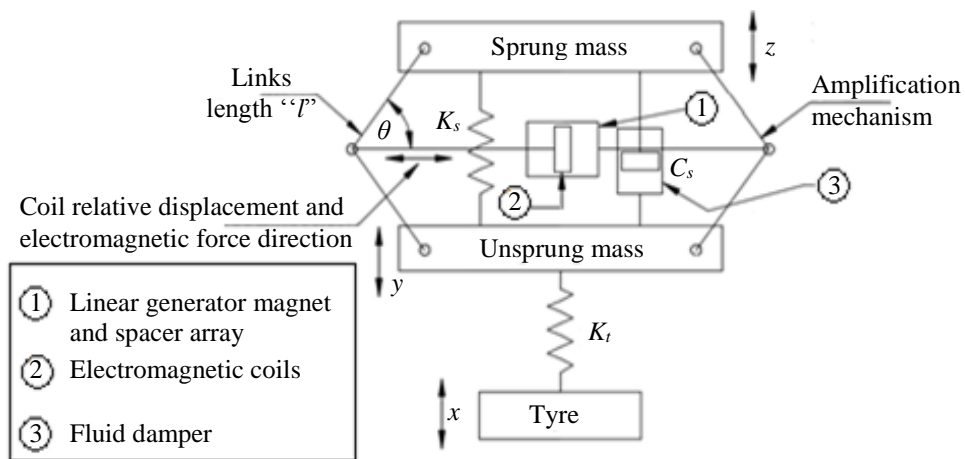
Figure 1. Modified quarter car model

Voltage across the load resistance is given as:

$$U_{tot} = IR_{total} = \left(\pi D_{avg}\, N_c B \dot{u}\right) - L_{coil}\frac{dI}{dt} \tag{3}$$

Voltage across the coils depends on average armature coil diameter in the linear generator (D_{avg}), number of copper wire turns in the armature (N_c), air gap magnetic flux density (B), coil relative velocity in horizontal direction $\left(\dot{u}\right)$ and the coil inductance (L_{coil}).

The coil relative displacement in horizontal direction is given as,

$$u = \frac{h-(z-y)}{2\tan\left[\sin^{-1}\dfrac{h-(z-y)}{2l}\right]} - \frac{1}{2}\sqrt{4l^2 - h^2} \tag{4}$$

where:
 h – distance between the sprung and unsprung masses at equilibrium.

Simulations have been performed in MATLAB based on Equations (1)-(4). Vertical displacement of the tyre (x) have been experimentally measured for two types of road profiles and used in the theoretical model during the simulations.

3. Experimental and simulation results

Prototype HEMSA has been designed to suit rear suspension of C-size passenger car (Maruti Suzuki Zen Lxi), which has been used along with the existing helical spring (stiffness: 10.5KN/m) and fluid damper (mean damping coefficient: 880 Ns/m with damper asymmetry of 70/30). Available layout in the suspension allows 220 mm of vertical and 210 mm of horizontal space. The CAD model is illustrated in Figure 2, which includes amplification links, linear generator, engagement mechanism, lower support and upper support. For more elaborate details on design and fabrication of the linear generator used in electromagnetic shock absorbers, the interested readers should refer to our earlier publication [18]. Photograph of the prototype fitted in the vehicle is shown in Figure 3.

It is necessary to ensure effective rattle space of the fluid damper, irrespective of limitations of the linkage mechanism vertical stroke. This is ensured by spring loaded ball and pin in the engagement mechanism, as illustrated in Figure 2. In case the suspension stroke exceeds working limit of the amplification mechanism, the spring loaded ball disengages the mechanism from suspension movement. The linear generator assembly comprises of magnets, inner spacers and outer spacer with constructional details given in Table 1. The links with length of 95 mm ensure effective velocity amplification within the available space. Upper and lower supports ensure rigid fastening of the prototype assembly to the sprung and unsprung masses respectively.

Experimentation has been performed to evaluate electrical power harvested and comfort in the vehicle. The test vehicle was driven along two types of roads (referred as Type-1 and Type-2) and acceleration (at the tyre and sprung mass) have been measured with a vibration meter (Instrument: Svantek SVAN958 - four channel sound and vibration analyser) and two uniaxial accelerometers (SV 3185 D). Electrical power harvested by the

linear generator has been evaluated by measuring voltage across electrical resistance (5 Ω) with an oscilloscope (Tektronix TDS 1001B).

Table 1. Details of the linear generator

Magnet and inner spacer outer diameter (inner diameter x outer diameter x thickness):	9mm x 12mm x 5mm (10 numbers)
Magnet material and coercive force	Ferrite, 254 kA/m
Outer spacer (inner diameter x outer diameter x thickness)	19mm x 22mm x 104mm
Material for inner and outer spacers	Mild steel
Armature copper wire diameter and number of turns	0.2 mm with 85 turns

Test vehicle set up with all the equipment is shown in Figure 4. Further, vertical acceleration measured at the tyre has been used in theoretical simulation to determine the sprung mass acceleration, electric power and tyre deflection from the numerical model. Experimental and simulation results for the sprung mass acceleration are shown in Table 2, which shows close agreement. Experiment was conducted to determine sprung mass acceleration without the prototype HEMSA fitted in the rear suspension and maximum acceleration was recorded to be 1.524 m/s^2. Safety criteria of the shock absorber has been evaluated by calculating the root mean square (rms) tyre deflection. Lower tyre deflection gives lesser variation in forces transmitted from tyre to the road and vice versa. Values of rms tyre vertical deflection for the prototype HEMSA have been calculated from numerical simulation and reported in Table 2. Further simulations performed with the theoretical model indicate that maximum rms tyre deflection for conventional fluid shock absorber (without prototype HEMSA) will be 3.51 mm.

Marginal increment in the acceleration (8%) and tyre deflection (7%) is attributed to the fact that presently the linear generator has been incorporated along with the existing fluid damper, which increases overall damping coefficient for HEMSA than that of the conventional fluid shock absorber. However, there is a need to redesign the fluid damper since electromagnetic damping is being assisting in energy dissipation. Simulation study indicates that the vertical component of electromagnetic force is about 20-25% than that of the braking force on the generator coils (i.e. F_{lg}). Linear generator coils are operated with amplified relative velocity (than that of the relative velocity between sprung and unsprung masses) to derive better power output and simultaneously only fraction of the electromagnetic force is transmitted as the vertical component, that influences comfort and safety. Thus HEMSA ensures more power output and effect of electromagnetic force on the vibration isolation is kept at minimum.

The peak power of the real size HEMSA can be significantly improved by replacing the ferrite magnets with high energy density rare earth magnets and improving number of copper wire turns. Literature indicates that maximum flux density in the linear generator air gap can be increased up to 0.7 T. Minor changes in the existing vehicle layout can facilitate redesign of amplification mechanism to ensure velocity increase up to 800% that of the suspension vertical velocity. These modifications will ensure that the real size HEMSA will ensure peak power of about 18-25 W for each of the shock absorber with an efficiency of 19.28%.
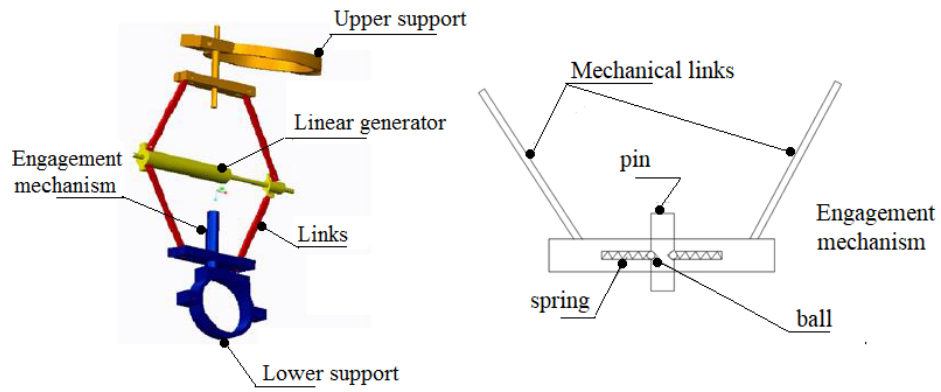
Figure 2. CAD model of the prototype with engagement mechanism
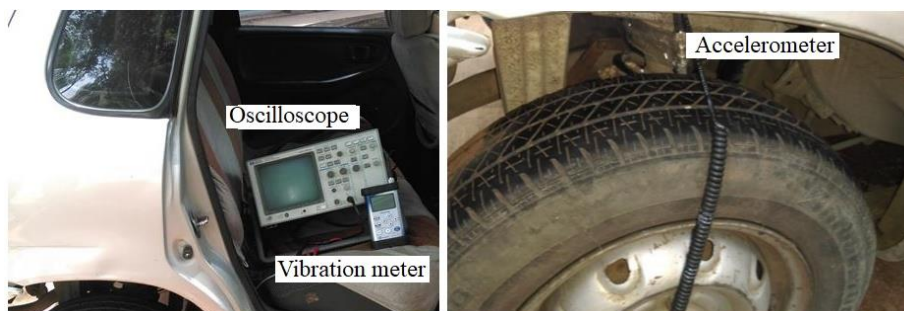

Figure 3. The view of EMSA prototype

Figure 4. Test set up

Table 2. Experimental and simulation results for comfort,
handling and electric power

Type of road	Vehicle speed [km/h]	Sprung mass peak vertical acceleration [m/s^2]		Peak electric power [mW]		Peak tyre displacement [mm]
		Therotical	Experimental	Therotical	Experimental	
Smooth Type 1	10	0.127	0.132	3.1	2.0	1.25
Smooth Type 1	20	1.218	1.356	8.2	6.5	2.84
Rough Type 2	10	0.282	0.355	6.2	5.1	2.38
Rough Type 2	20	1.580	1.673	28.0	20.0	3.81

4. Conclusion

The study presents design of an energy harvesting shock absorber (HEMSA) that uses amplification links to increase electrical power output. Results of numerical modelling has been presented to evaluate comfort, safety and electric power. Novel feature of the presented work includes design, fabrication, fitment and experimentation of the prototype HEMSA in a C-size passenger car rear suspension. The experimentation has been performed to determine acceleration transmitted and electrical power harvested by the energy harvesting shock absorber, when the vehicle travelled along two types of roads with different velocities. Vertical acceleration at the tyre has been measured with an accelerometer and used to evaluate the numerical model for validating the experimental data. Simulation and experimental results indicate that electrical power up to 21 mW can be harvested with only marginal increment in the sprung mass acceleration. In the event of the electric generator failure, fluid damper will provide minimum force ensuring better failsafe characteristics. The prototype has used ferrite magnets and existing rear suspension layout. However significant power of up to 18-25 W can be harvested from each of the shock absorber, with redesign of existing suspension layout for more vertical space for HEMSA and use of high energy rare earth magnets.

References

1. A. I. Sultoni, I. N. Sutantra, A. S. Pramono, *Modeling, prototyping and testing of regenerative electromagnetic shock absorber*, Appl. Mechanics and Materials, Trans Tech Publications, **493** (2018) 395 – 400.
2. N. V. Satpute, S. Singh, S. M. Sawant, *Energy Harvesting Shock Absorber with Electromagnetic and Fluid Damping*, Adv. Mech. Eng., **2014** (2014) 1 – 14.
3. W. Salman, L. Qi, X. Zhu, H. Pan, X. Zhang, S. Bano, Y. Yuan, *A high-efficiency energy regenerative shock absorber using helical gears for powering low-wattage electrical device of electric vehicles*, Energy, **159** (2018) 361 – 372.
4. S. Singh, N. V. Satpute, *Design and analysis of energy-harvesting shock absorber with electromagnetic and fluid damping*, J. Mech. Sci. Technol., **29**(4) (2015) 1591 – 1605.

5. R. Wang, R. Ding, L. Chen, *Application of hybrid electromagnetic suspension in vibration energy regeneration and active control*, J. Vib. Control, **24**(1) (2018) 223 – 233.

6. E. Asadi, R. Ribeiro, M. B. Khamesee, A. Khajepour, *A new adaptive hybrid electromagnetic damper: Modelling, optimization, and experiment*, Smart Mater. Struct., **24**(7) (2015) 075003.

7. Y. Pan, T. Lin, F. Qian, C. Liu, J. Yu, J. Zuo, L. Zuo, *Modeling and field test of comact electromagnetic harvester for railroad transportation*, Appl. Energy., **247** (2019) 309 – 321.

8. H. L. Guntur, W. Hendrowati, S. Mochammad, *The Effect of Using Current Stabilizer to the Dynamic Characteristic of a Regenerative Shock Absorber*, Appl. Mechanics and Materials- Trans Tech Publications, **758** (2015) 137 – 142.

9. R. Zhang, X. Wang, S. John, *A Comprehensive review of the techniques on regenerative shock absorber systems*, Energies, **11(5)** (2018a) 1167.

10. R. Zhang, X. Wang, Z. Liu, *A novel regenerative shock absorber with a speed doubling mechanism and its Monte Carlo simulation*, J. Sound Vib., **417** (2018b) 260 – 276.

11. J. Mi, L. Xu, S. Guo, M. A. Abdelkareem, L. Meng, *Suspension performance and energy harvesting property study of a novel railway vehicle bogie with the hydraulic-electromagnetic energy-regenerative shock absorber* (No. 2017-01-1483), SAE Technical Paper (2017a).

12. J. Mi, L. Xu, S. Guo, L. Meng, M. A. Abdelkareem, *Energy harvesting potential comparison study of a novel railway vehicle bogie system with the hydraulic-electromagnetic energy-regenerative shock absorber*, ASME Joint Rail Conference (2017b).

13. M. Demetgul, I. Guney, *Design of the hybrid regenerative shock absorber and energy harvesting from linear movement*, J. Clean Ene. Tech., **5(1)** (2017) 81 – 84.

14. Z. Zhang, X. Zhang, W. Chen, Y. Rasim, W. Salman, H. Pan, C. Wang, *A high-efficiency energy regenerative shock absorber using supercapacitors for renewable energy applications in range extended electric vehicle*, Appl. energy, **178** (2016) 177 – 188.

15. J. Zou, X. Guo, L. Xu, G. Tan, C. Zhang, J. Zhang, *Design, modeling, and analysis of a novel hydraulic energy-regenerative shock absorber for vehicle suspension*. Shock Vib. (2017).

16. X. D. Xie, Q. Wang, *Energy harvesting from a vehicle suspension system*, Energy, **86** (2015) 385 – 392.

17. L. Chen, D. Shi, R. Wang, H. Zhou, *Energy conservation analysis and control of hybrid active semiactive suspension with three regulating damping levels*, Shock Vib., (2016).

18. N. V. Satpute, S. N. Satpute, L. M. Jugulkar, *Hybrid electromagnetic shock absorber for energy harvesting in a vehicle suspension*, J. Mech. Eng. Sci., **231**(8) (2017) 1500 – 1517.

Investigation of the Vibration Properties of Concrete Elevated Hospital Helipads

Wiesław KRZYMIEŃ
Institute of Aviation, Al. Krakowska 110/114, Warsaw,
wieslaw.krzymien@ilot.edu.pl

Sławomir CIEŚLAK
Institute of Aviation, Al. Krakowska 110/114, Warsaw,
slawomir.cieslak@ilot.edu.pl

Abstract

Elevated helipads at hospitals offer the possibility of rapid transport and assistance to persons injured in accidents or severely ill. Such helipads may have a diverse structure and location-depending on the possibilities of the hospital environment, including the vicinity of other buildings. Vibroacoustics Laboratory of the Institute of Aviation performed the measurement of the vibration properties of several helipads of varying degrees of construction. These tests were intended to determine the vibration properties of the helipads as well as the building, as an attempt to access the impact of the vibrations induced during a helicopter's landing and take-off on the construction of the helipad, the building and its equipment. This paper presents the tests and some results of the measurements made with a modal hammer, carried out on two new elevated helipads, built on the building's roofs and an estimation of the impact of the helicopter on its construction at the stage of design and construction of the helipad.

Keywords: elevated helipads, ground vibration tests, vibration measurements

1. Introduction

The air transport system for injured or severely ill people facilitates the provision of rapid and specialized medical assistance. The general conditions for the functioning of air transport for medical purposes are governed by the Act of 28.09.2006 on State Medical Rescue (Journal of Laws 191, item 1410) [1] and the health-related regulation of 3.11.2011 in the hospital emergency department (Journal of Laws 2019 item. 1213) [2]. The requirement to provide a short transport time determine the location of the landing fields as close to the hospital as possible. In addition, it is important to ensure the safe operation on the landing fields for 24 hrs under the acceptable weather conditions.

In Poland there are currently about 240 working hospital helipads and among them there are 31 elevated helipads: 25 on buildings (Figure 1) and 6 free-standing (Figure 2) – they all operate as 24 hrs ready.

Due to the requirements and the area of operation of the Medical Air Rescue (polish: LPR), the increase in the number of elevated helipads can be expected. Most of them will be built on hospital buildings. An example of a currently built helipad located on a building is the South Hospital in Warsaw is presented in Figure 1.

Two basic solutions for hospital landings are:
- ground helipads (requiring a lot of spaces),
- elevated helipads - most often used in built-up areas (near the city centre).

Figure 1. Elevated helipad (under construction) on South Hospital in Warsaw
(10.2018)

Figure 2. Elevated free-standing helipad near hospital in Krakow [3]

Elevated helipads require relatively small area and allow to shorten the distance between the helicopter and the Hospital Emergency Department (polish: SOR). Their disadvantages are: high cost of construction, requirements for safe operation [4], high costs of winter maintenance and the possibility of dangerous effects in case of a helicopter accident during take-off or landing.

The placement of the helipad on the building makes the helicopters' taking-off and landing, which are important sources of vibrations and noise, directly impact the building. The impact of the helicopter on the closest environment during landing and shutdown of the drive and then start and take-off follows from:

- the noise of the engine/engines,
- the noise of rotor blades (endings),
- the noise of the tail propeller,
- pulsation of the blow from the blade,
- loads from "hard landing",
- the vibration of the main rotor transferred to the landing gear by the chassis.

Elevated helipads on the roofs of buildings depending on the executive capacity and the strength properties of the building can be built as:

- concrete construction - heavy, planted on several concrete poles,
- steel construction - light, on a trill structure (Figure 3).

Figure 3. The steel structure of the hospital helipads on Lindley Street in Warsaw

The steel-structure-based helipads typically have vibration isolation elements. Their construction (built-up with multiple components) is characterised by a slightly higher vibration damping factor. These are the reasons for a decision to study the real vibration properties of concrete helipads. Their design is part of the building's design

and vibrations from the helicopter can be more easily transmitted to lower floors, where operating rooms or vibration-sensitive medical equipment can be located.

The important and recommended feature of the helipads is an airgap - the space between the roof of the building and the landing plate. In the case of a strong wind an airgap stabilizes the airflow around the building and the landing area increasing safety and facilitating the execution of a landing and take-off of a helicopter. The purposes of the airgap are to raise the landing plate and to reduce the stiffness of the support of the landing plate (in particularly: bending of the poles).

The recently introduced standards PN-B-02170_2016 [5] and PN-B-02171_2017 [6] determine the method of measurement and recommended vibration levels on the floor of different rooms of buildings in the area of influence of e.g. railway tracks, factories or construction sites. Measurements should be carried out for a frequency range up to 100 Hz.

During the start-up and braking of the main rotor, vibrations generated by the blades can be transmitted to the ground. Variable rotor rotations and wind can cause helicopter's resonant vibrations on the chassis. This is usually the case for helicopters with three-axis articulated rotor heads (such measurements were made in IoA for the Mi-2 helicopter). In the case of EC-135 helicopters the procedures and the equipment for the torsional blade and balancing of the carrier rotor and the tail fan prepared by the manufacturer ensures that vibrations are minimized across the range of the rotating frequencies of the rotor (and multiples of the number of blades). These excitations are small, but the low damping of the structure can cause vibration of the helipad move to the building [7].

The authors of this paper have made preliminary measurements of the environmental impact of the EC-135 helicopter to estimate the type and magnitude of the impact of the helicopter on the environment [8]. This article provides examples of the measurement results of the vibration properties of concrete helipads on buildings and vibrations transmitted to the building.

2. Scope of research

The research of the vibration properties of the helipad and the upper part of the building is a way of estimating the frequencies and vibration levels that may occur during landing and take-off of a helicopter.

Measurements were made in two steps:
- determination of the shape of the free vibrations of the helipad,
- assessment of the transmission of vibrations from the landing plate to the floor of the storys under the helipad.

The investigations were carried out using sensor signal analysis after exciting the object with a pulse (a 5 kg modal hammer) in the range up to approx. 150 Hz. Figure 4 shows the modal hammer as well as a graph of the force's waveform for two different strokes – force impulses, from which it is apparent that the pulse time does not depend on the impact of force.

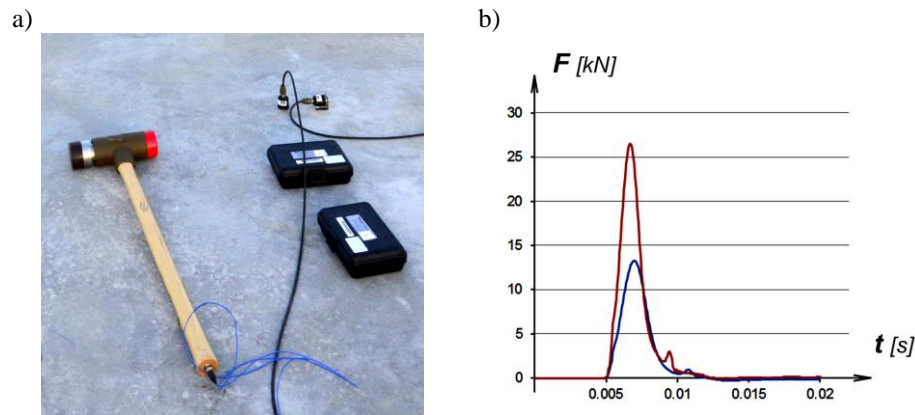a)   b)

Figure 4. Modal hammer and sensors used in the measurements on the helipads (a)
and an example of force pulse waveform for two different strokes (b)

In the case of a single construction (which is the concrete landing structure), this method of measurement produces sufficient and reliable results. The study used LMS measurement equipment and software.

3. Test results

The free vibration tests of helipads (including poles) were designed to determine the basic shapes with the lowest vibration frequencies. The sensors are located on the plate (in the centre and approx. 1 m from its edge), on the bases of the poles at the roof level and one sensor on the floor below the roof in the vertical axis of the helipad.

Figure 5 shows the model for visualizing the shape of vibrations: the displacements of the nodes correspond to the amplitude of the measured acceleration of vibration on the object. The measurement direction is given with the sensor numbers.
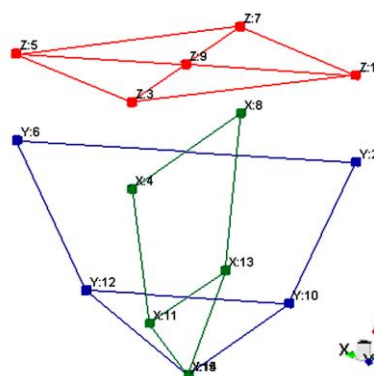

Figure 5. Model for visualizing the vibration shape of the tested helipad

The basic measured vibration figures, short description of the shape, frequency and damping coefficients in the range up to 100 Hz are summarized in Table 1. Figure 6 illustrates some examples of the measured shapes of vibrations.
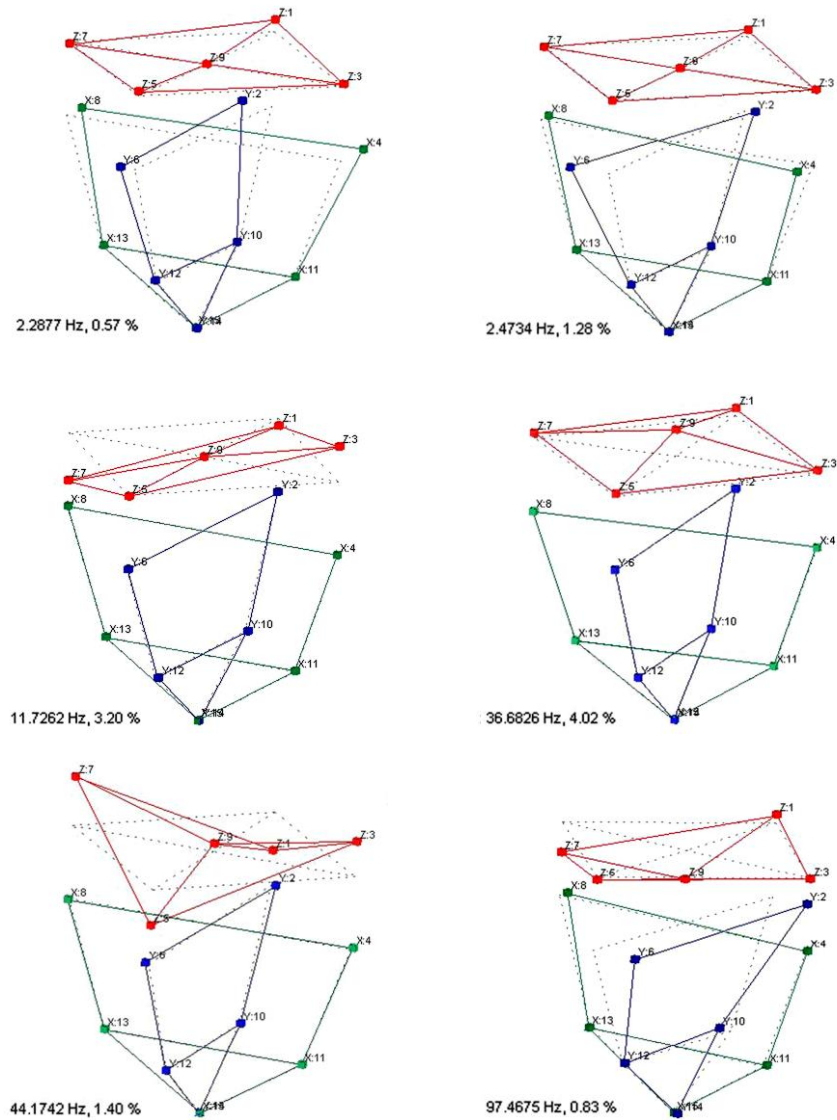

Figure 6. Examples of the shapes of the measured helipad vibrations

Table 1. Overview of the form of helipad and building vibrations

No.	Shape of vibration	f [Hz]	Damping coeff.
1	Poles bending in directions X i Y	2.28	0.57%
2	Torsion around the Z axis (vertical)	2.47	1.28%
3	Swinging the plate round X axis	11.73	3.20%
4	Vertical vibration the middle of the plate	36.68	4.02%
5	Plate bending in X and Y axis	44.17	1.40%
6	Vertical displacement of the plate	70.55	2.05%
7	Poles bending in direction X	94.74	0.95%
8	Poles bending in direction Y	97.47	0.83%

Measurements of the transmission of the vibrations from the helipad to the lower stories of the building were carried out at the hospital in Lublin. The building was in the process of equipping and at the courtesy of the Hospital Directorate the measurements were carried out for rooms in almost ready-to-use state, however the landing area was not yet completed.

The sensors have been located on the floor in the rooms under the helipad landing area on the two highest stories of the 5-story building: in the vertical axis of the landing area and in the middle of three adjacent rooms. Figure 7 shows the arrangement of the sensors as a model to visualize the amplitude of vibration at the measuring points. Sensor No. 1. is placed in the center of the landing plate, sensors No. 2 - 6 on the 4th floor, and sensors No. 12 - 15 on the 3rd floor. All sensors measured acceleration of vibrations in the vertical direction.
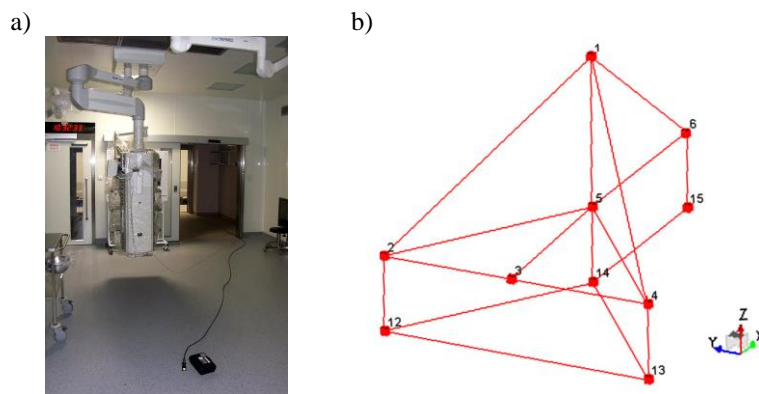
a) b)

Figure 7. Sensor No 4. on the floor of operating theatre (a) and the arrangement of sensors - model visualizing the position and amplitude of vibration transmitted from helipad (b)

Figure 8 shows amplitude-frequency characteristics obtained on the basis of signal from the sensors after impulse excitation in the centre of the helipad.
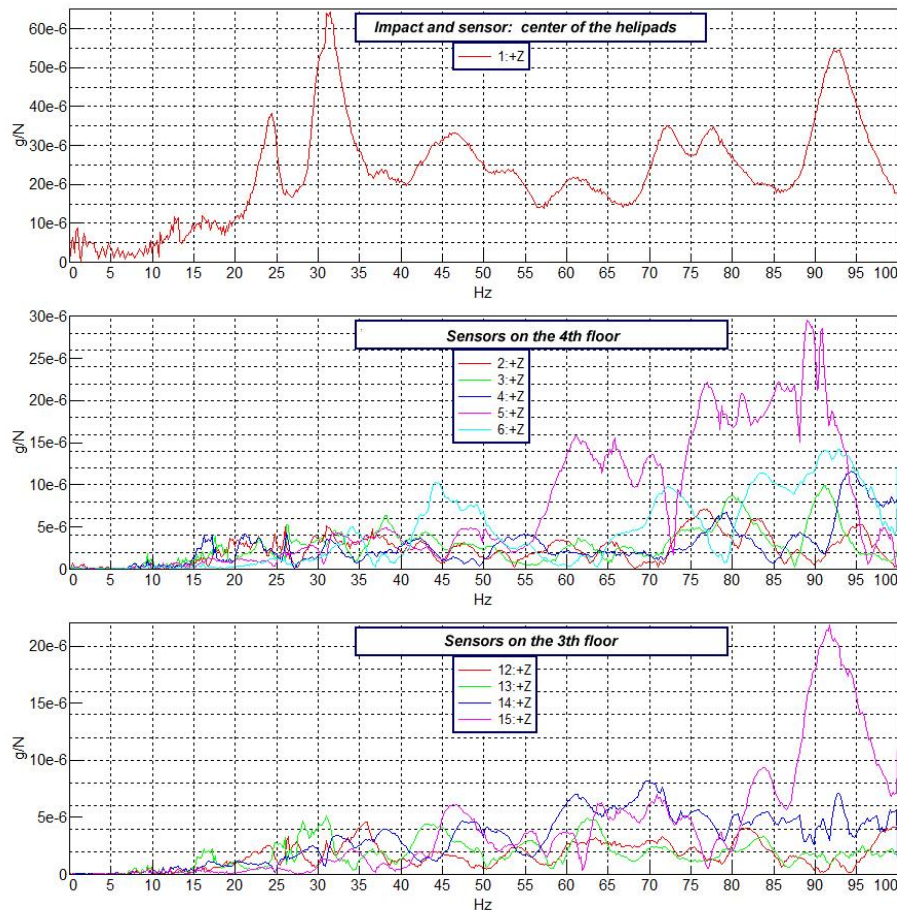

Figure 8. Frequency-amplitude characteristics from sensors

Based on the graphs, it can be concluded that a small part of the vibrations is transmit from the helipad to the lower story's. On floors there are vibrations of different frequencies which are damped and do not show the nature of individual resonances.

During the tests [8], a typical landing of EC-135 helicopter was recorded. The landing took place "at the tip of the left skid", which makes it usually gentle and thus does not cause dynamic (impact) loading of the landing pad.

In difficult weather conditions a "hard landing" is possible. The point effect of a force pulse which occurs during the hard landing is simulated by a modal hammer impact on the helipad well enough. In this way, without the involvement of the

helicopter and its crew, it is possible to measure the vibration of the landing pad and the building structure excited as a result of the force impulse.

The final verification of the vibration level in the building can only be carried out during helicopter's take-off and landing operations, however, their practical implementation is associated with a temporary disruption of the hospital's operation - they require a special helicopter landing and placing sensors in places (rooms) that require aseptic or special access e.g. operating rooms or rooms with specialized testing equipment.

A separate threat to the building, patients and hospital staff are emergency conditions, such as: helicopter impact on the helipad or turbulence from the rotor and wind in the event of an unusual landing or take-off.

4. Conclusions

As a result of the measurements, information about the dynamic properties of the helipad was obtained, i.e. the frequencies and forms of free vibrations were determined using the method of the force excitation with a modal hammer.

The impact of a helicopter on the environment may not be burdensome if the flights taking place no more than once a day. However the involvement of helicopters in the field of transport of sick and injured people will increase.

Compliance with the standards and recommendations should be planned in advance, but adequate data is needed to assess the impact of helicopters as well as a preliminary verification of vibration properties is needed in order to introduce any changes in the construction of the helipad.

Based on the measurements carried out, no significant transmission of vibrations (excited by a modal hammer) through the landing pad structure to the building floors was found, which indicates the extend to which vibrations are dampened by the building structure and its equipment.

The main rotor is the main source of vibrations excited by the helicopter. The EC-135 helicopters used by the Air Ambulance Service can be a source of vibrations with a nominal rotor operating frequency of about 6.5 - 6.8 Hz (depending on the version) and a multiple of the number of blades ± 1. During starting and braking of the helicopter's rotor due to the changing frequency of excitation, there may be short-term excitations of vibrations resulting from passing through individual resonance frequencies of the structure (from 0 to 34 Hz). The engine starts for approx. 1 minute, and it brakes for approx. 1.5 minutes, therefore the resonance passages are fast.

The final verification of the impact of the helicopter on the construction of the helipad and the hospital building would be conducted by an analysis of the signal from many sensors during the landing and take-off of the helicopter.

References

1. Law from 8.09.2006 r. about National Emergency Medical Services (JoL 191 item 1410).
2. Ordinance Min. of Health from 27.06.2019 regarding the hospital emergency department (JoL 2019 item 1213).

3. https://www.google.pl/maps/@50.0131343,20.0021003,3a,75y,212.99h,91.07t/.

4. Federal Aviation Administration, US Department of Transportation, 2012, Heliport Design -AC 150/5390-2c, Chapter 4-Hospital Heliports.

5. Standard PN-B-02170_2016, *Assessment of the harmfulness of vibrations transmitted through the ground to buildings*.

6. Standard PN-B-02171_2017, *Assessment of the impact of vibrations on people in buildings.*

7. K. Wąchalski, *Assessment of the current construction conditions for elevated helipad on hospital buildings in Poland*, Transactions of the Institute of Aviation, **3** (244) (2016) 189 – 201.

8. W. Krzymień, S. Cieślak, *Initial analysis of helicopter impact on hospital helipads*, Transactions of the Institute of Aviation, **3**(256) (2019) 14 – 23.

9. Law from 8.09.2006 about National Emergency Medical Services (JoL 191 item 1410).

Identification of Plastic Deformations in Carbon Steel Elements Using the Filtered Barkhausen Noise Signal

Jacek DYBAŁA

Warsaw University of Technology, Faculty of Automotive and Construction Machinery Engineering, Institute of Vehicles, 84 Narbutta St., 02-524 Warsaw, Poland, jacek.dybala@pw.edu.pl

Krzysztof NADULICZ

Military Institute of Armament Technology, 7 Wyszynski St., 05-220 Zielonka, Poland, naduliczk@witu.mil.pl

Abstract

The paper presents new approach to processing the Barkhausen Noise signal in order to detect and identify plastic deformations in carbon steel. A new automatic method of Barkhausen effect signal filtration was investigated. Apart from a classical measurement of Barkhausen effect signal, for which the RMS value is assumed, the signal waveform factor was also used in analyzes. The developed approach to processing the Barkhausen Noise signal has made it possible to obtain more useful diagnostic data than those obtained from the raw signal.

Keywords: non-destructive evaluation, plastic deformation, Barkhausen Noise, signal processing

1. Introduction

One of active diagnostic magnetic methods is Barkhausen Noise (BN) method based on the assessment of the microstructural properties of ferromagnetic materials [1]. BN is generated during jumps of magnetic domain boundaries, so-called Bloch walls, when domains set their orientation to the direction of an external magnetizing field [2, 3]. BN depends on different factors, such as material microstructure, stress state and material composition, that affect the domain structure of ferromagnetic material. Thereby, it is possible to use BN for assessment of states of the stresses and the magnitude of plastic deformations [4]. Unfortunately, the measured raw Barkhausen Noise signal often contains some components that are not related to the state of the stress and the scale of plastic deformation [5]. Therefore, it is necessary to develop an effective method of filtering the raw BN signal to remove unnecessary disturbances and obtain useful diagnostic information. The article investigates the effectiveness of the new approach to processing the Barkhausen effect signal. The use of an additional reference coil, and adaptive filtration, and Empirical Mean-based Signal Decomposition method enabled the elimination of most disturbances occurring in the raw BN signal. The filtered BN signal was used to determine a waveform factor, whose values correlate with the values of plastic deformations of carbon steel test-pieces.

2. Details of experiments

A unit generating low-frequency vibrations of the magnetic field consisted of a sinusoidal signal generator of RIGOL company, a power amplifier with amplification rate equal to 7 and a coil including 800 turns of 0.8 mm diameter winding wire wound on "UU-93-K" carcass of FERYSTER Sp. z o. o. Company. The carcass is mounted onto a "U" type core made by gluing three cores of "I" type. The channel measuring the Barkhausen effect signal uses an acoustic amplifier with amplification rate of 100 and a pickup coil built from 2400 turns of 0.15 mm diameter winding wire applied on the plastic carcass with external and internal diameters of 29 mm and 16 mm respectively and height of 15 mm. A second coil with the same parameters as the pickup coil was also connected to the measuring system. This additional coil played the role of the reference coil. The set-up was powered by a three-channel laboratory power supply TP-3305U of Twintex Company. A voltage in the form of a harmonic signal with frequency 2 Hz and amplitude 3.5 V excited vibrations of the magnetic field. Signals from both coils were recorded in digital form by the 16-channel recorder of HIOKI Company, model MR8847A, with a sampling frequency 1 MHz and with a low-pass filter (500 kHz cutoff frequency). The recording time during a single measurement was 2 s. Diagram of the set-up used for measurements is presented in Figure 1.
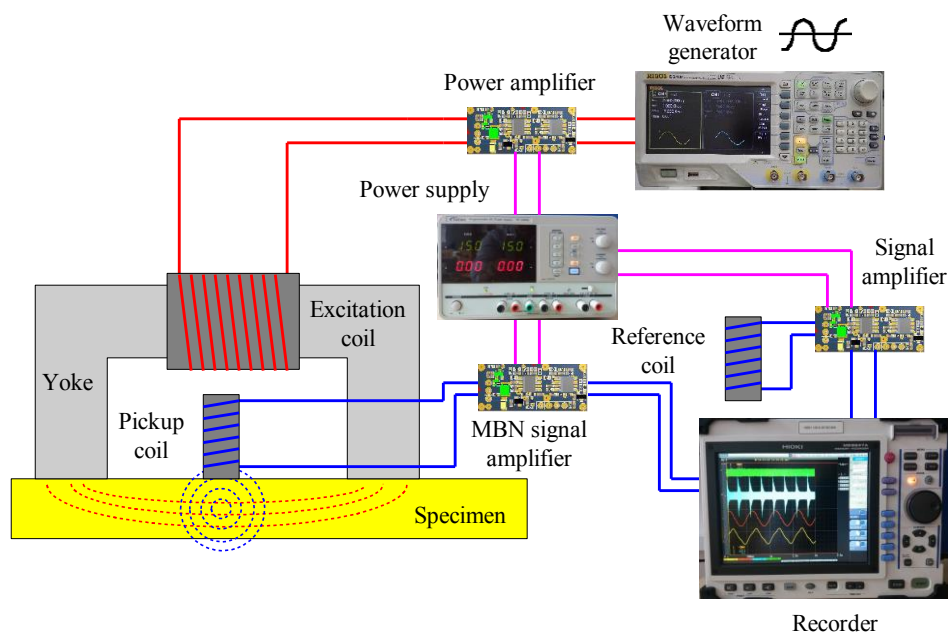

Figure 1. Block diagram of the set-up used for measurements

The carbon steel S355J2 is taken as the testing material in this study. The chemical composition of S355J2 carbon steel is as follows: carbon (C) 0.20%, sulphur (S) 0.04%, phosphorus (P) 0.04%, manganese (Mn) 1.5%, silicon (Si) 0.5%, chromium (Cr) 0.03%, nickel (Ni) 0.03%, cobalt (Co) 0.2%, copper (Cu) 0.3%. Test-pieces had dimensions 330 x 30 x 3 mm and were cut out with a guillotine from a sheet steel S355J2. The experiment was carried out with the use of Zwick-Roell Z100 testing machine in the tensile test mode. The sample was subjected to an extension test aimed to produce a plastic deformation of the sample for enabling the measurement of the magnetic effects. The plastic deformation of the test-piece has been gradually increased during the experiment. The pickup coil was mounted on the test-piece. A yoke with a coil generating low-frequency vibrations of the magnetic field (excitation coil) was placed above the pickup coil. The additional reference coil was placed outside the test-piece, at a distance of 65 mm from the pickup coil. BN signal measurements were carried out on loaded test-pieces (in-situ) at the following values of relative plastic deformations: 0 %, 1.52 %, 3.03 %, 4.55 %, 6.06 %, 7.58 % and 9.09 %.

3. Measurement results

Figures 2 and 3 show exemplary waveforms and amplitude spectra of the signals recorded by the pickup coil (BN signal) and the reference coil during the experiment. Amplitude spectra clearly show some high-frequency disturbances of varying intensity in both measured signals. In particular, there are clearly visible disturbances in the form of harmonic signals with frequencies around 16 kHz, 48 kHz and 127 kHz.
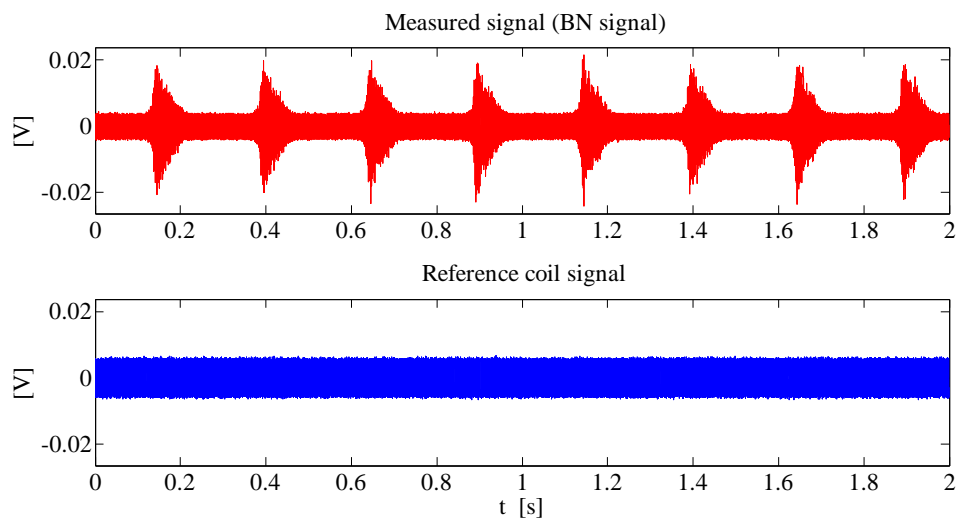

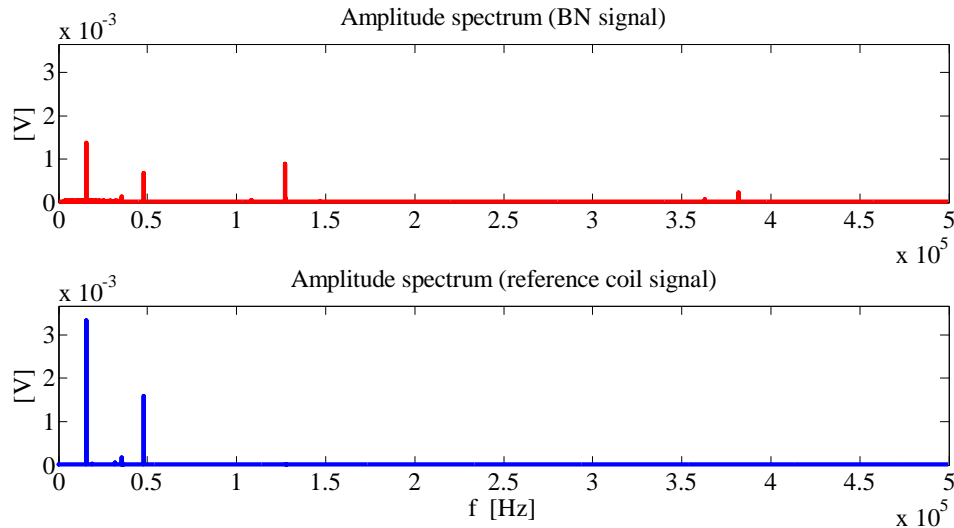Figure 2. Waveforms of measured BN signal and reference coil signal

Figure 3. Amplitude spectra of measured BN signal and reference coil signal

Conventional diagnostic use of Barkhausen effect signal is based on the use of the RMS value (Root Mean Square) of the measured signal:

$$u_{\text{RMS}} = \sqrt{\frac{1}{T}\int_0^T u^2(t)dt} \approx \sqrt{\frac{1}{N}\sum_{i=1}^N u_i^2} \tag{1}$$

where N is the number of samples and u_i are the measured values.

Figure 4 shows the correlation of the RMS value of the measured raw BN signal with plastic deformations of test-piece.

It may be noted that in the case of the plastic deformation value assessment, the RMS value of raw BN signal cannot be treated as fully useful diagnostic parameter. The RMS value of the raw BN signal does not change in a monotonic way. The poor diagnostic usefulness of raw BN signal is probably due to disturbances recorded by the pickup coil. In order to eliminate the disturbances, a two-stage BN signal filtration procedure was developed.

The first stage performs an adaptive filtration using a finite impulse response filter (FIR filter). The goal of adaptive filtering systems is to eliminate signal-disturbing components and to obtain an undistorted desired signal [6]. The adaptive filtration scheme is shown in Figure 5.

The second stage extracts the low-frequency signal component of the FIR-filtered BN signal. An Empirical Mean-based Signal Decomposition method [7] determines this signal using the technique introduced in Empirical Mode Decomposition method for empirical determination of signal envelopes [8]. The processing algorithm of the FIR-filtered BN signal consists of the following steps:

Step 1: Identification of all local extremes (maxima and minima) of FIR-filtered signal $x(t)$.

Step 2: Connecting all local maxima (respectively minima) with a line known as the empirically determined upper envelope $E_U(t)$ (respectively the lower envelope $E_L(t)$). Local maxima (minima) are connected with a line by using piecewise cubic interpolation (Piecewise Cubic Hermite Interpolating Polynomials – PCHIP).

Step 3: Constructing the mean of empirically determined upper and lower envelopes (the low-frequency signal component) $d(t) = 0.5 \cdot (E_U(t) + E_L(t))$. The low-frequency component of the FIR-filtered BN signal is treated as the (finally) filtered BN signal.
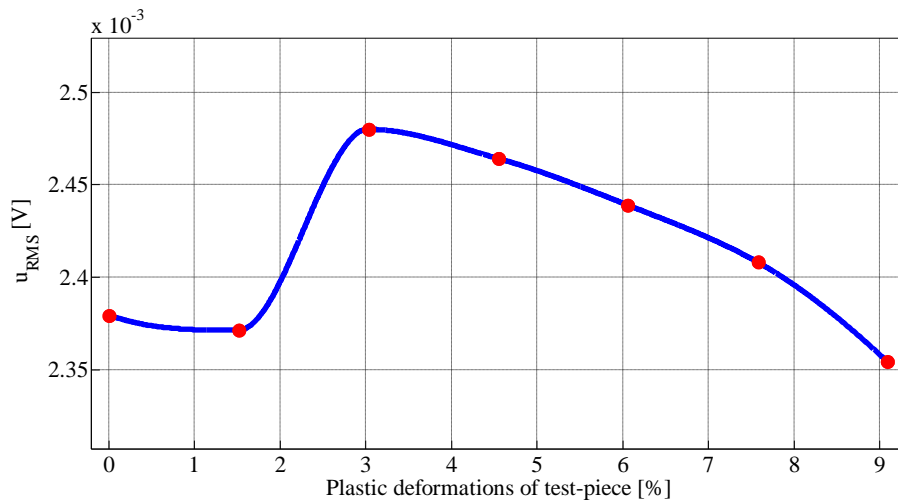

Figure 4. Dependence of RMS value of the measured BN signals on plastic deformations of test-piece
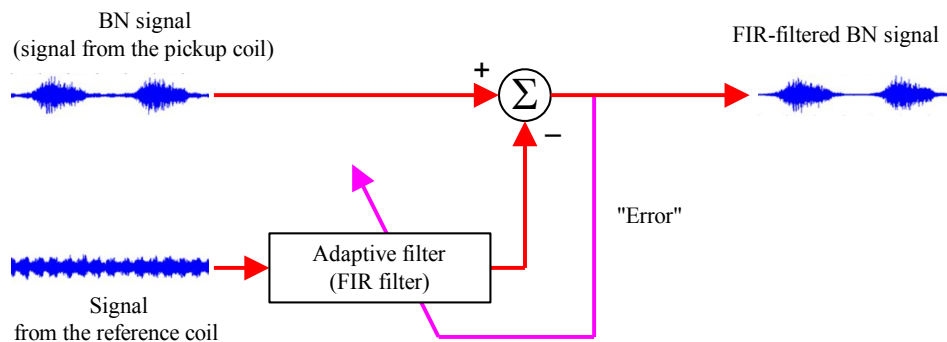

Figure 5. Adaptive filtration scheme

Figure 6 and 7 show waveforms and amplitude spectra of exemplary raw and filtered BN signals. It is clearly visible how the level of disturbances in the filtered BN signal is reduced. This creates a possibility for a better use of the diagnostic information contained in the Barkhausen effect signal.

Based on the filtered BN signal, the waveform factor was determined, defined by the formula:

$$u_{\text{WF}} = \frac{u_{\text{RMS}}}{u_{\text{AVE}}} = \frac{\sqrt{\dfrac{1}{T}\displaystyle\int_0^T u^2(t)dt}}{\dfrac{1}{T}\displaystyle\int_0^T |u(t)|dt} \approx \frac{\sqrt{\dfrac{1}{N}\displaystyle\sum_{i=1}^N u_i^2}}{\dfrac{1}{N}\displaystyle\sum_{i=1}^N |u_i|} \tag{2}$$

where N is the number of samples and u_i are the measured values.

Figure 8 shows the correlation of the waveform factor of the filtered BN signal with plastic deformations of test-pieces. It may be noted that the waveform factor of the filtered BN signal can be treated as fully useful diagnostic parameter. The monotonic change in the waveform factor value and the correlation of its value with the plastic deformation of the test-piece is clearly visible.
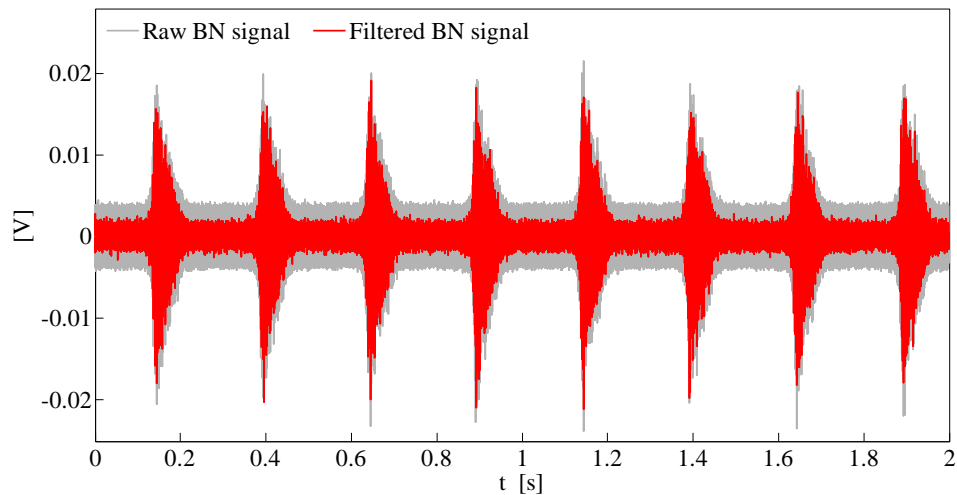
Figure 6. Waveforms of exemplary raw BN signal and filtered BN signal
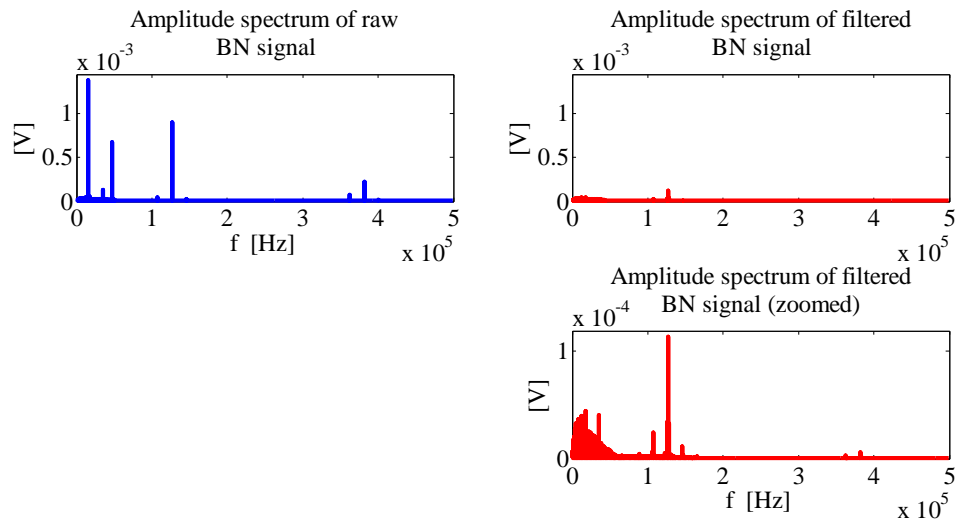
Figure 7. Amplitude spectra of exemplary raw BN signal and filtered BN signal

Figure 8. Dependence of waveform factor of the filtered BN signals on plastic deformations of test-piece

4. Conclusions

The original method of the Barkhausen effect signal filtration was developed to eliminate disturbances present in the signal recorded by the pickup coil. It was proved that applied filtration of BN signal led to better use of diagnostic information contained

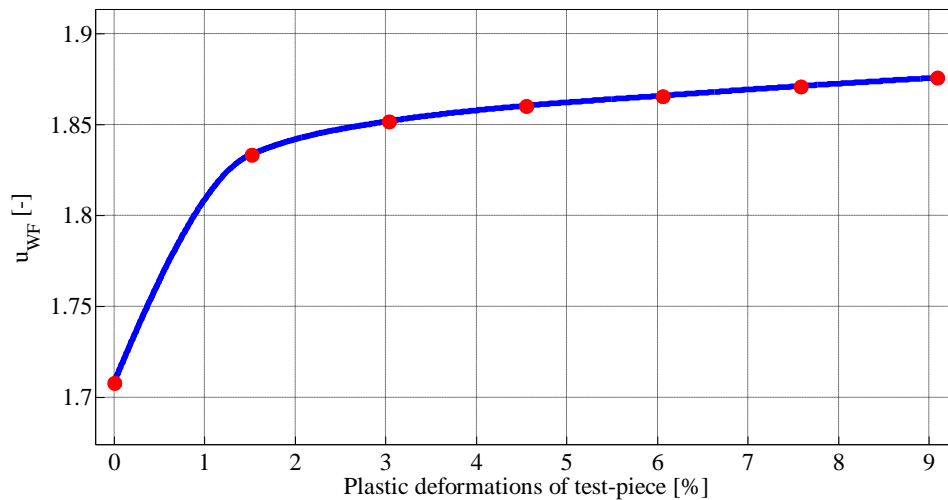in this signal. In case of the necessity to assess the plastic deformation value of the element made of carbon steel, the waveform factor of the filtered BN signal can be treated as useful diagnostic parameter. The waveform factor is a diagnostic parameter convenient for interpretation, because its value is positively correlated with the amount of plastic deformation (its value increases with the increase in the value of plastic deformation).

References

1. J. C. Sánchez, M. F. Campos, L. R. Padovese, *Magnetic Barkhausen emission in lightly deformed AISI 1070 steel*, Journal of Magnetism and Magnetic Materials, **324**(1) (2012) 11 – 14, https://doi.org/10.1016/j.jmmm.2011.07.014.

2. D. C. Jiles, *Dynamics of domain magnetization and the Barkhausen effect*, Czechoslovak Journal of Physics, **50**(8) (2000) 893 – 924, https://doi.org/10.1023/A:1022846128461.

3. S. Santa-aho, A. Laitinen, A. Sorsa, M. Vippola, *Barkhausen Noise Probes and Modelling: A Review*, Journal of Nondestructive Evaluation, **38**(94) (2019), https://doi.org/10.1007/s10921-019-0636-z.

4. H. Chen, S. Xie, Z. Chen, T. Takagi, T. Uchimoto, K. Yoshihara, *Quantitative nondestructive evaluation of plastic deformation in carbon steel based on electromagnetic methods*, Materials Transactions, **55**(12) (2014) 1806 – 1815, https://doi.org/10.2320/matertrans.M2014173.

5. D. Blažek, M. Neslušan, M. Mičica, J. Pištora, *Extraction of Barkhausen noise from the measured raw signal in high-frequency regimes*, Measurement, **94** (2016) 456 – 463, http://dx.doi.org/10.1016/j.measurement.2016.08.022.

6. B. Widrow, J. R. Glover, J. M. McCool, J. Kaunitz, C. S. Williams, R. H. Hearn, J. R. Zeidler, E. Dong Jr., R. C. Goodlin, *Adaptive Noise Cancelling: Principles and Applications*, Proceedings of the IEEE, **63**(12) (1975) 1692 – 1716, http://dx.doi.org/10.1109/PROC.1975.10036.

7. J. Dybała, J. Komoda, *Empirical signal decomposition methods as a tool of early detection of bearing fault*, in: Eds. A. Timofiejczuk, F. Chaari, R. Zimroz, W. Bartelmus, M. Haddar, Advances in Condition Monitoring of Machinery in Non-Stationary Operations, Applied Condition Monitoring, **9**, Springer International Publishing AG, Cham 2018, 147 – 156, https://doi.org/10.1007/978-3-319-61927-9_14.

8. N. E. Huang, Z. Shen, S. R. Long, M. C. Wu, H. H. Shih, Q. Zheng, N. C. Yen, C. C. Tung, H. H. Liu, *The empirical mode decomposition and the Hilbert spectrum for nonlinear and non–stationary time series analysis*, Proceedings of the Royal Society of London, Series A – Mathematical, Physical and Engineering Sciences, **454**(1971) (1998) 903 – 995, http://dx.doi.org/10.1098/rspa.1998.0193.

Recommendation for the Design of Composite Covers which Protect the Chassis of a Rail Vehicle

Mateusz JUZUŃ

Silesian University of Technology, Institute of Fundamentals of Machinery Design,
S. Konarskiego 18A, 44-100 Gliwice, mateusz.juzun@polsl.pl,
Alstom Konstal S.A., Metalowców 9, 41-605 Chorzów.

Wojciech CHOLEWA

Silesian University of Technology, Institute of Fundamentals of Machinery Design,
S. Konarskiego 18A, 44-100 Gliwice, wojciech.cholewa@polsl.pl

Abstract

Fragments of research to formulate criteria allowing for the rational design of covers to protect against the destructive impact effects of small, sharp elements, are discussed. The motivation for this research was the result of the analysis of damage to composite covers which protect the chassis of a modern traction vehicle, moving at high speed on Polish railway routes. Such covers must have appropriate strength properties and high surface resistance to external damage, while limiting the influence of the impact of foreign elements on the cover, and the impact of external sources of noise and vibrations on the interior of the vehicle. They have a sandwich structure and are made of a polymer composite. General guidelines for the design of covers having the required properties are not known.

A method of analyzing the resistance of the cover to damage associated with the impact of elements with sharp edges and irregular shapes, using the LS-Dyna software, has been proposed. For the needs of the proposed method, a general model of the cover structure has been introduced. The assumptions adopted in determining the field of possible solutions are discussed. Particular attention is paid to the required structure of the cover, allowing for the differentiation of its properties observed in the longitudinal and transverse directions of the vehicle. Selected conclusions resulting from the research carried out so far, are presented.

Keywords: composite covers, vibroacoustic insulation of composite covers, impact resistance

1. Introduction

Railway vehicles which move on ballasted lines during operations, are exposed to the impacts of stones which constitute the mentioned ballast. Their high speed, very often above 200 km/h, causes air to lift the stones and to throw them against the equipment and structural parts located on the underframe. The impact of the ballast may cause damage to the impacted area and in some particular cases, may cause a serious incident. The next indicated inconvenience is noise caused by the air and the impacts. Because of these points, many manufactures equip their product with additional protective covers which are fixed to the underframe to isolate them from the destructive external factors. [1]

This protection may be realized in a few different ways, but mostly by using special steel plate or a polymer composite sandwich. Composites present some advantages compared to steel because of their better noise reduction, as well being lighter. That's why modern trains are often protected by this material. On the other hand, using polymer

composite materials to protect the chassis from the aggressive environment makes it necessary to be precisely sure of their properties because they are anisotropic. Hence there is a need to conduct simulations and real tests to confirm the efficiency and impact resistance of the designed cover.

According to this specific use of the composite, there is a lack of clear requirements and specifications which could be used by designers to increase the reliability of the mentioned covers. To study the damage features, one of the covers was unmounted from the train after a few months in service. This enabled the types and dimensions of the damages to be observed, and detailed microscopic observations were conducted. A few different types of damages were indicated, but during this investigation, smooth "cracks" were considered (Figure 1a) because of their overwhelming amount. This kind of damage is caused by lifting ballast, as indicated earlier, with impact speeds of about 70 m/s. To ensure safety of the underframe's equipment, covers must present an adequate level of strength, which is described in detail as the stiffness, coefficient of friction, and direction of the fibers.

As well as high impact resistance, there are also other requirements that should be met by the composite cover. According to European Regulations, all combustible parts which are attached to trains need to meet requirements for the material's fire behavior. One example of these requirements, which trains need to fulfil, is the European Standard - EN45545: Railway applications – Fire protection on railway vehicles. The objectives are to minimize the probability of a fire starting, to control the rate and extent of fire development, and to minimize the impact of the products of a fire on passengers. [2, 3] The materials must also meet the standards based on existing Fire Safety regulations for railway vehicles from the International Union of Railways (UIC).
Last but not least, another advantage of using a composite cover instead of a steel one, are the acoustic properties – the absorption and reflection of acoustic waves, which increases the comfort of the passengers. Many of the above presented requirements were analysed during different simulations and analyses performed to try to define a set of universal requirements for new designed composite covers.

2. Methods and materials

As a first step, a detailed analysis of the real existing cover was performed. One example of the typical damage is presented in Figure 1a.

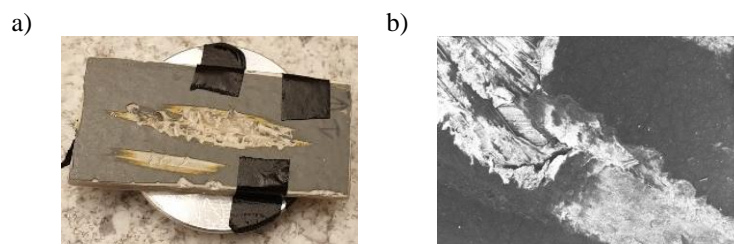a)   b)

Figure 1. a) Specimen, example of longitudinal damage. Sample prepared for SEM observations. b) Detailed view of the damaged area

This was chosen and taken for further analysis. For the selected specimen, an SEM observation was carried out and an example view is presented in Figure 1b. It was noticed that all of the scratches are turned towards the vehicle's axis of movement. Taking this into account, it was proposed that the degree of damage depends on the directionality of the fibers in the outer layer. After a detailed analysis of the composite cover's structural damages, it was observed that the damaged edges looked ragged (Figure 1b). This means that during the scratch, the fibers were pulled out of the composite which increased the damaged area. This is because that in existing composites, the external plies are made from chopped strand mat with a chaotic strand orientation. To decrease the area of damages, unidirectional external plies could be used. In this configuration, a scratch will occur, but it will only produce a small area of damage.

2.1. *Influence of Coefficient of Friction*

As the next factor, the friction accompanied with the impact against the external surface was studied. To check the influence of the Coefficient of Friction (CoF) on the damage scope on the external surface of the composite, simulations using LS-Dyna software were performed. The main goal of using FEA methods is to replace a continuous system, which is applicable for real constructions, by a discrete system to allow for calculations [4]. At the first stage, the impactor was considered as a sharp edged wedge which is a meshed rigid part. As representative of the impacted reference surface, a newly created laminate was used. The details of the specimen are:

- Overall dimensions: 50 x 15 x 2.5 mm.
- Mechanical properties: Young's Modulus - X direction: 45 GPa, Y direction: 10 GPa , Z direction: 10 GPa,
- Poisson's Ratio XY: 0.3, YZ : 0.4, XZ: 0.3.
- The final laminate was built from 14 plies, which structure follows the order: $[0_2/90_2/45/-45_2/-45_2/45/90_2/0_2]_T$.

A series of simulations were performed, with varying impact angles (30°, 60°) and an impact velocity equal to 70 m/s. The impact velocity corresponds to the real condition of moving railway vehicles during normal operational service. The specimen was fixed on the whole area of the bottom surface, to ensure that no global elastic deformation occurs. In fact, the analysis is focused on local damages which is the reason why this simplification was implemented. Analyses were performed with different Coefficient of Friction values, which varied from 0.1 up to 0.9, by every 0.1. Values close to 0.9 means contact with a sticky rubberized coating, while 0.1 imitates a smooth surface. Both types of external surface can theoretically exist on a cover – a polished topcoat, or additionally, a painted layer to protect the composite from the external environment. For a pair of materials which are used to make the real considered cover and the impactor, CoF value is in the range of 0.35-0.55, which depends on surface condition.

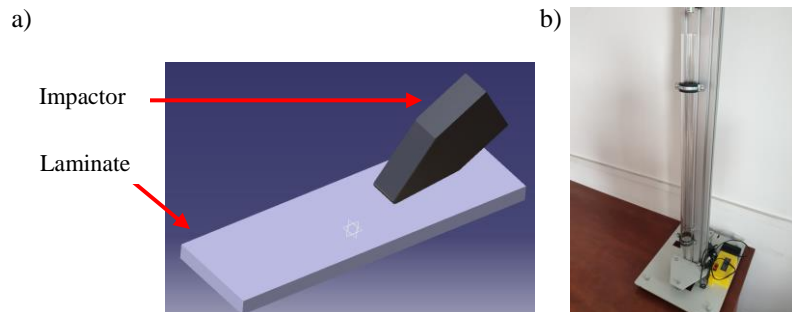a)   b)

Figure 2. a) Simplified model representing the composite specimen and impactor.
b) Apparatus for determining the value of Coefficient of Restitution

The results of performed analysis are presented to show the dependency of the composite damage range on the value of the CoF and the angle of impact.

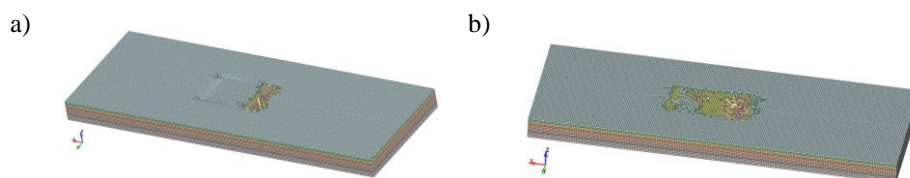a)   b)

Figure 3. Differences in area of damage, impact angle 30 deg,
Coefficient of Friction: a) CoR = 0, b) CoR = 0.5 [5]

As seen in Figure 3, by increasing the CoF value, the area of damage increases. Furthermore, it was observed that with an increasing impact angle, the influence of the CoF on the damage scope reduces, because instead of a scratch, a puncture occurs.

2.2. *Influence of material elasticity*

A cover which protects the underframe of modern railway vehicles may have large overall dimensions, therefore, the rigidity of the cover in relation to the impact strength is not without significance. Because of that, studies on the relationship between the stiffness of the material and its impact resistance, were performed. For this purpose, relevant simulations of the impact for two different variants of the composite material were done. Both structures were sandwich ones, with the same cross-sectional order. The only differences were the coefficients for the foam between the external laminates. The elastic core has a density equal to 330 kg/m^3, and Young modulus E = 122 MPa, while those of the rigid core are 630 kg/m^3 and E = 286 MPa, respectively. [6]

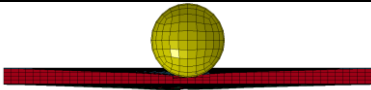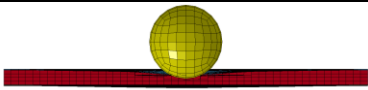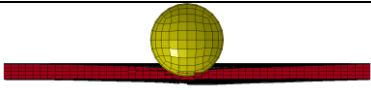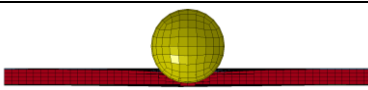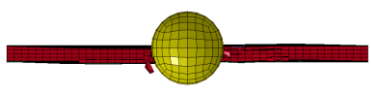| Time [ms]	Elastic foam inside	Rigid foam inside
5.65		
8.48		
21.92		

Figure 4. Differences in results of impact
with different rigidities of thesandwich's core at the same time

According to the comparison between the results in these two cases (Figure 4), it was observed that in the variant with the elastic foam, in first impact phase, because of the large deformation of the sandwich material, the top and bottom external layers were damaged, based on the idea that full penetration occurs faster than in the variant with the rigid core. In the rigid composite in the first phase of impact, a smaller deformation was observed, and thanks to that, the bottom external laminate wasn't damaged. In the next phase, when the core layer was fully penetrated, the ball deformed the bottom layer elastically, without penetration. In this case, the area of the damaged core is much larger than in the previous variant because of the elastic deformation of bottom layer. A large area of debonding between the core and external laminate is easily visible

To verify the elasticity properties of the materials, a dedicated apparatus was created according to standard EN ISO 10545-5 (Figure 2b). This allowed the determination of the value of Coefficient of Restitution (CoR) of the composite material. The CoR's value corresponds to the height of rebound of dropping a steel ball from a fixed height onto the test specimen. A value of CoR close to 0 means a perfectly inelastic collision, where the kinetic energy of the ball is converted into heat or deformation of the object. On the other hand, a value of CoR close to 1 means that the collision is perfectly elastic where no kinetic energy is dissipated. In the real world, the values of CoR are between $0 < e < 1$, depending on the type of material.

2.3. *Fire & Smoke requirements*

As covers designed for being use on trains need to meet the Fire &Smoke requirements, analysis based on European standards was performed. In the first step, to determine the appropriate level of fire protection requirements, the hazard level needs to be specified for the designed train. It must be determined based on a product of the relation between the running time for vehicles in the event of fire (operational category), and the type of the vehicle, for example, a double decked vehicle or a sleeping vehicle (design category). If the vehicle category is correctly defined, the hazard level can be designated. For a considered vehicle, determined as an Electric Multiple Unit, the operational category equals OC2 –which means the running time in the event of a fire shall be 4

minutes, a value which depends on the time needed to stop the movement and start the evacuation process. [7] The design category was specified as N – standard vehicles, according to Table 1, so this means a HL2 level of Material Safety requirement [3]
The designed parts reaction to fire depends on their intrinsic nature and also[2]:

- on the location of the materials within the design,
- on the shape and the layout of the materials,
- on the surface exposed and the relative mass.

Based on that, requirement R7 is finally dedicated for the considered external covers, because of the requirement list provided by the standards, which specifies:

- Location: External part – EX3, under the frame of external body shell,
- Specific use: External surfaces of the underframe structure of the body shell (floor) including paint and coating systems (thermal, design, and acoustic coating) and the protective floor panelling.

As a result, requirement R7, which needs to be met by the underframe's covering must pass the following standards:

- T02 based on ISO 5658-2 – Lateral flame spread,
- T03.01 based on ISO 5660-1 – Reaction to fire tests,
- T10.04 based on EN ISO 5659-2 – Plastics – Smoke generation,
- T11.01 based on EN45545-2 Annex C – Gas analysis in the smoke chamber.

For the above listed standards, more detailed requirements are described in the particular standards themselves. If a new composite material for the cover is to be created, then the tests presented above need to be performed and the relevant certificates should be sent to customer.

2.4. *Acoustic requirements and properties*

Noise requirements in the railway industry are determined by the Commission Decision, "*concerning the technical specification for interoperability relating to the subsystem "rolling stock – noise" of the trans-European conventional rail system*" (2006/66/EC). Based on that, in relation to noise inside the vehicle, the interior noise level of the passenger vehicles is not considered to be a basic parameter, but the noise level in the driver's cab is an issue. [7] Noise levels need to be kept at the lowest possible level by limiting the noise generated at source, as well as by additional insulation and sound absorbers.

The main sources of the noise and vibrations which come from the rail vehicle may be classified as: rolling noise, curve squeal, aerodynamic noise, ground noise, and bridge noise. [8, 9] One of the methods of rolling noise reduction is the use of shielding, for example, wheel mounted, bogie mounted, or vehicle mounted covers. Creating underframe protection covers as noise absorbing, enables the requirements to be met, and additional shields may be not required.

Noise absorption and insulation depends on the frequency, and the loss is higher for higher frequencies. In the case of considering a single-layer construction, such as a steel cover, transmission occurs according to the mass law, the more massive the structure is,

the smaller the amount of sound passing through. For lightweight structures, the use of a filler in the form of an absorbent material results in better sound insulation. This points out the advantage of polymer composite sandwiches in comparison with steel metal covers.

3. Conclusions

The resistance of the cover to impacts by sharp stone edges may be investigated by means of LS-Dyna software. For the investigations, a steel bullet shape, representing the sharp edged and irregular stones, may be used as the impacting element. Simulations shall be done with different specimen angles of inclination, where all the angles should be lower than 45°. It has been assumed that chaotically moving stones before impact of train's underframe, mainly have a vertical velocity, with a low horizontal velocity value in relation to the ground. In this case, the component of horizontal speed during an impact is derived from the speed of the moving train. Since the train speed is much higher than the vertical speed of the stones, the resultant impact force is directed at an acute angle of a rage 0-45° relative to the surface of the underframe, and the value of the impact speed is close to the value of the speed of the moving train. In the case of the underframe cover, where the train speed reaches a maximum 70 m/s, the considered estimated impact energy value for the stones should not exceed 320 J. This value is calculated as kinetic energy taking into account the mentioned speed of the train and the mass of the impactor - 130g. As the impactor shape and its weight during the simulations are constant, the energy may be adjusted by variable velocity – lower operation speed, means lower impact energy.

By using LS Dyna analysis, it is possible to define the required stiffness and strength for each layer of material. As we considered a composite material, the layers are represented by plies and the stiffness value by the plies and foam between the external laminates. The proposed order of the directional composite layers in the external laminate is presented in Figure 5. The number of plies, their direction, and the density of the foam are the points of investigation. For external plies which are mostly exposed to impacts, it is recommended to use unidirectional plies with the direction related to vehicle movement axis. This facilitates a decrease in the damaged area once it occurs.
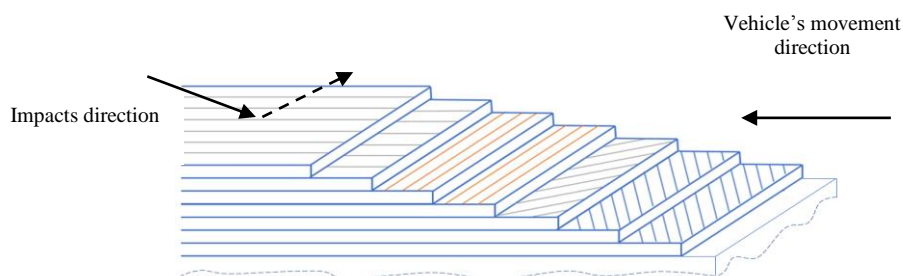

Figure 5. Proposal of external plies order

After the simulations, a real specimen should be created and then validation tests should be carried out to check and confirm the accuracy of the simulations. For this purpose,

a test-bench dedicated to impact research should be used. An example of the work principles is presented in Figure 6.
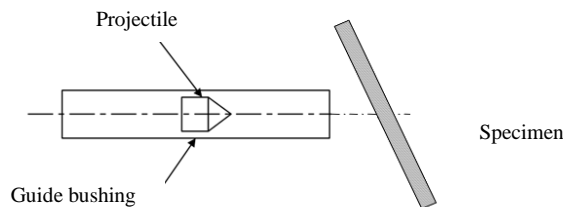

Figure 6. Scheme of impacting machine

After the real test, results, such as penetration depth, will be compared to validate the correctness of the assumptions made during the numerical simualtions.

Acknowledgment

References

1. Standard NF F07-101:2002, *Railway applications – Shock test by throwing up ballast simulation*, 2002.
2. Standard EN 45545-1:2013, *Railway applications – Fire protection on railway vehicles*, General, 2013.
3. Standard EN 45545-2:2013+A1:2015, *Railway applications – Fire protection on railway vehicles. Requirements for fire behavior of materials and components*, 2013.
4. R. Panowicz, D. Kołodziejczyk, K. Sybilski, T. Niezgoda, *Analysis of the process of punching a plate through by a small cylindrical element* (in Polish), Problemy Mechatroniki: uzbrojenie, lotnictwo, inżynieria bezpieczeństwa, **5**(2) (2014) 77 – 90.
5. M. Juzuń, M. Pawlak, *Influence of impact angle and coefficient of friction on high velocity polymer composite damage*, Conference materials, MERGE, Chemnitz, 2019.
6. Livermore Software Technology Corporation (LSTC), *Keyword User's Manual LS-DYNA*, volume I, version 971, May 2007.
7. A. Kaźmierczak, J. Piergies, *Review of selected security requirements for fire protection while assessing the electric multiple unit FLIRT 3 series ED160* (in Polish), Prace Instytutu Kolejnictwa, **150** (2016) 38 – 44.
8. B. Tatic, N. Bogojevic, Z. Soskic, Z. Petrovic, *Railway vehicles as the source of the noise in the urban areas*, Heavy Machinery – HM 2001, 77 – 80.
9. R. Watson, M. Sohail, *Reducing railway noise level - the impact of forthcoming European legislation*, Department of Civil and Building Engineering Loughborough University, Loughborough, UK, 2008.

Three-Dimensional Mathematical Model of Bio-Mechanical System: Human- Mechanized Hand Tool in Accordance to ISO 10068 Standard on the Example of Impact Drill

Wojciech RUKAT

Poznan University of Technology, Faculty of Mechanical Engineering and Management, Piotrowo 3 St, 60-965 Poznan, wojciech.rukat@put.poznan.pl

Abstract

This paper presents the development of a mathematical model of a bio-mechanical system: human – power tool, on the example of an impact drill. The physical model of the operator's upper limb with 5 degrees of freedom, in accordance with ISO 10068 standard was used. The paper presents the results of theoretical analysis regarding elementary and net displacements for individual directions. Moreover mathematical relationships describing them were determined. The result of the synthesis of these relations and the adopted (in accordance with the standard) physical model of the upper limb is the general matrix form of differential equations of motion of the analysed bio-mechanical system, built using the Lagrange's equations of the second kind.

Keywords: local vibration, mathematical model, impact drill, ISO 10068, Lagrange'a equation second kind

1. Introduction

Modelling, simulations and numerical experiments have become one of the most common tools used in the engineering practice. They cover a wide range of issues, including static calculations of elements and structures of various types [1-9], heat and/or working medium (liquids) flows [10-16], changes in the intensity of vector fields (electric and electromagnetic) [17-24] as well as vibration and dynamic analyses of constructions [25-34]. Regardless of the type of analysis conducted, energy methods, such as the finite element method (FEM) and less often the boundary element method (BEM), are used to meet the mentioned goals.

Computation of a complex system, e.g. mechanical construction, is generally limited to solving the differential equation of motion - in the case of dynamic analysis, or the equation of displacement of the system - in the case of static analysis. The generalized equation of motion in the matrix notation is presented below.

$$[M]\big[\ddot{q}_{(t)}\big] + [C]\big[\dot{q}_{(t)}\big] + [K]\big[q_{(t)}\big] = \big[F_{(t)}\big] \tag{1}$$

where: $[M]$, $[C]$, $[K]$ are matrices of inertia, damping and elasticity,
$[F_{(t)}]$ is a vector of forces,
$[q_{(t)}]$, $[\dot{q}_{(t)}]$, $[\ddot{q}_{(t)}]$ are vectors of displacement, velocity and acceleration.

The issues of vibration impact on the human body, including the methodology of performing measurements of local vibrations, are discussed in EN ISO 5349–1 [35] and EN ISO 5349–2 [36] standards. The issue of practical way of measuring vibration of specific body parts (elbow, shoulder, etc.) has been discussed many times, among others

in the works of Bąk and Cukierman-Rakoczy as well as Mrukwa, Świder and Staniek [37, 38]. Doubts regarding unambiguousness of the results obtained (vibrations of soft and hard tissues) and limitations of ethical nature (permanent fixation of the measuring equipment with a human body) have led to the creation of a unified physical model of the upper limb. The first attempts have been made in the 1980s. Possible variants of the human body modelling were presented by Książek as well as Nader and Korzeb [39, 40]. The final result of this work is the ISO 10068:1998 standard [41], which has been successfully used so far. The bio-mechanical system is the result of the synthesis of a mechanical system interpreted as the source of vibrations - e.g. a power tool with the operator's body. In this work, author has analysed and mathematically described vibrations of the bio-mechanical system for three directions of the Cartesian coordinate system, with an assumption that the device (the source of vibrations) can move in all six degrees of freedom.

The mathematical model allowed the author to analyse vibrations of individual human body parts, structural energy flow [42]. This is important when determining the permissible time of exposure to harmful factors that undoubtedly occur during the operation of a device of this type [44-46] and the implementation of occupational safety and health policy.

The aim of the work was to build a mathematical model of the bio-mechanical system: operator – power tool, basing on ISO 10068, using equivalent model of upper limb with 5-dof (degrees of freedom) , while assuming that movement of the source of vibrations in all six degrees of freedom is possible. The same physical model was used for each upper limbs. The structure of the physical model is the same for each of the direction of the coordinate system.

2. Research methodology

The basis for the carried out analysis is the 5-dof equivalent model of the upper limb, which is shown in the Figure 1. The figure presents a combined system of mass elements parallel connected in series and in parallel that represent fragments of the upper limb. Mass elements are connected with each other by both elastic and damping elements. The model also highlights the reference directions of individual coordinate axes in relation to the hand – tool handle system. The structure of the upper limb model is the same for both limbs and in all directions of the coordinate system.

The analysed device is Hitachi DH 22 PH rotary hammer, with a power of 620 W. The maximum spindle speed of this device (without load) equals 1400 rpm. In the impact drilling mode, the mechanism generates 5600 impacts per minute, each with an energy of 1.7 J. Visual inspection and analysis of the device's kinematic and assembly diagrams allow to state that the device's centre of gravity is shifted relative to the plane of the device's body. It also does not coincide with any of handles or the spindle axis. The analysed device was presented on the figure 1.

In the presented model the device's handles are the sources of vibrations. Previous research carried out by the author showed that the device's handles vibrate in all 3 directions. The vibrations have different values for each direction, which makes it possible to suspect that the device moves in all six degrees of freedom during operation [45, 46].

Figure 1. Analysed impact drill - Hitachi DH 22 PH [own photo]
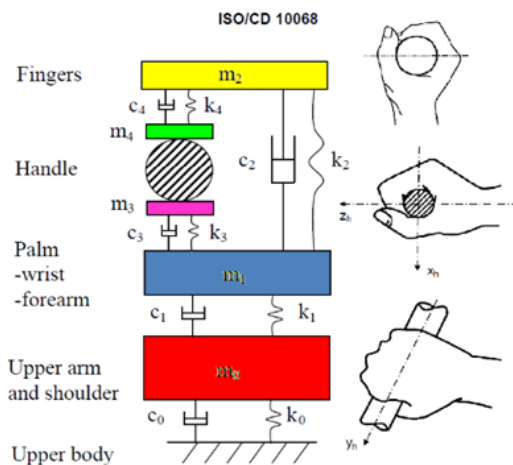
where:
m_0, m_1, m_2, m_3, m_4 - equivalent mass coefficients;
k_0, k_1, k_2, k_3, k_4 - equivalent d stiffness coefficients;
c_0, c_1, c_2, c_3, c_4 - equivalent damping coefficients

Figure 2. 5-dof equivalent model of upper limb [41]

The result of the synthesis of the considered device and the equivalent model of the upper limbs in the base direction (Z axis of the device – spindle's axis) is shown in Figure 3. Furthermore, Figure 4 shows the displacement field corresponding to the equivalent physical model of the entire bio-mechanical system (Figure 3). Figure 4 shows the linear displacement caused by one vector component of the eigenvector of the system and the angular displacement which generates the corresponding linear displacement of the device's handle. The geometric dimensions describing distances between reference points (reduction point) associated with the device handles and the centre of mass are also shown in the figure.

Figure 5 (accordingly to Figure 3) presents the equivalent model of the bio-mechanical system in the Y direction (horizontal, transverse to the spindle axis). Figure 6 shows the displacement field of the device handle on the XZ plane. The equivalent model of the system in the Y axis (vertical direction) and the associated with it displacement field are shown in Figures 7 and 8.
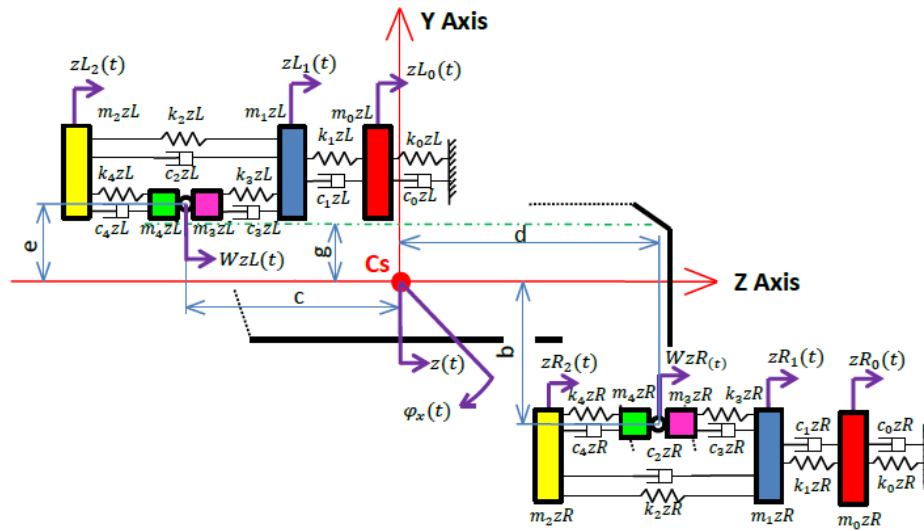
Figure 3. Equivalent model for Z direction

In the figure following markings have been adopted:

m_0zL, m_1zL, m_2zL, m_3zL, m_4zL – equivalent mass coefficients of the left hand in Z direction,
m_0zR, m_1zR, m_2zR, m_3zR, m_4zR – equivalent mass coefficients of the right hand in Z direction,
k_0zL, k_1zL, k_2zL, k_3zL, k_4zL – equivalent stiffness coefficients of the left hand in Z direction,
k_0zR, k_1zR, k_2zR, k_3zR, k_4zR – equivalent stiffness coefficients of the right hand in Z direction,
c_0zL, c_1zL, c_2zL, c_3zL, c_4zL – equivalent dumping coefficients of the left hand in Z direction,
c_0zR, c_1zR, c_2zR, c_3zR, c_4zR – equivalent dumping coefficients of the right hand in Z direction,
$z(t)$ – linear displacement of centre of the mass in Z direction,
$\varphi_x(t)$ – angular displacement of the model around the X axis,
$WzL(t)$ – net displacement of the device's left handle in Z direction,
$WzR(t)$ – net displacement of the device's right handle in Z direction,
b c, d ,e, g – dimensions describing position (distance) between device's handles, spindle and the centre of the mass of the device.
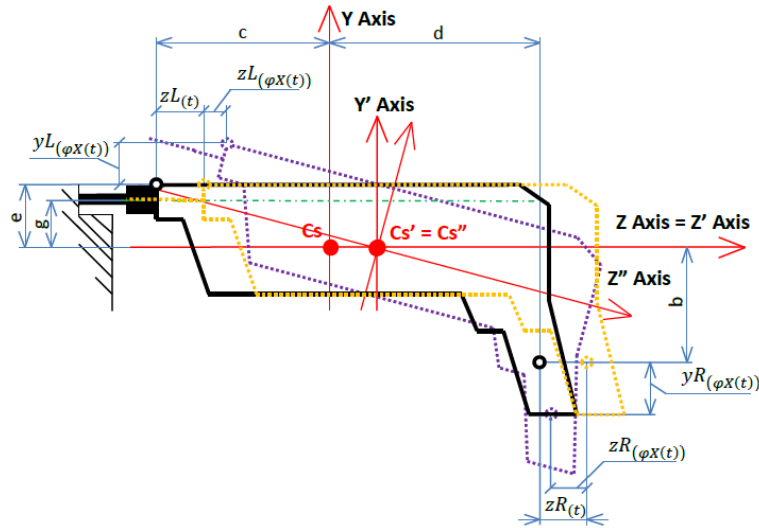
Figure 4. Displacement graph for Z direction

In the figure following markings have been adopted:
b c, d ,e, g – dimensions describing position (distance) between device's handles, spindle
 and the centre of the mass of the device,
$zL(t)$ – displacement of the device's left handle in Z direction caused by linear
 displacement $z(t)$,
$zL_{(\varphi x(t))}$ – displacement of the device's left handle in Z direction caused by angular
 displacement $\varphi_x(t)$,
$yL_{(\varphi x(t))}$ – displacement of the device's left handle in Y direction caused by angular
 displacement $\varphi_x(t)$,
$zR(t)$ – displacement of the device's right handle in Z direction caused by linear
displacement $z(t)$,
$zR_{(\varphi x(t))}$ – displacement of the device's right handle in Z direction caused by angular
 displacement $\varphi_x(t)$,
$yR_{(\varphi x(t))}$ – displacement of the device's right handle in Y direction caused by linear
 displacement $z(t)$.

 Designation of parameters in the four following figures was done in accordance to
designation of parameters in Figures 3 and 4.
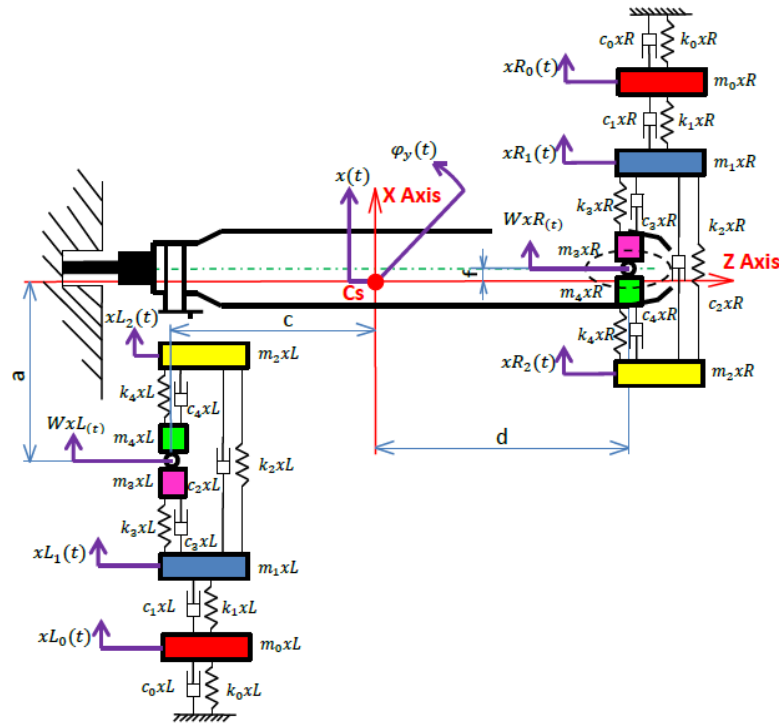
Figure 5. Equivalent model for X direction
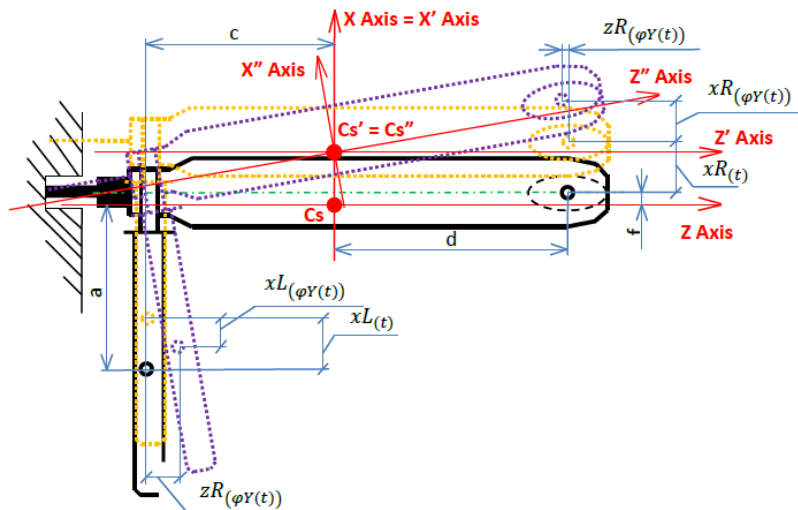
Figure 6. Displacement graph for X direction
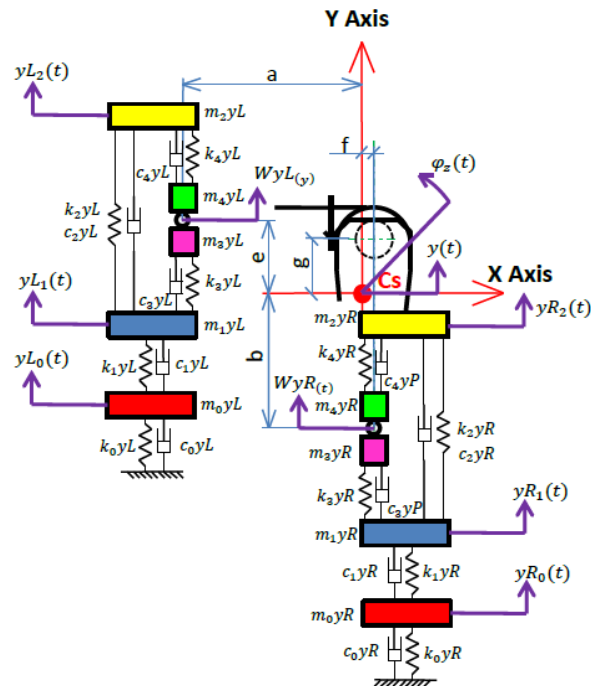
Figure 7. Equivalent model for Y direction
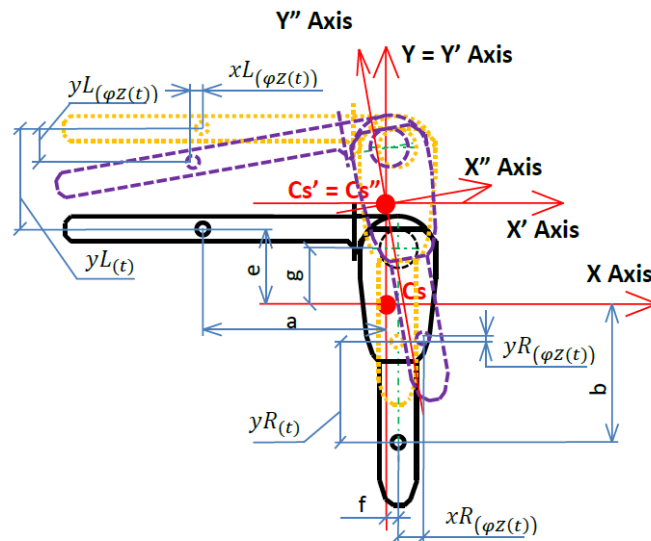
Figure 8. Displacement graph for Y direction

In order to solve the simulation model, it is necessary to determine the value of the force vector – components of the eigenvector and the eigenmoment. The determination of these values requires carrying out kinematic analyses of the device's drive. To do this, one have to define positions of all bearing nodes in relation to the device's centre of the mass. Furthermore, values of technological forces from the tool (friction strength, resistance torque, etc.) should be determined. Then basing on the knowledge of the drive structure and dimensions of its components values of reaction forces (bearings) are calculated. An assembly drawing of the analysed device with highlighted movable parts is shown in Figure 9.
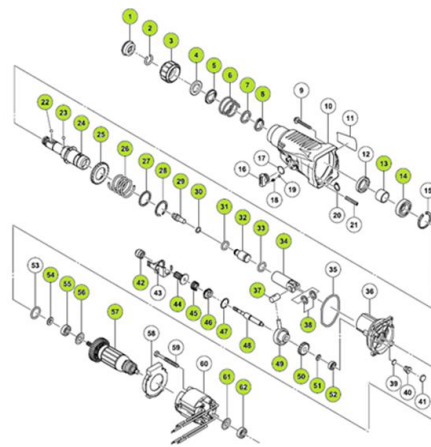
Figure 9. Assembly drawing Hitachi DH 22 PH [47]

The kinematic scheme of the driving mechanism was created based on the assembly drawing. It is presented in the following figure.
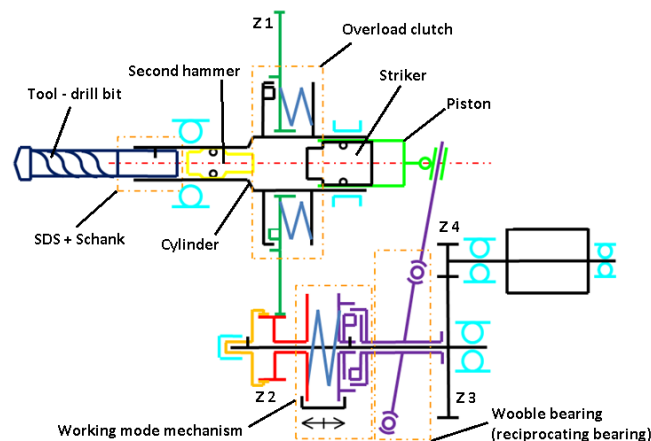
Figure 10. Kinematic scheme of the driving mechanism

The list of movable parts together with the kinematic scheme allows us to analytically determine the value of the mass moment of inertia of the driving mechanism reduced to the spindle axis - $I_Z^{\text{INT. MECH.}}$. It is described by the following equation

$$I_Z^{INT.MECH.} = \begin{bmatrix} (I_1 + I_2 + \cdots. + I_7 + I_8 + I_{13} + I_{14} + I_{22} + \cdots. + I_{28}) \\ +(I_{42} + I_{44} + \ldots. + I_{52})\dfrac{Z1}{Z2} + (I_{54} + \ldots. + I_{57} + I_{61} + I_{62})\dfrac{Z1}{Z2}\dfrac{Z3}{Z4} \end{bmatrix}$$

where: I_i – value of individual moment of inertia; $Z1$, $Z2$, $Z3$, $Z4$ – number of teeth of each gear

A force field acting on bearing nodes was also created on the basis of the kinematic scheme. The input parameters for such calculations are: technological forces, ratios of gear stages as well as geometrical dimensions of elements and arrangement of the bearings. According to reverse engineering values and frequencies of reaction forces can be calculated. These forces are transferred through the device's body onto its handles. They form three-dimensional general force system, that according to principals of the vector calculus, reduces to the eigenvector and the eigenmoment of the entire system. The force field is shown in the figure below.
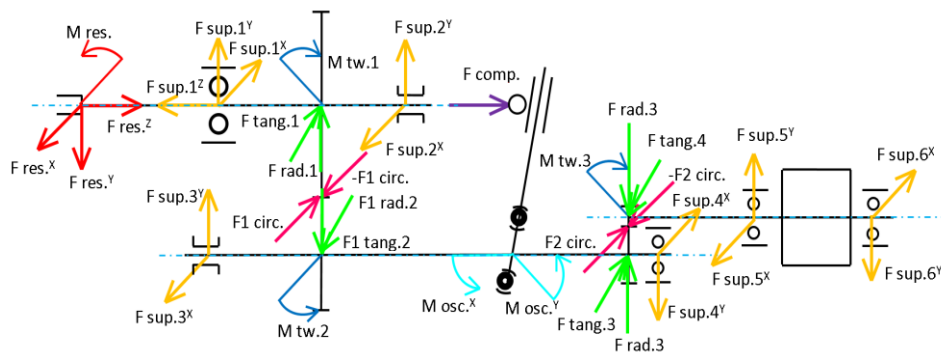
Figure 11. Drive mechanism load diagram

where: $M_{res.}$ – resistance torque; $F_{res.}^{i}$ – resistance force; $F_{sup}j^{i}$ – supporting force; $M_{tw.j}$ – twisting torque; $F_{comp.}$ – compression force; $F_{j\,circ.}$ – circumferential force; $F_{tang.j}$ – tangential force; $F_{rad.j}$ – radial force; $M_{osc.}^{i}$ – oscillating moment; i – X, Y and Z - axis of coordinate system; j – index calculations – number of bearing node and stage of gear of the drive mechanism.

3. Analytical research results

The net displacement of a handle in the considered direction are a geometric sum of the linear displacement of the centre of the mass in this direction and angular displacements resulting from the rotational movement of the device relative to the other two axes of the coordinate system passing through the centre of the mass, for a specific arm measured

between the centre of the mass and the reference point assigned to a the handle. The net vibrations are described for each of directions of the coordinate system, in the case of the rear handle with equations (2), (3) and (4), and for the front handle with equations (5), (6) and (7). In these equations, the net displacements of the handle – reference point, were defined as the geometric sum of the linear displacement of the device's centre of the mass and the displacement of the handle caused by rotational movement relative to axes passing through the centre of the mass. Finally, assuming the linear and angular displacements are finitely small, the components of lower orders, that are associated with to the double product of angular displacements, were omitted and resulted with the following set of equations.

$$W_R Z_{(t)} = z_{(t)} + zR_{(\varphi X(t))} + zR_{(\varphi Y(t))}$$
$$= z_{(t)} + \left(-b \cdot \varphi_{x(t)} - d \cdot \varphi_{x(t)} \cdot \varphi_{x(t)}\right) + \left(-f \cdot \varphi_{y(t)} - d \cdot \varphi_{y(t)} \cdot \varphi_{y(t)}\right)$$
$$\cong z_{(t)} - b \cdot \varphi_{x(t)} + f \cdot \varphi_{y(t)} \tag{2}$$

$$W_R X_{(t)} = x_{(t)} + xR_{(\varphi Y(t))} + xR_{(\varphi Z(t))}$$
$$= x_{(t)} + \left(d \cdot \varphi_{y(t)} + d \cdot \varphi_{y(t)} \cdot \varphi_{y(t)}\right) + \left(-f \cdot \varphi_{y(t)} - d \cdot \varphi_{y(t)} \cdot \varphi_{y(t)}\right)$$
$$\cong x_{(t)} - d \cdot \varphi_{y(t)} + f \cdot \varphi_{y(t)} \tag{3}$$

$$W_R Y_{(t)} = y_{(t)} + yR_{(\varphi X(t))} + yR_{(\varphi Z(t))}$$
$$= y_{(t)} + \left(-d \cdot \varphi_{x(t)} + b \cdot \varphi_{x(t)} \cdot \varphi_{x(t)}\right) + \left(f \cdot \varphi_{z(t)} + b \cdot \varphi_{z(t)} \cdot \varphi_{z(t)}\right)$$
$$\cong y_{(t)} - d \cdot \varphi_{x(t)} + f \cdot \varphi_{z(t)} \tag{4}$$

$$W_L Z_{(t)} = z_{(t)} + zL_{(\varphi X(t))} + zL_{(\varphi Y(t))}$$
$$= z_{(t)} + \left(e \cdot \varphi_{x(t)} + c \cdot \varphi_{x(t)} \cdot \varphi_{x(t)}\right) + \left(a \cdot \varphi_{y(t)} + c \cdot \varphi_{y(t)} \cdot \varphi_{y(t)}\right)$$
$$\cong z_{(t)} + e \cdot \varphi_{x(t)} + a \cdot \varphi_{y(t)} \tag{5}$$

$$W_L X_{(t)} = x_{(t)} + xL_{(\varphi Y(y))} + xL_{(\varphi Z(t))}$$
$$= x_{(t)} + \left(-c \cdot \varphi_{y(t)} + a \cdot \varphi_{y(t)} \cdot \varphi_{y(t)}\right) + \left(-e \cdot \varphi_{z(t)} + a \cdot \varphi_{z(t)} \cdot \varphi_{z(t)}\right)$$
$$\cong x_{(t)} - c \cdot \varphi_{y(t)} - e \cdot \varphi_{z(t)} \tag{6}$$

$$W_L Y_{(t)} = y_{(t)} + yL_{(\varphi X(t))} + yL_{(\varphi Z(t))}$$
$$= y_{(t)} + \left(c \cdot \varphi_{x(t)} - e \cdot \varphi_{x(t)} \cdot \varphi_{x(t)}\right) + \left(-a \cdot \varphi_{z(t)} - e \cdot \varphi_{z(t)} \cdot \varphi_{z(t)}\right)$$
$$\cong y_{(t)} - c \cdot \varphi_{x(t)} - a \cdot \varphi_{z(t)} \tag{7}$$

The mathematical model of the analysed bio-mechanical system was developed using the Lagrange's equations of the second kind. For each of the reference points, directions of vibration and type of motion device (linear and angular), the motion equation was derived individually. The general form of the Lagrange's equation is presented by equation (8).

$$\frac{d}{dt}\left(\frac{\partial E_K}{\partial \dot{q}_J}\right) - \frac{\partial E_K}{\partial q_j} = \frac{\partial L}{\partial q_j} - \frac{\partial V}{\partial q_j} - \frac{\partial \emptyset}{\partial \dot{q}_J} \tag{8}$$

where: E_K – total kinetic energy of the reduction point; L- virtual work of stimulating force at the point of reduction; V-potential elastic forces; Ø –power dissipation function; q- generalized coordinate; j – index calculations; j = 1,2, 3, …, s; s – number of degrees of freedom

Determination of the net accelerations requires knowledge of the values of linear displacements and rotational movements performed in relation to the axes passing through the device's centre of the mass. This leads to formulation and solution (numerically) of the mathematical model - 24 differential motion equations, which representation can be shortened by using the matrix notation and equation (1). Then the general form of the components of this equation is given in the following form:

A) Displacement vector and inertia matrix:

$$q_{(t)} = \begin{bmatrix} iR_{0(t)} \\ iL_{0(t)} \\ iR_{1(t)} \\ iL_{1(t)} \\ iR_{2(t)} \\ iL_{2(t)} \\ i_{(t)} \\ \varphi_{i(t)} \end{bmatrix} \qquad [M] = \begin{bmatrix} m_{0iR} & 0 & 0 & 0 & 0 & 0 & 0 & 0 \\ 0 & m_{0iL} & 0 & 0 & 0 & 0 & 0 & 0 \\ 0 & 0 & m_{1iR} & 0 & 0 & 0 & 0 & 0 \\ 0 & 0 & 0 & m_{1iL} & 0 & 0 & 0 & 0 \\ 0 & 0 & 0 & 0 & m_{2iR} & 0 & 0 & 0 \\ 0 & 0 & 0 & 0 & 0 & m_{2iL} & 0 & 0 \\ 0 & 0 & 0 & 0 & 0 & 0 & M_i & 0 \\ 0 & 0 & 0 & 0 & 0 & 0 & 0 & J_i^{RED.} \end{bmatrix}$$

B) Dumping matrix:

$$[C] = \begin{bmatrix} c_{0iR} + c_{1iR} & 0 & -c_{1iR} & 0 & 0 & 0 & 0 & 0 \\ 0 & c_{0iL} + c_{1iL} & 0 & -c_{1iL} & 0 & 0 & 0 & 0 \\ -c_{1iR} & 0 & c_{1iR} + c_{2iR} + c_{3iR} & 0 & -c_{2iR} & 0 & -c_{3iR} & 0 \\ 0 & -c_{1iL} & 0 & c_{1iL} + c_{2iL} + c_{3iL} & 0 & -c_{2iL} & -c_{3iL} & 0 \\ 0 & 0 & -c_{2iR} & 0 & c_{2iR} + c_{4iR} & 0 & -c_{4iR} & 0 \\ 0 & 0 & 0 & -c_{2iL} & 0 & c_{2iL} + c_{4iR} & -c_{4iL} & 0 \\ 0 & 0 & -c_{3iR} & -c_{3iL} & -c_{4iR} & -c_{4iL} & C_i Z & 0 \\ 0 & 0 & 0 & 0 & 0 & 0 & 0 & C_i \varphi \end{bmatrix}$$

C) Stiffness matrix:

$$[K] = \begin{bmatrix} k_{0iR} + k_{1iR} & 0 & -k_{1iR} & 0 & 0 & 0 & 0 & 0 \\ 0 & k_{0iL} + k_{1iL} & 0 & -k_{1iL} & 0 & 0 & 0 & 0 \\ -k_{1iR} & 0 & k_{1iR} + k_{2iR} + k_{3iR} & 0 & -k_{2iR} & 0 & -k_{3iR} & 0 \\ 0 & -k_{1iL} & 0 & k_{1iL} + k_{2iL} + k_{3iL} & 0 & -k_{2iL} & -k_{3iL} & 0 \\ 0 & 0 & -k_{2iR} & 0 & k_{2iR} + k_{4iR} & 0 & -k_{4iR} & 0 \\ 0 & 0 & 0 & -k_{2iL} & 0 & k_{2iL} + k_{4iR} & -k_{4iL} & 0 \\ 0 & 0 & -k_{3iR} & -k_{3iL} & -k_{4iR} & -k_{4iL} & K_i Z & 0 \\ 0 & 0 & 0 & 0 & 0 & 0 & 0 & K_i \varphi \end{bmatrix}$$

where: i = X, Y, Z - direction of the coordinate system.

The displacement vector is the effect of double integration of the acceleration vector of each of reference points. Currently, for this purpose, numerical integration procedures

(ODE 113 and others) implemented in a digital simulation software are used, e.g. Matlab SIMULINK.

In the above matrices in addition to the individual (or in the form of appropriate algebraic expressions) mass, stiffness and damping parameters, whose values were specified in ISO 10068, there are also generalized equivalent coefficients of mass, stiffness and damping. In the case when the Z direction is considered, the generalized equivalent parameters are:

A) Generalized equivalent mass coefficient

$$M_Z = M_D + m_{3ZR} + m_{4ZR} + m_{3ZL} + m_{4ZL} \tag{9}$$

where: M_D – the device's mass

B) Generalized equivalent moment of inertia

$$J_Z^{RED.} = \left[\begin{array}{c} J_Z^{INT.\ MECH.} + (m_{3XR} + m_{4XR})b^2 + (m_{3XL} + m_{4XL})e^2 \\ + (m_{3YR} + m_{4YR})f^2 + (m_{3YL} + m_{4YL})a^2 \end{array} \right] \tag{10}$$

where: $I_Z^{INT.MECH.}$ – moment of inertia of the drive mechanism generalized to the spindle axis.

C) Generalized equivalent damping coefficient for translations

$$C_Z Z = c_{3ZR} + c_{4ZR} + c_{3ZL} + c_{4ZL} \tag{11}$$

D) Generalized equivalent damping coefficient for rotations

$$C_Z \varphi = [(c_{3XR} + c_{4XR})b^2 + (c_{3XL} + c_{4XL})e^2 + (c_{3YR} + c_{4YR})f^2 \\ + (c_{3YL} + c_{4YL})a^2] \tag{12}$$

E) Generalized equivalent stiffness coefficient for translations

$$K_Z Z = k_{3ZR} + k_{4ZR} + k_{3ZL} + k_{4ZL} \tag{13}$$

F) Generalized equivalent stiffness coefficient for rotations

$$K_Z \varphi = [(k_{3XR} + k_{4XR})b^2 + (k_{3XL} + k_{4XL})e^2 + (k_{3YR} + k_{4YR})f^2 \\ + (k_{3YL} + k_{4YL})a^2] \tag{14}$$

For the other two coordinate system axes, in equations describing the values of equivalent dynamic parameters, in addition to the change of the index of a given axis (for coefficients associated with translations), the dimensions are switched for the corresponding to position related to the given axis - in the case of parameters related to rotational motion.

5. Preliminary simulation results

The results of a simplified simulation concerning only translation in the Z axis are presented below. It was assumed that the motion is the result of the simultaneous operation of a sinusoidal pressure force and the impulse force associated with the impact mechanism

Simulation parameters: mass, stiffness and dumping coefficients in the direction of the spindle axis - Z axis were adopted in accordance with ISO 10068. The mass of the device equals 2.1 kg, while the source of vibration was represented in the form of a sinusoidal signal with an amplitude of 90 N and a frequency of 23.3 Hz. Then, the impact mechanism was modelled as impulses with an amplitude of 270 μm, duration of 0.01 s and 1% signal fill time. Zero initial conditions were also assumed. The system began its motion from rest. Due to the symmetry of the system: both in terms of physical structure and parameter values (coefficients), vibrations of individual reference points for both limbs are the same. In addition, handle vibrations are equal to the vibrations of the device's centre of the mass.

The *RMS* values of acceleration, velocity and displacement of the reference points are presented in the table 1.

Table 1. RMS value of dynamic simulation parameter

Point of reduction	Dynamic parameter		
	Acceleration	Velocity	Displacement
	[m/s^2]	[m/s]	[m]
$z(t) = zP(t) = zL(t)$	12.61	0.09426	0.004019
$zP2(t) = zL2(t)$	4.67	0.08931	0.003808
$zP1(t) = zL1(t)$	2.342	0.09609	0.004099
$zP0(t) = zL0(t)$	0.9721	0.04104	0.001747

The simulation results in the form of acceleration, velocity and displacement signals of individual reference points are presented below. Firstly, the results related to reference points associated with the handles of the device were presented, these are followed by the results for points related to the masses m_2, m_1 and m_0.
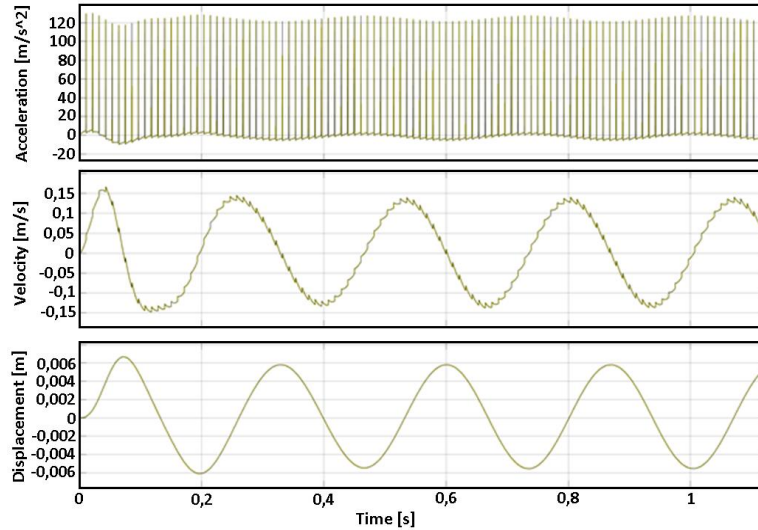
Figure 12. Accelerations, velocity and displacement of the handle – mass m_3 and m_4

As shown in Figure 12, the peak values of vibration acceleration of both the reference points fixed to the device's handles exceed 120 m/s². Accelerations are sinusoidal with a few impulse events. Numerical integration, through which velocities and displacements are calculated, decreases the impact character of the operation. The peak values of velocity reach approx. 0.15 m/s, while peak values of displacement are approx. equal to 7 mm. The transient state associated with the start-up phase lasts approx. 0.5 seconds.
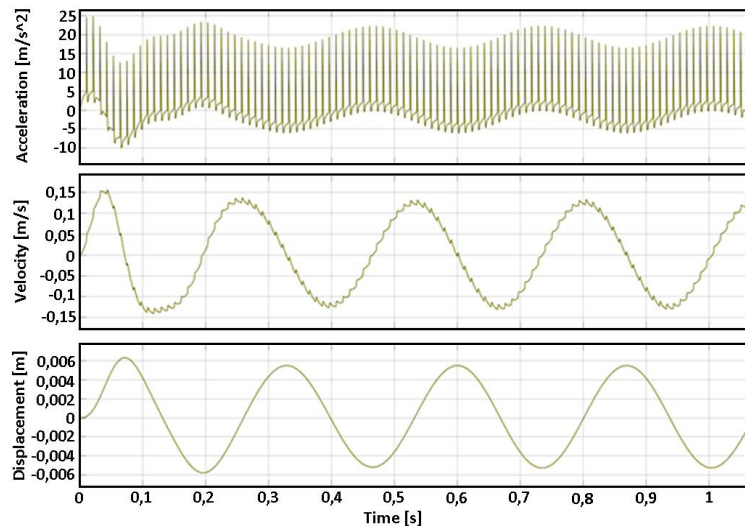
Figure 13. Accelerations, velocity and displacement of the m_2 mass point reduction

Vibration accelerations of the reference point corresponding to the movement of mass m_2 reach a value of about 23 m/s^2, the peak values of vibration velocity, likewise for the handle of the device, are approx. equal to 0.15 m/s. Peak values of displacements are slightly smaller than for the handle and are approx. equal to 6 mm. The nature of the time course of dynamic parameters is similar to one for the before mentioned reference point. For mass m_2, the impulse character of the vibrations also disappears with each subsequent signal integration.
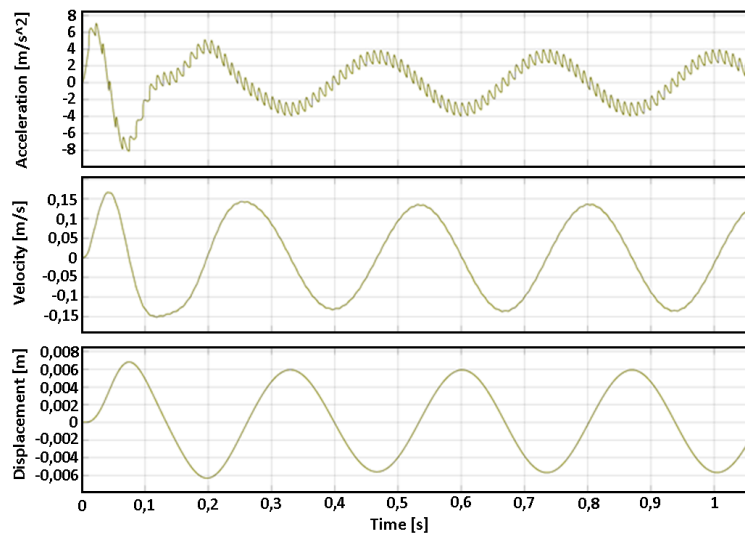
Figure 14. Accelerations, velocity and displacement of the m_1 mass point reduction

As it is shown in Figure 14 for the reference point associated with mass m_1, the peak value of vibration acceleration is about 4 m/s^2. The peak value of vibration velocity, as in previous cases, is approx. equal to 0.15 m/s. Furthermore, the amplitudes of vibration displacements are about 6 mm. In the case of vibration accelerations for mass m_1, no phenomena related to the impact mechanism have been observed. The same it was for previously considered reference points.
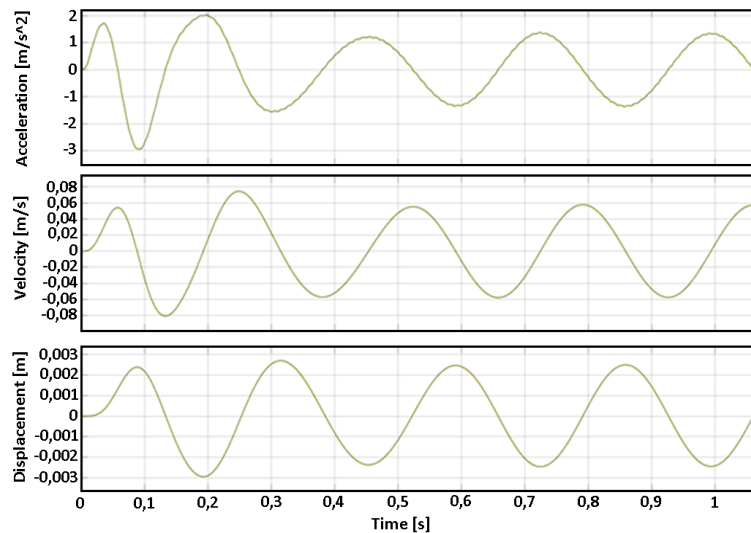
Figure 15 Accelerations, velocity and displacement of the m_0 mass point reduction

For the reference point representing mass movement m_0, the peak values of vibration acceleration shown in the figure do not exceed 1.2 m/s^2. The peak value of vibration velocity equals 0.06 m/s, while the peak vibration displacements are about 2.5 mm. The visible start-up phase, as well as for the previously analysed reference points, lasts about 0.5 seconds.

6. Conclusions

Using the Lagrange's equations of the second kind, it is possible to build a mathematical model describing the vibrations of any mechanical and/or bio-mechanical system.

The ISO 10068 standard provides 3 variants of the upper limb model. For the purposes of the research, the five degrees of freedom (5 dof) equivalent model of upper limb was used.

The development of the mathematical model requires determining the distance between the device's centre of the mass and it's handles as well as calculating moments of inertia in relation to the coordinate system axes.

The structural analysis of the drive mechanism allows us to determine the values of forces acting on individual bearing nodes. Using the theorem on the reduction of any spatial system of forces, one can determine the values of the eigenvector and the eigenmoment of the system in relation to the centre of the mass of the system.

The solution of the mathematical model requires the use of simulation software and a numerical integration apparatus. It is necessary to know the nature and the actual value of the stimulating forces acting on the system.

The determination of values of the mass moments of inertia of the device's drive, regardless from its type and size, requires running structural and kinematic analysis. For this purpose, one can use tools commonly used in engineering practice, e.g. CAx

programs such as Matlab SIMULINK. In the case of the lack of digital documentation of a device, it is necessary to disassemble the device and to map the geometry and kinematic structures of the drive system elements.

The ISO 10068 standard allows an approximate determination of the dynamic parameters of individual parts of the upper limbs when the nature of the source of vibration is known. It is possible without interfering with the operator's body.

On the basis of the results of simulations, it was found that the vibrations emitted by the device exceed both the threshold limit value for an 8-hour working day and for short-term exposure, which has been confirmed in stand tests [45].

Following the path of reference points from the device - the consecutive reference points, the vibration load of individual parts of the operator's upper limbs decreases. At the same time, the phenomena related to the impulse nature of the device's operation disappear.

The simulation model provides the opportunity to analyse transient states by setting elective initial parameter values.

Acknowledgement

References

1. P. Paczos, R. Wichniarek, K. Magnucki, *Three–point bending of sandwich beam with special structure of the core*, Composite Structures, **201** (2018) 676 – 682.
2. M. Obst, D. Kurpisz, P. Paczos, *The experimental and analitical investigations of torsion phenomenon of thin–walled cold formed channel beams subjected to four–point bending*, Thinn–Walled Structures, **106** (2016) 179 – 186.
3. P. Paczos, P. Wasilewicz, E. Magnucka–Blandzi, *Experimental and numerical investigations of five–layered trapezoidal beams*, Composite Structures, **145** (2016) 129 – 141.
4. M. Obst, M. Rodak, P. Paczos, *Limit load of cold formed thin–walled nonstandards channel beams*, Journal of Theoretical and Applied Mechanics, **54**(4) (2016) 1369 – 1377.
5. E. Magnucka–Blandzi, P. Paczos, P. Wasilewicz, A. Wypych, *Three–point bending of seven layers beams – theoretical and experimental studies*, Archives of Civil Engineering, **62**(2) (2016) 115 – 133.
6. P. Paczos, *Experimental investigations of C–beams with non–standard flanges*, Journal of Constructional Steel Research, **93** (2014) 77 – 87.
7. F. Harmit , B. Necib, *Analysis of mechanical structures using plate finite element method under different boundary conditions*, Diagnostyka, **19**(2) (2018) 3 – 9.
8. J. Blata, D. Šeděnka, L. Kašiar, P. Volna, *Examining the condition of the ball and the ball track on the heavy machine ZP6600*, Diagnostyka, **18**(3) (2017) 85 – 91.

9.   Y. Basova, K. Nutsubidze, M. Ivanova, S. Slipchenko, A. Kotliar, *Design and numerical simulation of the new design of the gripper for manipulating of the rotational parts*, Diagnostyka, **19**(4) (2018) 11 – 18.

10. A. Wang, J. Wang, *Temperature Distribution and Scuffing of Tapered Roller Bearing*, Chinese Journal of Mechanical Engineering, **27**(6) (2014) 1272 – 1279.

11. K. Yan, N. Wang, Q. Zhai, Y. Zhu, J. Zhang, Q. Niu, *Theoretical and experimental investigation on the thermal characteristics of double–row tapered roller bearings of high speed locomotive*, International Journal of Heat and Mass Transfer, **84** (2015) 1119 – 1130.

12. J. Li, J. Xue, Z. Ma, *Study on the Thermal Distribution Characteristics of High–Speed and Light–Load Rolling Bearing Considering Skidding*, Applied Sciences, **1593**(8) (2018) 1 – 20.

13. H. Nourghassemi, H. Ghassemi, H. Taghva, *Numerical Hydrodynamic Results of the Two Stedded Planing Hull*, American Journal of Mechanical Engineering, **6**(3) (2018) 93 – 97.

14. S. Boulahrouz, Y. Avenas, A. Chehhat, *CFD Simulation of Heat Transfer and Fluid Flow within Metalic Foam in Forced Convection Environment*, Mechanics and Mechanical Engineering, **21**(3) (2017) 611 – 635.

15. S. Bigham, H. Shokouhmand, R. N. Isfahani, S. Yazdani, *Fluid Flow and Heat Transfer Simulation in a Constricted Microchannel: Effects of Rarefaction, Geometry, and Viscous Dissipation*, Numerical Heat Transfer Applications, **59**(3) (2011) 209 – 230.

16. V. Dmytriv, I. Dmytriv, I. Horodetskyy, T. Dmytriv, *Analytical dynamic model of coefficient of friction of air pipeline under pressure*, Diagnostyka, **20**(4) (2019) 89 – 94.

17. J. Jiang, T. He, H. Duan, B. Li, *Electric Field Structure Analysis and Experimentation of Needle–plate Type Electrospinning Machine*, International Journal of Control and Automation, **7**(1) (2014) 369 – 378.

18. L. Chen, W. Lai, J. Wang, G. Jiang, Y. Zhou, Y. Chen, H. Liu, Z. Qin, L. Ke, L. Wang, Y. Shen, *Study on Surface Electric Field Simulation of High Voltage Transmission Line Assembly*, Journal of Power and Energy Engineering, **2** (2014) 554 – 563.

19. R. S. Ahmad, A. B. Shaari, C. T. Han, *Magnetic Field Simulation of Golay Coil*, Journal of Fundamental Science, **4** (2008) 353 – 361.

20. C. Ghnatios, F. Chinesta, A. Barasinski, *Electrical Fields Simulation in Heterogenus Domain Using the Proper Generalized Decomposition*, ECCOMAS Congress 2016, VII European Congress on Computational Methods in Applied Sciences and Engineering; June 2016.

21. C. Zhang Y. Mao, S. Xie, Y. Zhang, *Electric Field Simulation of Surge Capacitors with Typical Defects*, IOP Conference Series: Materials Science and Engineering, **322** (2018) 072040.

22. T. Li, Y. Jiang, L. Zhao, Y. Wang, *Electrical Field Simulation and Analysis of 1200 kV Gas Insulated Test Reactors*, IOP Conference Series: Earth and Environmental Science, **237** (2019) 062048.

23. H. Benguesmia, N. M'izou, A. Boubakeur, *Simulation of the potential and electric field distribution on high voltage insulator using the finite element method*, Diagnostyka, **19**(2) (2018) 41 – 52.

24. H. Benguesmia, B. Bakri, S. Khadar, F. Hamrit, N. M'izou, *Experimental study of pollution and simulation on insulators using COMSOL® under AC voltage*, Diagnostyka, **20**(3) (2019) 1 – 9.

25. B. Mânescu, N. D. Stânescu, *Dynamic Analisys of a Mechanism of an Engine with Variable Compression Ratio*, IOP Conference Series: Materials Science and Engineering, **564** (2019) 012118.

26. Z. Cao, S. Cao, X. Xu, T. Han, H. Guo, *Dynamic Analysis of the Harvester Seat*, IOP Conference Series: Materials Science and Engineering, **452** (2018) 022013.

27. C. Copilusi, N. Dumitru, A. Margine, I. Geonea, *Dynamic Analysis of a Human Ankle Joints Prothesis*, IOP Conference Series: Materials Science and Engineering, **568** (2019) 012077.

28. S. Maraş, M. Yaman, *Dynamic Analysis of Hybrid Laminated Composite Curved Beam*, 3rd International Conference on Advanced Engineering Technologies, September 2019

29. S. Maraş, M. Yaman, M. F. Şansveren, *Dynamic Analysis of Laminated Syntactic Foam Beams*, 3rd International Conference on Advanced Engineering Technologies, September 2019

30. V. M. Chau, H. B. Vo, *Structural Dynamics Analysis of 3-U Cube Sat*, Applied Mechanics and Materials, **894** (2019) 164 – 170.

31. A. Khnaijar, R. Benamar, *A discrete model for nonlinear vibrations of a simply supported cracked beams resting on elastic foundations*, Diagnostyka, **18**(3) (2017) 39 – 46.

32. M. Guebailia, N. Ouelaa, *The dynamic response of a continuous plate for different surface states*, Diagnostyka, **18**(4) (2017) 11 – 17.

33. J. Zachwieja, *Pipeline stress analysis under supporting structure vibrations*, Diagnostyka, **18**(2) (2017) 23 – 30.

34. Y. Kharchenko, Ł. Dragun, *Mathematical modelling of unsteady processes in electromechnical system of ring–ball mill*, Diagnostyka, **18**(1) (2017) 25 – 35.

35. EN ISO 5349–1 Mechanical Vibration – Measurement and Evaluation of Human Exposure to Hand-Transmitted Vibration – Part 1: General Requirements.

36. EN ISO 5349–2 Mechanical Vibration – Measurement and Evaluation of Human Exposure to Hand-Transmitted Vibration – Part 2: Practical Guidance for Measurement at the Workplace.

37. G. Bąk, E. Cukierman–Rakoczy, *Dynamic reaction of a human on vibrations by analysis of a single-dimensional biomechanical model*, Biuletyn Wojskowej Akademii Technicznej, **67** – LXVII (4) (2018) 169 – 181 (in Polish).

38. W. Mrukwa, J. Świder, A. Staniek, *Assessment of vibration measurement possibility at the contact point of hands with the vibration source*, Prace Naukowe Głównego Instytutu Górnictwa – Górnictwo i Środowisko, **1** (2002) 91 – 102.

39. A. M. Książek, *Analysis of existing biodynamic models of the hand-arm system for human vibration isolation - the operator from vibrations emitted by hand tools*, Czasopismo Techniczne 2M/1996, Wydawnictwo Politechniki Krakowskiej, 87 – 114 (in Polish).

40. M. Nader, J. Korzeb, *The Review of Biomechanical Models to Assess the Impact of Vibrations upon Human Organism*, Materials of a 3rd National Symposium "Computer – Aided Systems for Engineering Works in Industry and Transportation", 1999.

41. ISO 10068:1998 – *Mechanical vibration and shock - Free, mechanical impedance of the human hand-arm system at the driving point.*

42. M. W. Dobry, T. Hermann, *Energy method of an evaluation of human mechanical and biomechanical systems*, Modelowanie Inżynierskie, **17**(48) (2013) 28 – 36.

43. A. Antonucci, A. Barr, B. Martin, D. Rempel, *Effect of bit wear on hammer drill handle vibration and productivity*, Journal of Occupational and Environmental Hygiene, **14**(8) (2017) 641 – 649.

44. B. Jakubek, W. Rukat, *Influence of a tool's working diameter on the level of handle vibrations of an impact drill*, Vibroengineering Procedia, **6** (2015) 288 – 291.

45. B. Jakubek, W. Rukat, *Comparison of vibration impact of an impact drill on the human body under different working conditions*, Vibrations in Physical Systems, **27** (2017) 135 – 142.

46. Handling instruction for Hitachi DH 22PH rotary hammer – Code No. C99179291 F; downloaded from the site: https://hikoki-narzedzia.pl/do_pobrania; Access date: 5 II 2020.

Vibration Impact on People Transported by Mining Belt Conveyors

Grzegorz GÓRA

AGH University of Science and Technology, al. Mickiewicza 30
30-059 Krakow, ggora@agh.edu.pl

Marek IWANIEC

AGH University of Science and Technology, al. Mickiewicza 30
30-059 Krakow, iwaniec@agh.edu.pl

Piotr KULINOWSKI

AGH University of Science and Technology, al. Mickiewicza 30
30-059 Krakow, piotr.kulinowski@agh.edu.pl

Konrad GAC

AGH University of Science and Technology, al. Mickiewicza 30
30-059 Krakow, kgac@agh.edu.pl

Abstract

The paper presents the description and results of experimental research whose purpose was to analyze the vibration influence the miner's body during riding on a belt conveyor for transporting coal. The transport of people on mining belt conveyors is a commonly used method to increase mining efficiency and improve a mine's profitability. The paper presents an assessment of safety and comfort parameters used in transporting people, the effect of strong vibrations on the human body and its internal organs, the measuring system used to record the accelerations during the experiment and the measurement results. The recorded data enabled a dynamic analysis of the movement and an assessment of safety and comfort of transported miners on the basis of defined indicators. The data included the accelerations from the moment of getting on the conveyor belt to the moment of going down onto the platform. The tests were carried out for two different belt conveyor speeds, which allowed to assess how conveyor speed affects safety and comfort of people transported on the mining belt conveyor.

Keywords: belt conveyor, accelerations, safety and comfort of transporting people

1. Introduction

Many experiments described in the literature have confirmed that vibrations impact on the nervous system [1-4] and the circulatory system [5]. These vibrations may have effect on the systems' organs malfunction as well as mental and physical disorder. High vibration amplitudes in long periods of time can cause irreversible changes in the human body and even on internal organs. We are then dealing with a vibration disease (so-called Vibration Syndrome) [2, 6]. There are some studies where the human body is considered as a single mass (uniform mass) for frequency vibrations below 2 Hz [8, 9]. In this frequency band they are not harmful to humans and do not pose a significant threat. Impact of vibrations at a frequency range from 3 to 4 Hz induce strong vibrations

on the abdominal organs and at a frequency range from 7 to 8 Hz there is chest resonance. Vibration frequencies of head's organs are around 20 to 30 Hz and eyeballs at around 60 to 90 Hz. Strong vibrations in the narrow frequency range from 2 Hz to 100 Hz may cause adverse (hazardous in extreme situations) consequences for the human body.

Like all mechanical structures, the human body has resonance frequencies where the body exhibits a maximum mechanical response. Human body responses to vibration cannot be explained solely in terms of a single resonance frequency. There are many resonances in the body, and the resonance frequencies vary among people and with posture [10]. Approximate resonance frequency values of human body organs and possible disease symptoms observed during long exposure are presented in Table 1. When people are transported(e.g. by mining belt conveyors), it is beneficial that the vibration energy is evenly distributed in the frequency band from 2 Hz to 20 Hz, in which the resonant frequencies of most human organs are contained. An adverse phenomenon for the transported person is the effect of high amplitude peaks in a narrow band of the frequencies, which can cause resonant vibration of an organ or group of organs. Presented research concentrated on factors impacting miners comfort during transport by belt conveyors for the velocity above 2.5 m/s.

Table 1. Resonant frequencies of human organs [12]

Name of organ	Frequency Hz	Possible disease symptoms observed
Head	4 – 5, 17 – 25	Pains, dizziness, imbalances, larynx pressure, nausea,
Head with neck	20 – 30	forced rotation movement of the head,
Eyeballs	40 – 90	speech impediment, general psychophysical fatigue
Abdominal organs	4.5 – 10	Sensation of internal organs vibration, pain, nausea, feeling of fullness, urinary and bowel urgency,
Stomach	2 – 3	weakness and fatigue, reluctance to performing work
Chest organs	5 – 9	Respiratory distress, dyspnea, tachypnea, sensation of restlessness, pulse acceleration, blood pressure changes, heart beat, speech disorders,
Lungs	4 – 11	
Heart	4 – 6	
Lower torso	4 – 6	Joint and muscle pains, lumbar and cervical spine pain, increased muscle tension, fatigue
Pelvis	5 – 9	
Spine	10 – 12	
Hips	5	Joint and muscle pains, increased muscle tension, numbness and tingling of muscles
Calves	20	
Arm	16 – 30	Joint pains, increased muscle tension, muscle pains, involuntary muscular contractions resulting in additional hand movements
Forearm	4 – 6	
Hand	20 – 30	

2. Indicators for assessment of comfort and safety

The raw data from accelerometer recorded during experiments (the acceleration versus time) are difficult to unequivocal interpret and analyze. Therefore, the data analysis techniques used are, described by indicators and estimators to obtain better results.

The RMS (Root Mean Square) indicator is most often used to estimate the impact of vertical vibrations on the human body. The root-mean-square acceleration versus time gives a measure of the oscillatory content in the acceleration data. For the period of time considered, this quantity gives an indication of the time-averaged energy in the signal [11, 14]. The RMS value of acceleration is defined as (1).

$$a_{RMS} = \left[\frac{1}{T} \int_0^T a^2(t) \mathrm{d}t \right]^{\frac{1}{2}} \tag{1}$$

where: $a(t)$ is the time history of the vertical acceleration recorded as a function of time t and expressed in m/s^2, and T is the duration of the measurement in seconds.

Table 2 presents the relation of the frequency-weighted a_{RMS} acceleration and subjective response scale (degree of comfort) of ISO 2631-1 standard[12] and BS 6841standard [3].

Table 2. The scale of discomfort based on a_{RMS} [3, 5]

Frequency-weighted R.M.S. acceleration in units of m/s^2	Subjective response
Less than 0.315	Not uncomfortable
0.315 – 0.63	A little uncomfortable
0.5 – 1.0	Fairly uncomfortable
0.8 – 1.6	Uncomfortable
1.25 – 2.5	Very uncomfortable
Greater than2.0	Extremely uncomfortable

Simultaneously, the a_{RMS} underestimate the effects of transient shocks (instantaneous sudden amplitude growths), due to which neither of these methods makes it possible to take into account the impact of such shocks on the human body [13]. Therefore, an index referred to as a_{RMQ} (Rot Mean Quad) has been introduced, which was proposed by M. J. Griffin [2], described in BS 6841 [3], and defined as follows (2).

$$a_{RMQ} = \left[\frac{1}{T} \int_0^T a^4(t) \mathrm{d}t \right]^{\frac{1}{4}} \tag{2}$$

The a_{RMQ} is a preferred measurement for exposure to jolts, shocks and intermittent vibration because it is sensitive to peaks in acceleration levels. [13].

3. Methodology and system of measurement

In order to perform acceleration measure and data acquisition, the dedicated mobile measuring device was designed. The measuring recorder was built based on the 32-bit RISC (Reduced Instruction Set Computing) microcontroller with the ARM Cortex-M3 core. The user interface consists of a mini-keyboard and LCD (Liquid Crystal Display).

The recorder allows accelerations measurement from three digital sensors and saves data to an SD card. Saving to a file in text form allows to easily transfer data to any computer. The three-axis MEMS (Micro Electro Mechanical Systems) accelerometers were used to measure acceleration. The use of integrated digital sensors allows to easily and quickly change the settings of measurement parameters such as resolution, bandwidth, sensitivity, and range. Data reading from each sensor was carried out via the I2C (Inter-Integrated Circuit) serial interface. The recorders were placed in miners' backpacks during recording or data acquisition.

Table 3. Parameters of the measuring system

Parameter	Value	Unit
Sampling frequency	512	Hz
Measurement range	16	g
Sensor sensitivity	3.9	mg/LSB
Non-linearity	0.5	%
RMS noise level	1	LSB
Maximum sensor bandwidth	3200	Hz
Accelerometer low pass filter	250	Hz
Power supply (6 x AA batteries)	9	VDC

The accelerations of the body part of miner transported by belt conveyor were recorded during the experimental tests. Data recording has begun just before the moment of getting on the conveyor belt and has finished when the person going down onto the platform. Each of the measuring systems allows the acquisition of acceleration data from three independent channels (sensors).The first two sensors enabled the measurement of vibrations on the miner's legs. They were mounted on shoes, beside the ankles. The third sensor was attached to the belt or placed on the back, at the height of the breastbone. This arrangement of sensors allowed to study the dynamics of miner's movement. Additionally, it allows the detection of dangerous cases such as strong shocks, loss of balance or falling.

4. Experiments

An analysis compares data from three channels (right leg, left leg, belt or back). The recorded data consist of accelerations from three orthogonal axes. Figure 1 presents the accelerations from the moment of getting on the conveyor belt to the moment of going down onto the platform with described stages of the ride.
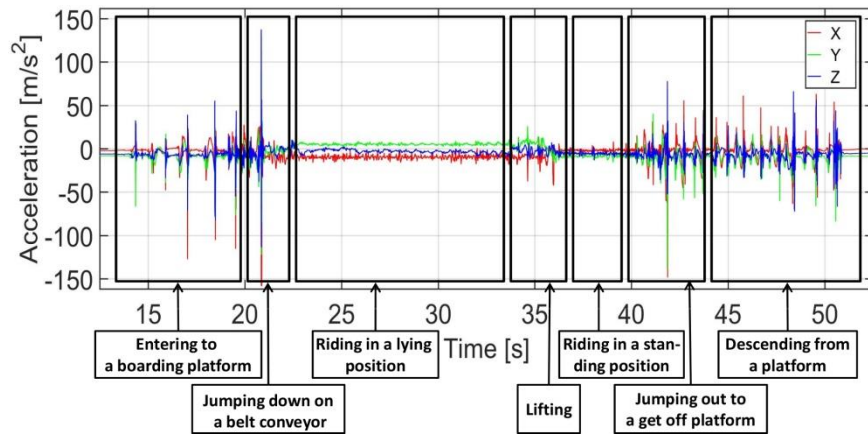
Figure 1. Accelerations recorded during transport with velocity 2.5 m/s

Curves colours are assigned to the respective sensor axes (X - red, Y - green, Z - blue). The axes of the coordinate system were dependent on the orientation of mounting the sensor on the body and current miner's body position. In order to determine the spatial orientation, they should be transformed individually for each case by determining the direction of the constant component (gravitational acceleration).

5. Results

Based on the recorded acceleration data from the miners' rides, an FFT(Fast Fourier Transform) frequency analysis was performed.
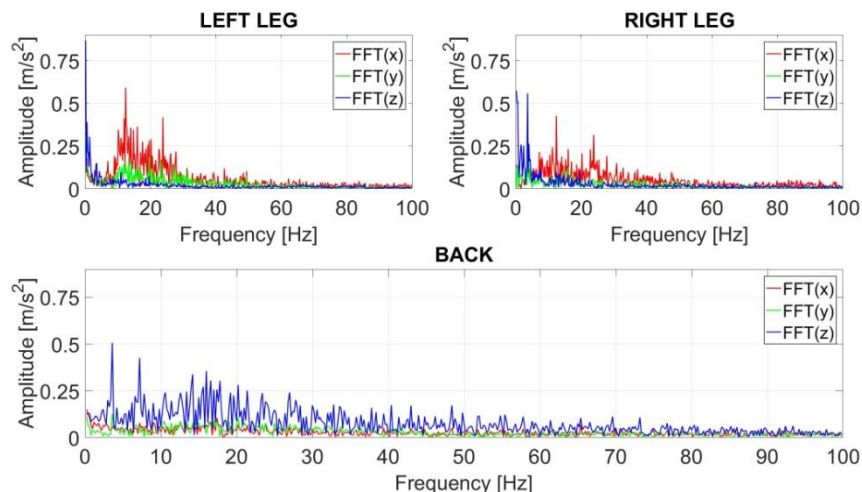
Figure 2. Acceleration spectra of vibration recorded during transport with velocity 2.5 m/s, lying position
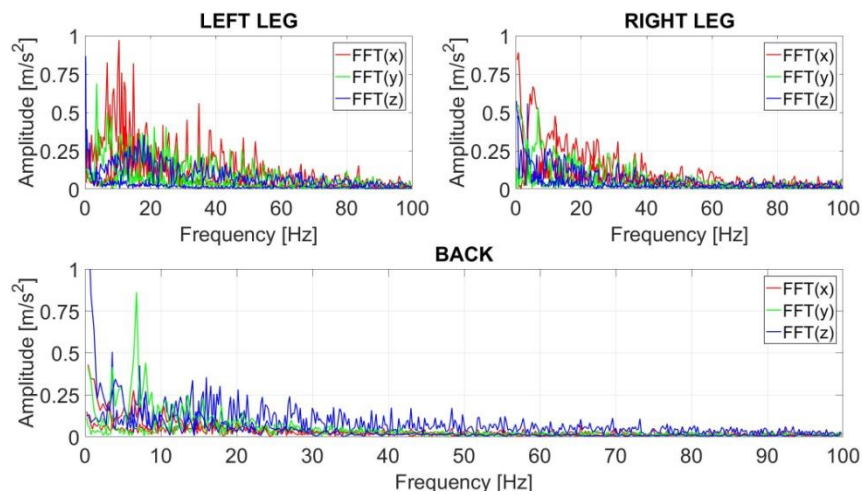
Figure 3. Acceleration spectra of vibration recorded during transport with velocity
2.5 m/s, standing position
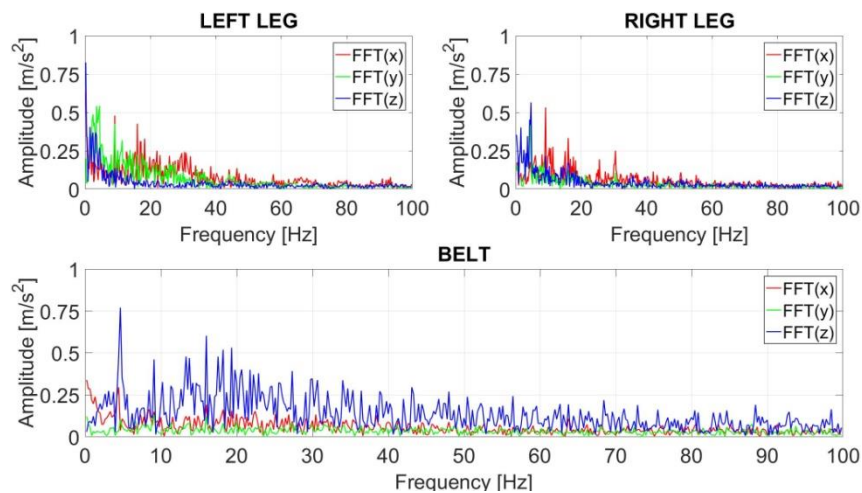
Figure 4. Acceleration spectra of vibration recorded during transport with velocity
3.3 m/s, lying position

The graphs above (Figure 3-4) show a comparison of the accelerations' spectra for transport of people with the speed 2.5 m/s and 3.3 m/s in the lying position and for the speed 2.5 m/s in the lying and standing position. The results of FFT transform shows that a resonant band occurs in the vibrations range around 5 Hz, which corresponds to the human heart, head and chest organs resonant frequency. The body posture is the factor

that impacts the possibility of dangerous vibrations of internal organs during transport more than belt movement velocity.

Table 4. Parametrization results of vibrations registered during transport of people by mining conveyors (bandwidth: 2-250 Hz)

Person	Lying position, *max* (x, y, z)			Standing position, *max* (x, y, z)			Lying position, *max* (x, y, z)			Standing position, *max* (x, y, z)		
	LL	RL	B/B	LL	RL	B/B	LL	RL	B/B	LL	RL	B/B
	a_{RMS} [m/s^2] (transport velocity 2.5 m/s)						a_{RMQ} [m/s^2] (transport velocity 2.5 m/s)					
B1	1.76	2.32	1.33	9.32	9.32	3.25	3.57	5.13	2.33	14.50	20.39	4.10
B2	2.53	1.95	2.89	4.26	1.59	2.45	3.64	2.95	6.22	8.33	2.43	3.49
B3	1.03	1.09	2.56	6.53	8.74	2.90	1.49	1.66	1.78	11.38	14.93	4.35
	a_{RMS} [m/s^2] (transport velocity 3.3 m/s)						a_{RMQ} [m/s^2] (transport velocity 3.3 m/s)					
B1	2.41	2.67	3.37	8.50	14.68	5.87	4.92	4.21	4.31	17.65	35.74	8.53
B2	2.60	2.12	4.67	6.47	6.54	2.51	3.79	3.01	9.53	11.62	14.11	3.46
B3	2.50	2.12	1.84	8.69	4.37	3.51	3.87	3.58	3.33	17.19	8.42	4.65
LL – left leg, RL – right leg, B/B – back/belt,												

6. Conclusions

Based on the results of the research conducted it can be assumed that the acceleration measurement data allow safety and comfort assessment of transported people.

The vibration frequency analysis enables the risk evaluation of harmful influence on human body organs and vitals. An increased speed of belt conveyor has no negative impact on comfort of transported miners according to a_{RMS} and a_{RMQ} indicators (Table 4). Frequency analysis shows that increased energy of vibrations (resulting from the increase of speed of a belt conveyor) has a linear distribution in the research range. The results of FFT transform shows that a resonant band occurs in the vibrations range around 5 Hz, which corresponds to the human heart resonant frequency. Therefore, some medical examinations for miners using belt conveyors for transport should be conducted (with special emphasis on possible heart diseases). The future steps of the research will include experiments with changing the speed of a moving belt by a few percent (increase and decrease of the speed) and carrying out the experiments on another conveyor belt. That may lead to a decrease in the amplitude of a resonant band. The body posture is the factor that impacts the possibility of dangerous vibrations of internal organs during transport the most.

The transport in a standing position may induce strong vibrations on a chest and

abdominal cavity (or abdominal organs). That is the consequence of high bands on the frequency spectrum in the range from 4 to 6 Hz. It is suggested to minimize the time of transport in the standing position. Based on the data provided in table 3 it can be assumed that an increase of velocity of the belt conveyor does not have any major effect on comfort during the transport. A moderate discomfort can be statistically confirmed for all the analyzed cases.

References

1. J. Dziurdź, *Human hazards in the work environment - Vibrations and noise* (in Polish), Warsaw University of Technology 2011.
2. M. J. Griffin, *Handbook of human vibration,* Academic Press, London 1990.
3. BS 6841:1987, *Guide to measurement and evaluation of human exposure to whole-body mechanical vibration and repeated shock,* 1987.
4. J. Iwaniec, M. Iwaniec, *Heart work analysis by means of recurrence-based methods*, Diagnostyka, **18** (2017) 89 – 96.
5. A. Dzhambov, D. Dimitrova, *Heart Disease attributed to occupational noise. Vibration and other co-exposure: self reported population-based survey among Bulgarian workers,* Medycyna Pracy, **67** (2016) 435 – 44.
6. A. Sonza, C. Robinson, *Whole Body Vibration at Different Exposure Frequencies: Infrared Thermography and Physiological Effects*, The Scientific W.J., 2015.
7. K. Krajnak, D. Riley, J. Wu, T. McDowell, D. Welcome, Xs. Xu, R. Dong *Frequen-cy-dependent Effects of Vibration on Physiological Systems: Experiments with Animals and other Human Surrogates*, Industrial Health **50** (2012) 343 – 353.
8. R. Budzik, *The research of vibration of vehicle floor pane* (in Polish)*, Silesian University of Technology - Drgania i hałas, **67** (2010) col. 1832, 23 – 30.
9. D. Więckowski*, An attempt to estimate natural frequencies of parts of the child's body* (in Polish), Wydawnictwo Naukowe, (2013) 159 – 172.
10. J.M. Stellman*, Encyclopaedia of Occupational Health and Safety,* International Labor Office, Geneva, **2** (1998).
11. M. Rogers, K. Hrovat, K. McPerson, M. E. Moskowitz, T. Reckart*, Accelerometer Data Analysis and Presentation Techniques,* Technical Report, NASA-TM-113173, **2** (1997) 2 – 13.
12. ISO 2631-1, *Mechanical vibration and shock. Evaluation of human exposure to whole-body vibration,* Part 1: General requirements*, 1997.
13. D. Więckowski*, Analysis domain of the time vertical vibration on a account comfort child during ride in the car* (in Polish)*, Mechanika – Czasopismo Techniczne, **10** (2017) 73 – 91.
14. W. Sawczuk, *Application of selected frequency characteristics of vibration signal for the evaluation*, Diagnostyka, **16** (2015) 34 – 36.

Identification and Classification of Selected Internal Combustion Engine Inefficiency Based on Vehicle Structure Vibrations

Krzysztof PRAŻNOWSKI, Jarosław MAMALA,
Andrzej BIENIEK, Mariusz GRABA
Opole University of Technology, Mechanical Department,
Mikołajczyka street 5, 45-271 Opole,
k.praznowski@po.edu.pl, j.mamala@po.edu.pl,
a.bieniek@po.edu.pl, m.graba@po.edu.pl

Abstract

The combustion engine generates forced vibrations, caused by periodically acting external forces resulting from the combustion of the fuel-air mixture. Any changes in this process cause an increase in the value of vibration amplitude and a change in the distribution of harmonics dominating in the frequency domain. In order to identify selected malfunctions of the internal combustion engine of the Polaris off-road vehicle tested, its current parameters were correlated with the vibrations transmitted to the vehicle's structural elements. An integrated sensor for measuring acceleration using the direct method, made in MEMS technology, was used for the tests.

The recorded signals of the acceleration components were subjected to analysis in the frequency domain, thus identifying the characteristic harmonic components in the analyzed spectrum. For the classification of incompleteness based on registered signals, a diagnostic inference matrix based on our own algorithm of conduct was used.

Keywords: short-term analysis, Fourier transform, engine diagnostics, diagnostic matrix

1. Introduction

In most internal combustion engines, fuel combustion occurs between the piston, cylinder and head. Then we deal with internal combustion engines in which mechanical work is carried out in a periodically repeatable manner and dependent on the number of strokes and the angular speed of the engine crankshaft [1]. The course of the fuel-air mixture combustion process in this type of engines is very intense at significant variable combustion pressures, which contributes to the formation of large energy pulses affecting the crank-piston system changing the instantaneous crankshaft angular velocity. The analysis of the instantaneous change in the angular velocity of the engine crankshaft was used to detect combustion process irregularities [2]. The phenomenon of disturbed combustion process of the mixture is also visible when applying direct pressure measurement in the combustion chamber. This manifests itself then in the oscillation of the pressure in the combustion chamber [3, 4]. However, the method is limited due to low durability and high cost of implementation.

Another method of diagnosing the correctness of combustion of the fuel-air mixture in the engine is the vibration analysis of the internal combustion engine [5-10]. In internal combustion engines, the detection of this process uses both the measurement of the angular speed of the crankshaft of the engine, by using a speed with higher

resolution correlated with the knock sensor. This combination is due to the large number of factors that affect the knock sensor vibration measurement process. This process may be preceded by signal re-sampling [11] and deeper spectral analysis allowing obtaining a spectrum with a characteristic harmonic component. Acceleration value recorded at the output of the acceleration sensor mounted on the engine body, represent the processed response of the elastic system to forced type: pressure changes as a result of combustion, pulsation of exhaust gases in the exhaust duct, etc. In addition, the measurement of body vibrations and analysis of statistical features is used to assess the impact of various fuels (gasoline, ethanol) for the correct implementation of the combustion process in the engine [4].

In [12] the application of the classification algorithm based on artificial neural networks (ANN), carrier vector machines (SVM) and k Neighbor Neighbor (kNN) classification algorithms are employed to predict if the motor works healthily based on the selected features and, if not what kind of faults is in the engine.

However, during operation of an internal combustion engine, its emergency conditions may occur resulting in introducing the engine into uncontrolled disturbances in its operation. This phenomenon may result, for example, from a malfunctioning fuel injection system. The resulting malfunction of the engine in the form of shutting down the cylinder from work causes a change in the amplitude spectrum of engine body accelerations.
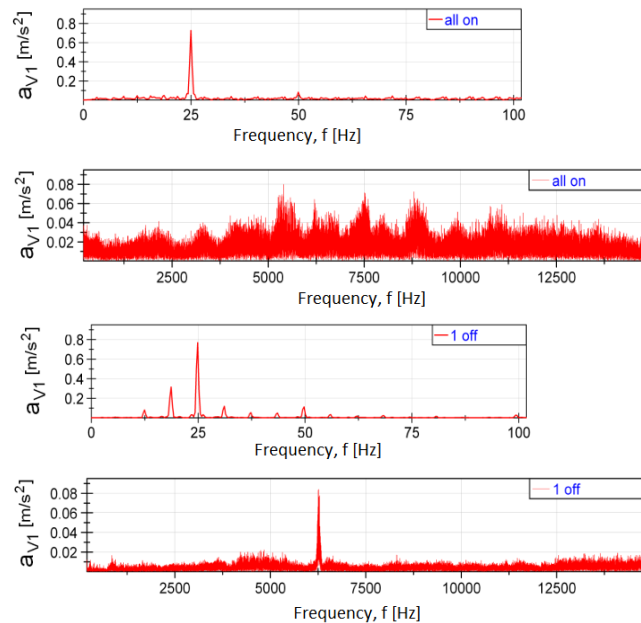

Figure. 1. Frequency spectrum of the vertical vibration acceleration – 1st cyl. [9]

As presented in [9], switching off one of the cylinders reduces the value of the amplitude of the engine vibration acceleration in both directions for all frequencies from

2.5 to 15 kHz except for the frequency of about 6.25 kHz, which is visible in the characteristic increase in amplitude in the spectrum of the tested signal. However, changes in the low frequency range (fundamental frequency and its multiplicity) were found. The harmonic increase occurs when one (several Fig. 1) or several cylinders are turned off.

The resulting vibrations of the engine and other elements of the chassis are transmitted by the engine mounting elements to the vehicle body [10]. The elastically damping properties of these elements are selected so that the occurring vibrations are the least burdensome for the vehicle user and do not cause stress in the body structure. However, these vibrations can be a source of diagnostic information [13, 14] about the occurrence of an internal combustion engine malfunction resulting from an incorrect combustion process. This information constituted the basis for undertaking works related to the identification of a combustion engine malfunction based on vibrations of the vehicle structure. Such a solution can be used in the conditions of actual operation to infer about the technical condition of selected components of the propulsion system [15].

2. Research object

The research involved the use of a Polaris off-road vehicle, which was equipped with an original integrated measuring system consisting of a wireless data transmission system from the on-board CAN BUS network and an acceleration sensor (Fig. 1). The wireless data transmission system uses diagnostic connector signals and allows data to be transferred from the vehicle to the recording computer using a radio transmitter operating in the 433 MHz band, which range is up to 1 km.

The sensor (3DM-GX3-25) was used to measure acceleration by a direct method. It is made in MEMS technology. The sensor is insensitive to the effects of internal noise of conditioning systems due to the use of a set of sensors with pulse PWM output. It has a built-in processor, which thanks to the algorithm of measurement synthesis provides static and dynamic orientation of its measurement axes. Basic parameters of the sensor are given in Table 1.

Table 1. Parameters of the sensor 3DM-GX3-25

Quantity	Value
Attitude heading range	360° about all 3 axes
Accelerometer range	±5g standard
Gyroscope range	±300°/sec standard
Static accuracy	±0.5° pitch, roll, heading typical for static test conditions
Data output rate	up to 1000 Hz
Filtering	sensors sampled at 30 kHz, digitally filtered (user adjustable) and scaled into physical units; coning and sculling integrals computed at 1 kHz
Interface	RS232
Baud rate	115,200 bps to 921,600 bps
Power supply voltage	+3.2 to +16 volts DC

The sensor was mounted on a structural element (frame) of the tested vehicle. This solution is intended to determine the possibility of using the vibrations of the support structure to identify selected given internal combustion engine malfunctions. The elastic damping elements fixing the engine to the frame did not show any operational damage. Directional setting of the sensor axis for recording vibrations caused by the operating internal combustion engine relative to the engine crankshaft: x – longitudinal axis, y – transverse axis, z – vertical axis is shown in Fig. 2.
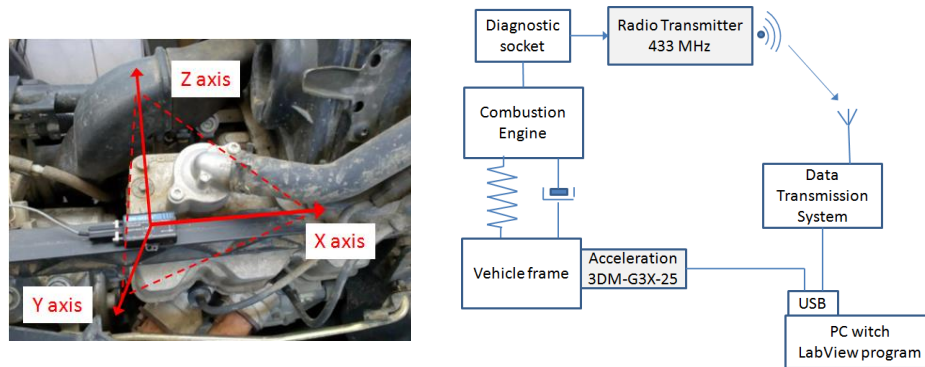

Figure 2. Placement of the 3DM-GX3-25 sensor on the vehicle during tests and block diagram of the measuring system

3. Signal analysis

The own application developed in MATLAB was used to analyze the recorded acceleration sensor signal and engine operating parameters. Due to the diversity of signal sampling (866 Hz for acceleration sensor and 132 Hz for engine running signal), the signals were synchronized.

The recorded signal from the acceleration sensor was analyzed using the Short-Term Fourier Transform (STFT) method. In the first phase, the STFT method consists in dividing the input signal into smaller segments, in which it can be treated as quasi-stationary, and then processing it based on the FFT algorithm of individual data segments. Short-term Fourier transform is described by equation 1, while the input signal is equated by equation 2.

$$STFT[x_w(t,\tau)] = \int_{-\infty}^{\infty} w(t,\tau)x(t)e^{-j2\pi ft}dt \tag{1}$$

$$x_w(t,\tau) = w(t,\tau)x(t) \tag{2}$$

In this way, a frequency and spectral map of the analyzed vehicle body vibration signal was obtained as a result of forcing the operating internal combustion engine (Fig. 3, 4, 5).

The obtained waveforms showed the occurrence of clear amplitudes in the range of the fundamental frequency f_1, as well as its subsequent harmonic order ($f_{0.5}, f_{1.5}, f_2, f_{2.5}$).
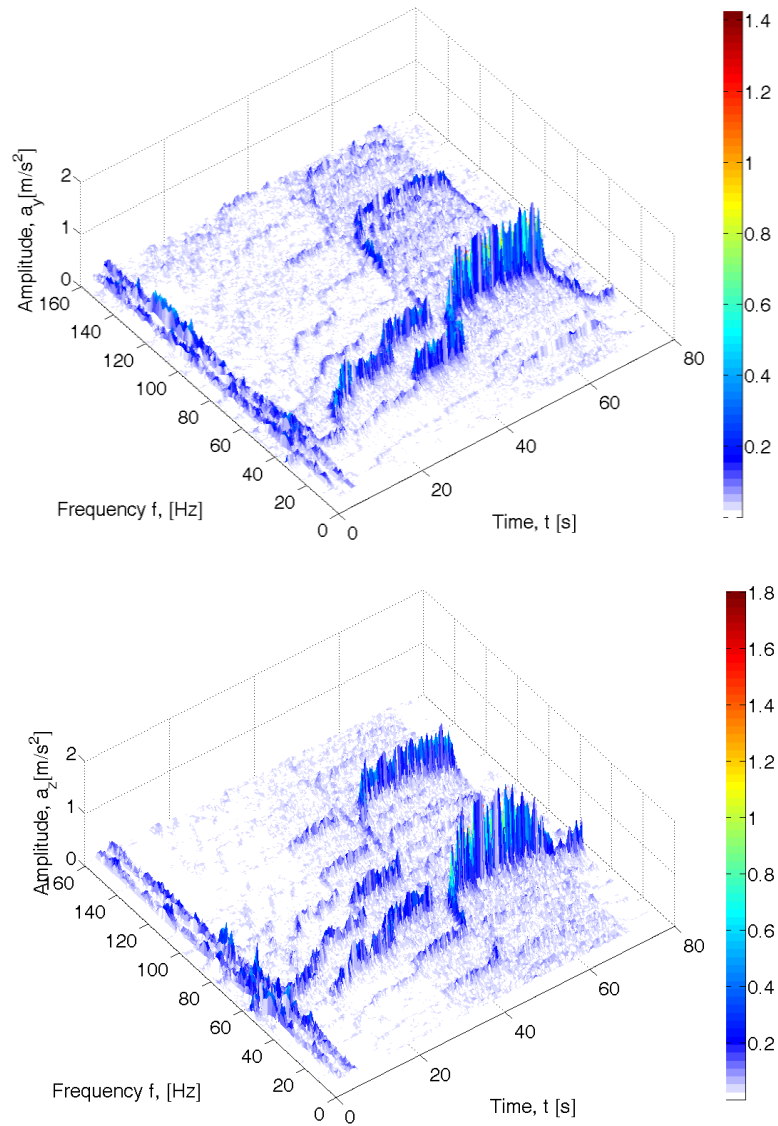
Figure 3. STFT spectrum for an faultless IC engine
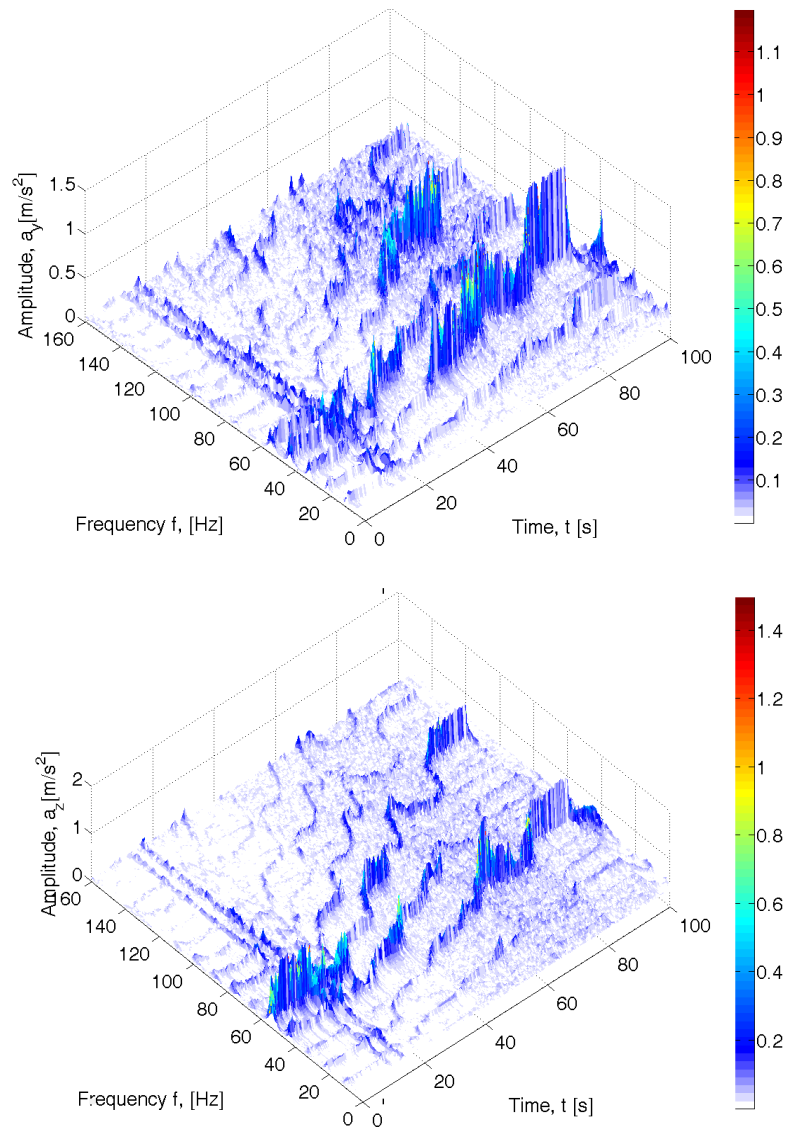
Figure 4. STFT spectrum for a malfunctioning IC
engine - time gap in fuel injection
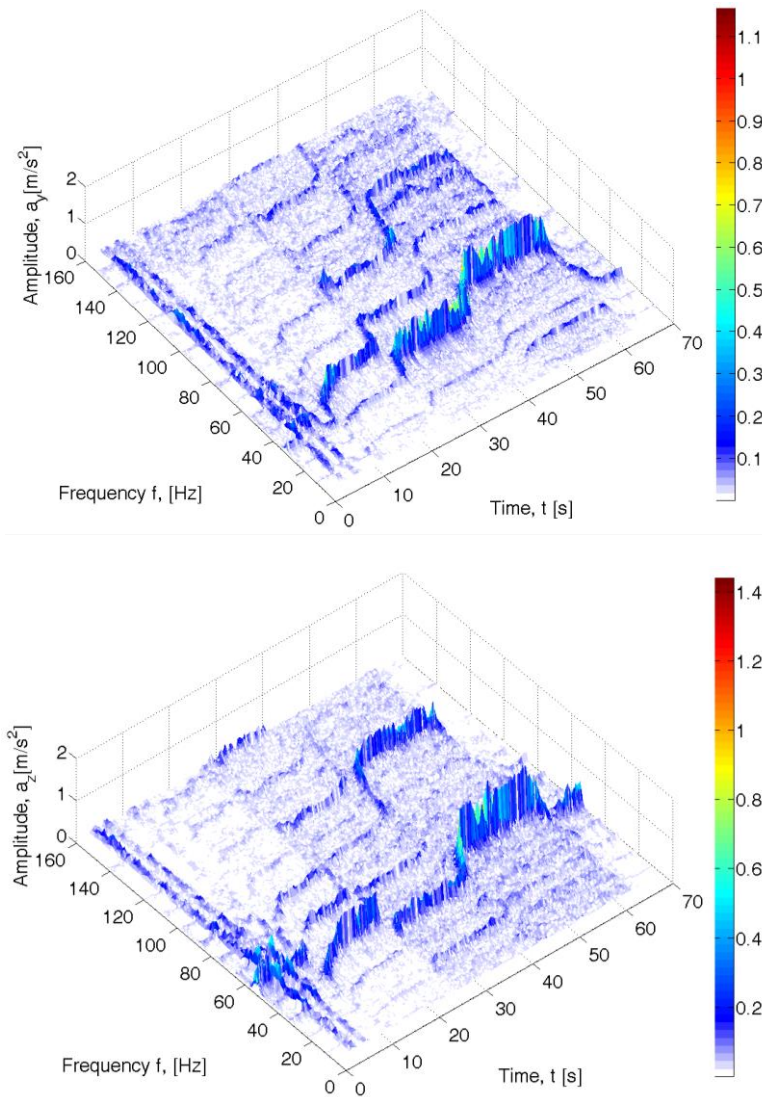
Figure 5. STFT spectrum for a malfunctioning IC
engine - identified air leak in one of the cylinders

STFT waveforms (Fig. 3, 4, 5) show the bands of local amplitudes for the components of vehicle structure vibration acceleration for given engine speeds. The occurrence of dominant amplitudes depends on both the engine speed and the set defect (no injection, spark plug socket leakage). They provide an illustrative map of

changes in amplitudes in the spectrum as a result of changes in engine speed and the given failure.

For further analysis of the acceleration signal, waveforms were used at a constant rotational speed of the engine crankshaft. Fragments of the time series of recorded signals for the speeds of 1250 rpm and 3500 rpm are presented in Figures 6, 7. The waveforms of the vehicle acceleration signal have a periodic sinusoidal shape. The specified failure causes a change in the shape of the signal. This is particularly evident in the absence of injection at a speed of 1250 rpm (Fig. 6b). At 3500 rpm, the specified defects cause signal distortion and additional harmonics.

Figure 6. Acceleration sensor signal for 1250 rpm engine speed
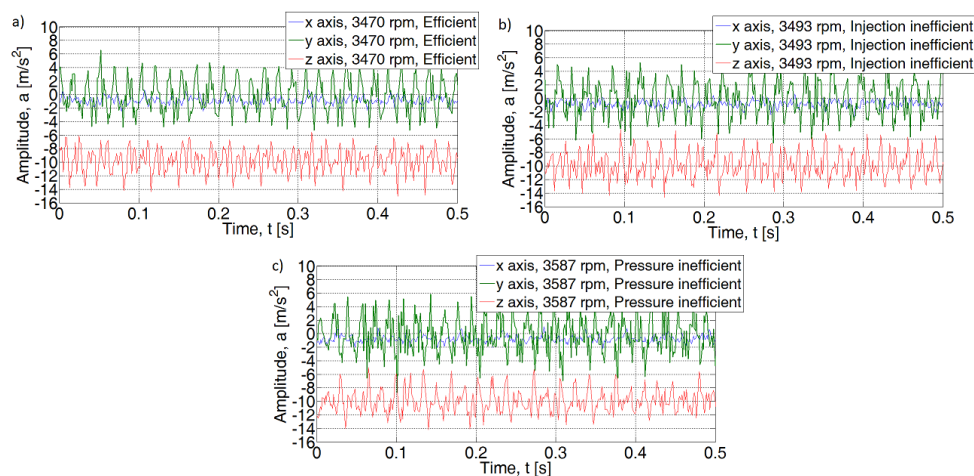
Figure 7. Acceleration sensor signal for 3500rpm engine speed

A fixed signal window value of 3 sec was adopted for the FFT transform. Then, for 1250 rpm, the acceleration signal was obtained, taking into acc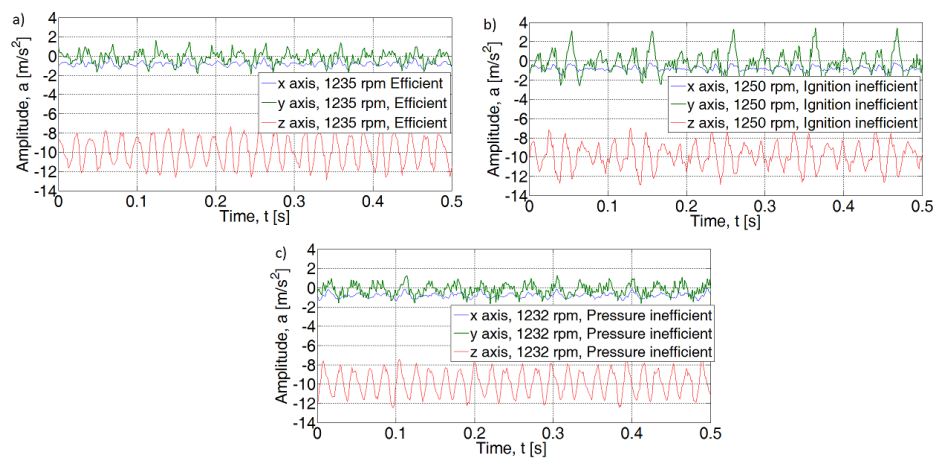ount 31 cycles of each cylinder of the internal combustion engine (1 cycle = 2 shaft revolutions). Whereas for 3500 rpm the spectrum for 87 cycles of each cylinder.

For an efficient internal combustion engine at idle, the maximum acceleration values for the basic harmonic (f_1) are: $a_x = 0.028$ m/s^2, $a_y = 0.11$ m/s^2 and $a_z = 0.13$ m/s^2 (Fig. 8). The highest acceleration values for the efficient motor were obtained for subsequent folds of the basic harmonic: y axis ($f_{1.5}$) $a_y = 0.5$ m/s^2, and for the z axis ($f_{2.5}$) $a_z = 1.05$ m/s^2. Introduced defects in the form of lack of injection into one cylinder or leakage of the spark plug caused a visible increase in the value of amplitudes for individual axes. The amount of increase depends on the type of damage. In the case of an malfunction at injection system, an increase is seen for the x axis for harmonics: (f_1, f_2, $f_{2.5}$), for the y axis: f_1, f_2, $f_{2.5}$, f_3 and the z axis: f_2 and $f_{2.5}$ (Fig. 8). The introduction of a malfunction in the form of a leak in the connection of the spark plug with the head did not introduce changes in the analyzed spectrum.
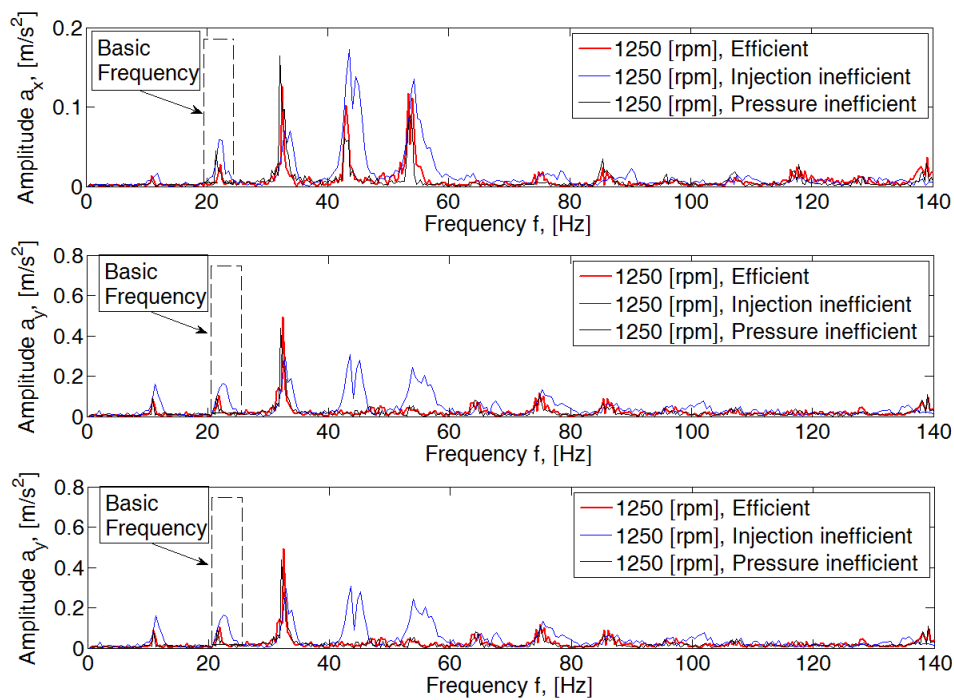
Figure 8. FFT spectral amplitude for 1250 rpm combustion engine

The increase in amplitude values is also visible for other engine speed ranges. An example of the course for the rotational speed of the crankshaft 3500 rpm is shown in Fig. 9.

Dominant amplitudes in the fundamental frequency range f_1 as well as $f_{1.5}$ and f_2 are visible in the analyzed spectrum. For an efficient motor, the amplitude values for f_1 are: $a_x = 0.18$ m/s^2, $a_y = 1.89$ m/s^2, and $a_z = 0.48$ m/s^2. An increase in the amplitudes of subsequent harmonics of the fundamental frequency (*x* axis and *y* axis) is also visible.

The introduced fault in the form of an inefficient injection system caused an increase in amplitude, which is visible for the harmonics $f_{1.5}$ and f_2 and f_1 for the *z* axis. The leakage of the candle results in an increase in the amplitudes of the *x* and *y* axis accelerations for the f_2 harmonic.

Based on the known rotational speed of the engine crankshaft, its basic frequency f_1 was determined using a frequency range window of +/- 1.5 Hz. Then dominant values of component acceleration amplitudes were determined for the n-order n = $f_{0.5}$; f_1; $f_{1.5}$; f_2; $f_{2.5}$. For the *x* axis, these values were determined as $a_{x0.5}$; a_{x1}; $a_{x1.5}$; a_{xn},
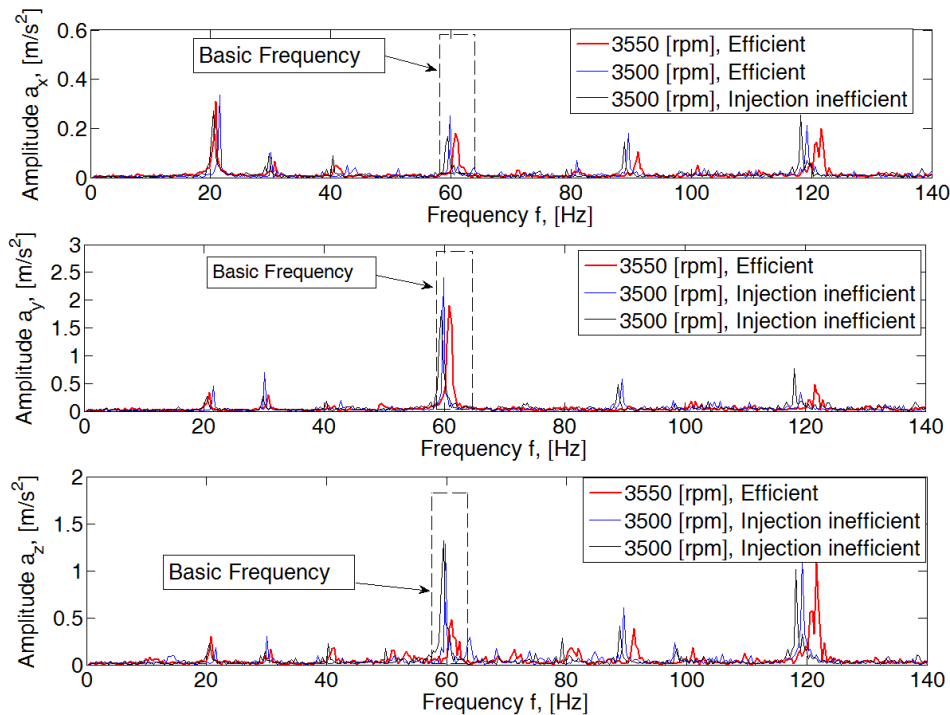
Figure 9. FFT spectral amplitude for 3500 rpm combustion engine

Then, relative values were determined for individual harmonics relative to the fundamental frequency. The obtained values take the designation A_{xn} (n-order of the analyzed basic harmonic) for individual harmonic components of the signal spectrum. Based on equation (3, 4, 5), the acceleration components for the measuring axis x, y, z were determined for the selected rotational speed of the internal combustion engine.

$$A_{xn} = \frac{a_{xn} \cdot 100}{a_{x1}} \tag{3}$$

$$A_{yn} = \frac{a_{yn} \cdot 100}{a_{y1}} \tag{4}$$

$$A_{zn} = \frac{a_{zn} \cdot 100}{a_{z1}} \tag{5}$$

Conditions have been adopted for individual residuals that determine the relationships for individual harmonics of the analyzed spectrum. The values obtained are relative to the value of the fundamental frequency signal.

Table 2. Residual specify in table for 1250 rpm

Nr resid.	Limit state WS	Logical value MD of benchmark data for specified engine condition		
		faultless	Injection malfunction	Reduced compression pressure
1	$A_{x1.0} > A_{x0.5}$	$MD11 = 1$	$MD21 = 1$	$MD31 = 1$
2	$A_{x1.5} > A_{x1}$	$MD12 = 1$	$MD22 = 1$	$MD32 = 0$
3	$(A_{x1.5} + A_{x0.5}) > A_{x1}$	$MD13 = 1$	$MD23 = 0$	$MD33 = 0$
4	$A_{x2} > A_{x1.5}$	$MD14 = 1$	$MD24 = 1$	$MD34 = 1$
5	$A_{x2.5} > A_{x2}$	$MD15 = 1$	$MD25 = 1$	$MD35 = 0$

Table 3. Benchmark values of residual for 1250 rpm

Limit state WS	Logical value ME for experimental data
$A_{x1.0} > A_{x0.5}$	$ME1$
$A_{x1.5} > A_{x1}$	$ME2$
$(A_{x1.5} + A_{x0.5}) > A_{x1}$	$ME3$
$A_{x2} > A_{x1.5}$	$ME4$
$(A_{x2.5}) > A_{x2}$	$ME5$

Table 4. IC engine identification table for 1250 rpm

Comparsion of readings (logical differential)	Logical value of state identification determinant **WD**		
MD11⇔ME1	0 = compatible 1 = incompatible	0 = compatible 1 = incompatible	0 = compatible 1 = incompatible
MD12⇔ME2 →	…..		
MD13⇔ME3	…..		
MD14⇔ME4	…..		
MD15⇔ME5	…..		
	Percenta- geshare *WS* for *WD* = 0	Percenta- geshare *WS* for *WD* = 0	Percenta- geshare *WS* for *WD* = 0

This solution does not clearly indicate the type of fault, but the probability of its symptoms. The obtained largest percentage value of the $WD = 0$ group of determinants consistent with the adopted relations ($MD = ME$) testifies to the probability of occurrence of a given fault.

4. Identification matrix

Obtained experimental data was analyzed with the use of described method basing on diagnostic matrix to identify malfunctions of the research object. A working example was shown for experimental data obtained for an engine speed of 1250 rpm. Values of acceleration components for *x*, *y*, *z* axes, specific frequency ranges (in relation to base frequency) and assumed state of the engine were shown in Fig. 8. Relative values were then determined for this portion of experimental data.

Table 5. Data analysis for 1250 rpm in *x* axis

Nr resid.	*MDx*1	*MDx*2	*MDx*3	*MEx*		*WIx*1	*WIx*2	*WIx*3
1	1	1	1	1		0	0	0
2	1	1	1	1		0	0	0
3	1	1	1	1		0	0	0
4	0	1	0	1		1	0	1
5	1	0	1	0		1	0	1
					WSx [%]	60	100	60

Table 6. Data analysis for 1250 rpm in *y* axis

Nr resid.	*MDx*1	*MDx*2	*MDx*3	*MEx*		*WIx*1	*WIx*2	*WIx*3
1	1	1	1	0		1	1	1
2	1	1	1	1		0	0	0
3	1	1	1	1		0	0	0
4	0	1	0	1		1	0	1
5	1	0	1	0		1	0	1
					WSx [%]	40	80	40

Table 7. Data analysis for 1250 rpm in *z* axis

Nr resid.	*MDx*1	*MDx*2	*MDx*3		*MEx*			*WIx*1	*WIx*2	*WIx*3
1	1	1	1		1			0	0	0
2	0	0	1		0			0	0	1
3	1	0	1		0			1	0	1
4	0	1	0		1			1	0	1
5	0	1	1		1			0	0	0
					WSx [%]			60	100	40

Table 8. Data analysis for 3500 rpm in *x* axis

Nr resid.	*MDx*1	*MDx*2	*MDx*3		*MEx*			*WIx*1	*WIx*2	*WIx*3
1	1	1	1		0			1	1	1
2	0	0	0		1			1	1	1
3	0	1	1		1			1	1	0
4	1	1	1		1			0	0	0
5	0	1	0		0			0	1	0
					WSx [%]			40	40	60

Table 9. Data analysis for 3500 rpm in *y* axis

Nr resid.	*MDx*1	*MDx*2	*MDx*3		*MEx*			*WIx*1	*WIx*2	*WIx*3
1	1	1	1		0			1	1	1
2	0	0	0		1			1	1	1
3	0	0	0		1			1	1	1
4	1	0	1		0			1	0	1
5	0	1	0		0			0	1	0
					WSx [%]			20	20	20

Table 10. Data analysis for 3500 rpm in *z* axis

Nr resid.	*MDx*1	*MDx*2	*MDx*3		*MEx*			*WIx*1	*WIx*2	*WIx*3
1	1	1	1		1			0	0	0
2	0	0	0		0			0	0	0
3	1	0	0		1			0	1	1
4	1	1	1		1			0	0	0
5	0	0	0		0			0	0	0
					WSx [%]			100	80	80

Benchmark data for diagnostic matrices *MDx*, *Mdy*, *MDz* (Tables 5-10) was obtained basing on the analysis of acceleration components and engine condition.

The determinants of the relationship (residuy) of particular harmonic axes *x*, *y*, *z* for the efficient engine were marked in columns: *MDx*1, *Mdy*1, *MDz*1. For engine with damaged injection *MDx*2, *MDy*2, *MDz*2. For a motor with a non-sealed combustion chamber: *MDx*3, *MDx*3, *MDx*3. The markers of the analyzed signal were denoted as: *MEx*, *MEy*, *MEz*.

The individual *MDn* reference data were compared with resi - des of the tested *MEn* signal, obtaining information on existing relations. In the case of compliance (e.g. *MDx*1 (1) and *MEx* (1)) for 1250 rpm (Tab. 4), the value of *WIx*1 (1) is 0. In the case of non-compliance (eg *MDx*1 (2) and *MEx* (2)), the value of *WIx*1 (2) is 1.

By analyzing specific measurement data for the engine, a percentage probability of its state was obtained. Data analysis for identified malfunctions in the form of time gap in fuel injection and air leak in one of engine cylinders is shown in Tables. 5, 6, 7. Show case data analysis for 1250 rpm, whereas Tables 8, 9, 10 show data analysis for 3500 rpm.

Identification matrices allow to identify time gap in fuel injection with 100%, 83%, 100% in *x*, *y*, *z* axes, and an air leak within the engine cylinder with 67%, 50%, 50% probability (in *x*, *y*, *z* axes) for 1250 rpm. For the analyzed signal, the greatest probability of engine failure was defined as pressure damage. For increased engine speed (3500 rpm), there are lower signal distortion. As a result, identifying malfunctions based on the presented diagnostic matrix is more difficult, and the accuracy of decisions is burdened with a significant error. It is therefore necessary to develop a relationship for comparing harmonics for individual characteristic speeds of an internal combustion engine.

5. Conclusions

The presented research has shown that it is possible to identify engine malfunctions by analyzing the harmonic components of vehicle chassis vibrations with the use of residuals. Two distinct engine failures were purposefully introduced to an investigated spark-ignition engine mounted in RZR 1000 ATV- time gap in fuel injection and air leak in engine cylinder. The tests were carried out for various engine speeds without additional load.

In the area of low frequencies, it was observed that the specified engine failure (no injection or damage to one of the cylinders) causes a change in the amplitude of vibration accelerations for a frequency corresponding to 0.5; 1; 1.5; 2 and 2.5 engine speeds f_o.

Analysis of the relative values of the components of harmonic amplitudes noted differences in spectral lines resulting from malfunction of the engine. This allowed the authors to formulate a reasoning matrix for identifying engine failure basing on comparative analysis of harmonic components. In future research, it would seem beneficial to conduct a similar analysis of harmonic components for different engine speeds and to specify a diagnostic criterion.

In the developed diagnostic matrix to identify the malfunction of the internal combustion engine based on the vibration of the vehicle structure, changes in the amplitudes of the individual harmonics of the signal in the spectrum were used.

This solution is an alternative to diagnostic inference in real vehicle operation conditions, due to the easy installation of the sensor. It should be noted, however, that the measurement is indirect, and the results presented do not take into account the effect of dissipative elastic elements of engine mounting to the vehicle structure. This compaction is a further part of the work carried out as part of the vehicle vibration analysis in terms of safety and comfort, and early identification of damage.

References

1. J. A. Wajand, J. T. Wajand, *Medium and high speed piston internal combustion engines* (in Polish), WNT, Warsaw 2000.
2. J. Grajales, H. Quintero, J. López, C. Romero, E. Henao, O. Cardona, *Engine diagnosis based on vibration analysis using different fuelblends*, Diagnostic **18**(4) (2017) 27 – 36.
3. J. A. Grajales, H. F. Quintero, C. A. Romero, E. Henao, J. F. López, D. Torres, *Combustion pressure estimation method of a spark ignited combustion engine based on vibration signal processing*, Journal of Vibroengineering, **18**(7) (2016) 4237 – 4247.
4. A. Taghizadeh-Alisaraei, A. Mahdavian, *Fault detection of injectors in diesel engines using vibration time-frequency analysis*, App. Acoustics, **143** (2019) 48 – 58.
5. J. Flett, G. M. Bone, *Fault detection and diagnosis of diesel engine valve trains*, Mech. Sys. and Sig. Proc., **72-73** (2016) 316 – 327.
6. Z. Geng, J. Chen, J. B. Hull, *Analysis of engine vibration and design of an applicable diagnosing approach*, Int. J of Mech. Sciences, **45**(8) (2003) 1391 – 1410.
7. M. Ettefagh, M. Sadeghi, V. Pirouzpanah, H. Arjmandi Tash, *Knock detection in spark ignition engines by vibration analysis of cylinder block: A parametric modeling approach*, Mech. Sys. and Sig. Proc., **22** (2008) 1495 – 514.
8. S. Delvecchio, P. Bonfiglio, F. Pompoli, *Vibro-acoustic condition monitoring of Internal Combustion Engines: A critical review of existing technique*, Mech. Sys. and Sig. Proc., **99** (2018) 661 – 683.
9. R. Sroka, *Determining the impact of switching off ZI engine cylinders on changes in the engine's vibroacoustic signal* (in Polish), Transport, Silesian University of Technology 2008.
10. R. Burdzik, *Research on the influence of engine rotational speed to the vibration penetration into the driver via feet - multidimensional analysis*, J of Vibroeng., **15**(4) (2013) 2114 – 2123.
11. J. Dziurdź, *Analysis of nonlinear phenomena in the diagnosis of vehicle propulsion systems* (in Polish), Warsaw-Radom 2013.
12. K. Jafarin, M. Mobin, R. Jafari-Marandi, E. Rabiei, *Misfire and valve clearence faults detaction in the combustion engines based on a multi- sensor vibration signal monitoring*, Measurement, **128** (2018) 527 – 536.

13. K. Prażnowski, J. Mamala, *Problems in Assessing Pneumatic Wheel Unbalance of a Passenger Car Determined with Test Road in Normal Conditions*, SAE Tech. Pap., Grand Rapids 2017.
14. K. Prażnowski, J. Mamala, *Classification of the road surface condition on the basis of vibrationsof the sprung mass in a passenger car*, IOP Conference Series: Mat. Scienc. and Engineering, Zakopane 2016.
15. J. Korbicz, J. Kościelny, Z. Kowalczuk, W. Cholewa, *Process diagnostics, Models, artificial intelligence methods, applications* (in Polish), WNT Warszawa 2002.

Identification of Characteristic Vibration Signal Parameters During Transport of Fruit and Vegetable

Natalia IDASZEWSKA
Institute of Machines and Motor Vehicles Poznan University of Technology,
Piotrowo 3, 60-965 Poznań, natalia.idaszewska@put.poznan.pl

Grzegorz M. SZYMAŃSKI
Institute of Combustion Engines and Transport, Poznan University of Technology,
Piotrowo 3, 60-965 Poznań, grzegorz.m.szymanski@put.poznan.pl

Abstract

The occuring vibrations during the transport of fruit and vegetables contributes to damage and accelerates their deterioration. In order to protect transported products against negative changes caused by vibrations during transport, it is necessary to know the values of these vibrations. The article presents the identified characteristic parameters of the vibration signal during transport of fruit and vegetables. The experimental investigations of the actual mechanical loads were carried out on various roads during transport by selected vehicles. Vibration spectra that represented the relation between the acceleration amplitudes and the vibration frequencies were obtained and analyzed. The vibration spectral analysis identified characteristic repetitive values of vibration signal parameters.

Keywords: transport of fruit and vegetable, vibrations

1. Introduction

Fruit and vegetables are one of the most popular food products. They play an important role in human food consumption because they are a rich source of vitamins and minerals, fiber and antioxidants. Consumption of fruits and vegetables is an important factor in the prevention of a variety of diseases including heart conditions [1-5], cancer [6-11] gastric diseases [12, 13] as well as metabolism related diseases [13-16].

Increasing consumer awareness and migration of people from different regions of the world cause greater interest in exotic species resulting from the fact of prolonged transport from distant regions of the world. Transporting fruit and vegetables is a difficult task, because these products are living tissue in which life processes take place constantly. These processes result in the development of sensory features desired by the consumer, but at a later stage lead to the deterioration of products, which in turn generates large losses.

A common phenomenon practiced to prolong the durability during their transportation is transport of unripe fruit and vegetable. This practice is caused by the necessity of long transport over long distances, transporting exotic fruit species from distant areas. Transportation of unripe fruit and vegetable prevents adverse changes occurring in fruits and vegetables, deterioration of quality and even damages, which generates financial losses. Fruits and vegetables that are delivered to the region of consumption are frequently subject to forced ripening through the application of ethylene, which completes the process

in just a few hours. Such practices may adversely affect some sensory features deteriorating the quality of the produce.

To maintain the highest possible quality of fruits and vegetables during transport, they should be provided with appropriate climate conditions that can slow down the processes that occur, thus protecting them from deterioration. Transport, however, introduces another parameter - vibrations. The occurrence of vibrations contributes to damage in transported products [17, 18]. Vibration that generates constant impacts and rubbing of the neighboring fruits and vegetables leads to the formation of bruises on their surface, which may even lead to juice secretions [19]. This, in turn, initiates the appearance of rotting processes which results in spoilage of the transported load. Vibrations negatively affect on the quality of fruits and vegetables, which, losing their original shape, are not suitable for direct sale, and often for further processing.

Numerous investigations show the negative impact of vibrations on transported fruit and vegetables, which result the form of dents, scratches and rotten spots. However, there is a lack of information on the exact values of vibration parameters, which vary depending on the region in the world where fruit and vegetables are transported. It is therefore necessary to know the exact parameters of the vibration signal when transporting fruit and vegetables on various roads and with different types of vehicles for transporting fruit and vegetables. If the vibrations contribute to the deterioration of products during transport, it can be assumed that their impact on transformations in transported products is as important as the influence of other factors (temperature, humidity). Knowledge about the value of specific vibration parameters may be significant in later determining the impact of these vibrations on the physicochemical parameters of fruits and vegetables, and this in turn can significantly facilitate the decision on the date of harvesting these products depending on the place of their distribution. This could contribute to reducing losses during fruit and vegetable transportation and at the same time help to preserve the best sensory and health features of fruit and vegetables without having to practice subjecting them to forced ripening.

2. Methodology

Within the preliminary investigations, measurements were carried out of the actual vibration during transport of fruits with a Lambert trailers on the distance of approx. 500 km. The trailers were loaded with Europalets with crates filled with 3 kg of fruits each (loose). The fruits were loose in the crates. The temperature in the trailer was approx. 5°C. The vibration sensor was fitted in the front of the trailer on the bottom of the highest placed crate. Upon loading the trailer, the vibration recorder was initiated. The recording lasted for 7 hours in each vehicle. After the trailer was filled with load, the vibration recorder was started to record. The recording was carried out for the next 7 hours, determined by the recorder's battery life. The computer program for recording vibrations was set in such a way that the recording was divided into 7 1-hour-long sections. The data were saved on a memory card located in the recorder, and their reading was possible after returning the vehicle to the place where the measurements began. The measurement was made on three different vehicles when they were stationary (refrigeration unit switched on) described STOP and on two different roads. To measure the vibration signal parameters occurring

during road transport, a measuring system was used, the diagram of which is shown in Figure 1.
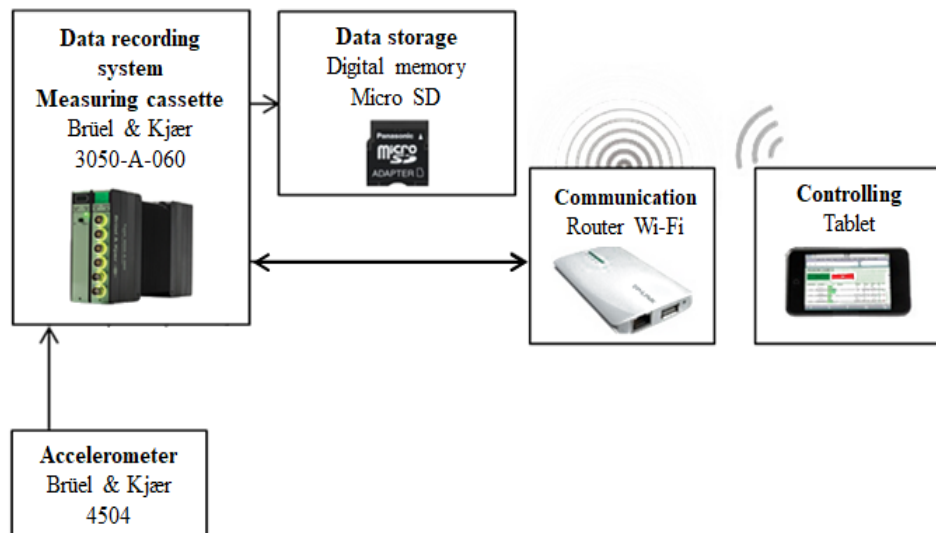

Figure 1. Diagram of the vibration measurement stand

The measurements system was composed of transducer (type 4504) connected to a wi-fi router and a battery-powered vibration recorder (LAN-XI Notar) capable of storing the recorded data on a flash memory card. The recorder was initiated via wi-fi from a portable computer. The computer had PULSE system data acquisition software. The transducer, the data recorder and the software were manufactured by Brüel&Kjær. Vibrations in the vertical direction were recorded. Since these are the first such tests at the Institute of Machines and Motor Vehicles, no tests related to vibration transmittance have been performed.

3. Analysis of results

Based on the investigations of the vibration signals carried out in actual traffic, vibration frequencies were assessed that dominate in the vibration signals during the transport of fruits. The recorded vibration signals shown in Figure 2 were subjected to time-frequency analysis and frequency analysis using the assumptions of the Fourier transform.
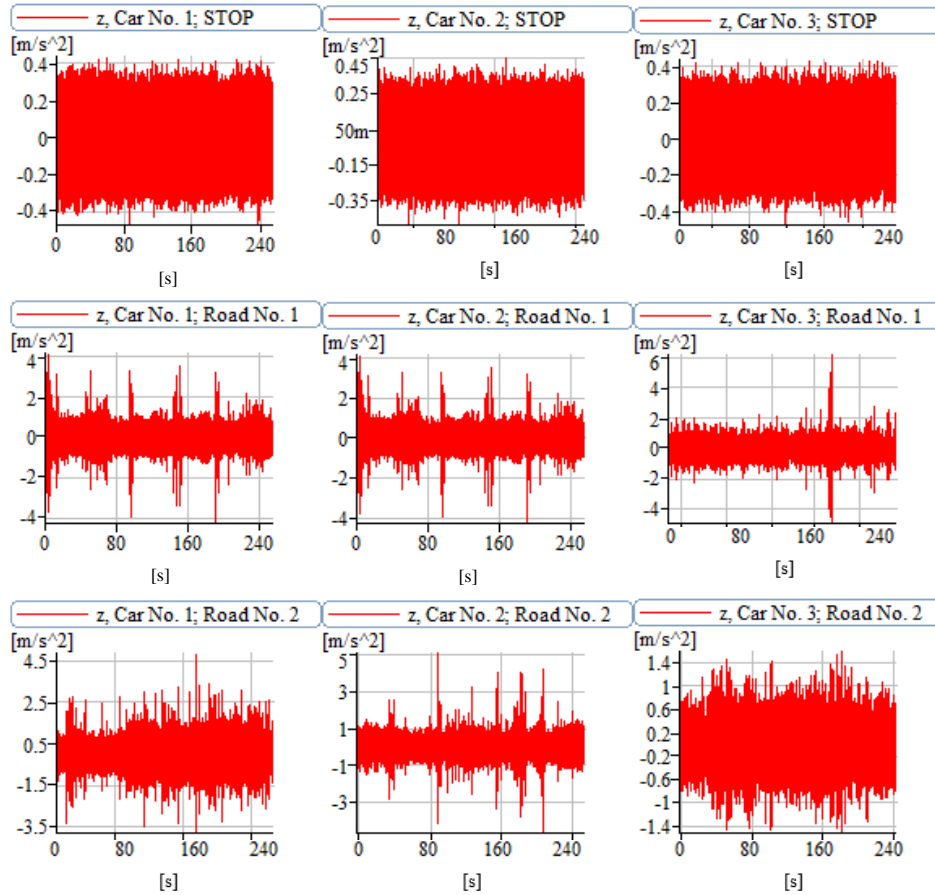
Figure 2. Time history of vibration recorded during the transport under actual traffic conditions for different vehicles when they were stationary (only refrigeration unit switched on) described STOP and on two different roads

Based on the waveforms shown in Fig. 2, the signals were found to be non-stationary. Therefore, time-frequency analysis (STFT) was performed to check amplitude and frequency stationarity. The STFT result can be treated as a series of spectra determined for local, short time segments of time history [20].

$$STFT\left[x_w(t,\tau)\right] = X_w(f,\tau) = \int_{-\infty}^{\infty} w(t,\tau)x(t)\cdot e^{-i2\Pi ft}dt \qquad (1)$$

where: $x(t)$ – time course representing analyzed input signal; $w(t)$ – time window function (tapering function); τ – position of time window in time domain.

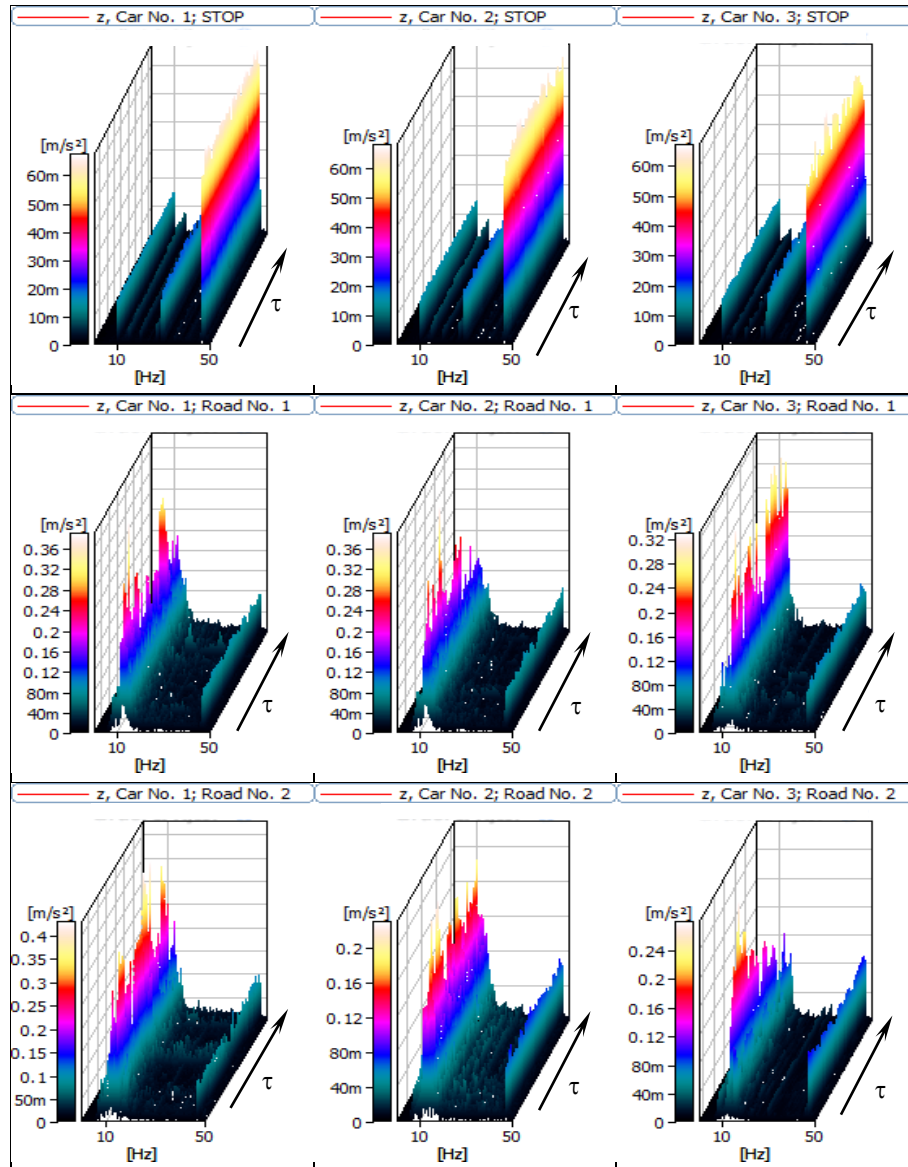The results of the STFT analysis are presented in Fig. 3.

Figure 3. Results of time-frequency analysis during the transport under actual traffic conditions for different vehicles when they were stationary (only refrigeration unit switched on) described STOP and on two different roads

Based on the STFT on Fig. 3 it was found that there are characteristic vibration frequency bands generated during transport of fruit and vegetables. Figure 4 presents the FFT spectrum of the vibration recorded during the transport of the fruits.
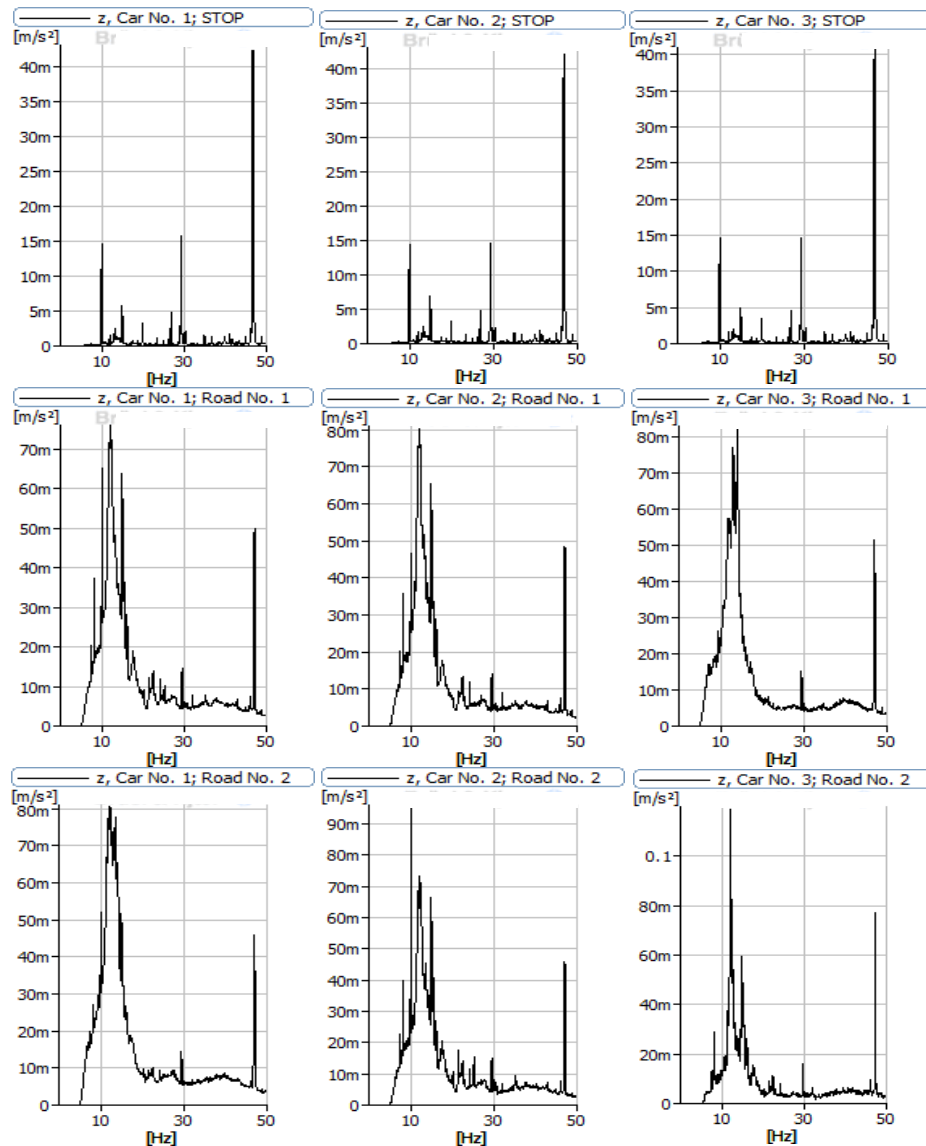
Figure 4. Results of FFT analysis for signals recorded during the transport under actual traffic conditions for different vehicles when they were stationary (only refrigeration unit switched on) described STOP and on two different roads

Based on spectrum analysis, the characteristic vibration frequencies were estimated:
- for the STOP case: 10 Hz, 29 Hz, 47 Hz.
- for the Car No. 1; Road No. 1 case: 12.25 Hz, 29 Hz, 47 Hz,

- for the Car No. 2; Road No. 1 case: 12.25 Hz, 29 Hz, 47 Hz,
- for the Car No. 3; Road No. 1 case: 14 Hz, 29 Hz, 47 Hz,
- for the Car No. 1; Road No. 2 case: 12.25 Hz, 29 Hz, 47 Hz,
- for the Car No. 2; Road No. 2 case: 12.25 Hz, 29 Hz, 47 Hz,
- for the Car No. 3; Road No. 2 case: 12,25 Hz, 29 Hz, 47 Hz.

3. Using of identified parameters of vibration signals

Based on data obtained during experimental tests (during driving time) was estimated by energy supplied to the load for one hour, as a result of vibration processes. Based on the analysis of characteristics in Fig. 4 it was found that the analyzed vibration signals aren't monoharmonic. Therefore, a_{RMS} were estimated for frequency bands with a width of 15 Hz and central frequencies presented in chapter 2.

Knowing the equivalent value of vibration acceleration, the dose of vibration was determined to enable comparison of changes that took place in fruits subjected to vibration of different duration. The vibration dose was determined on the basis of the following relationship [21]:

$$eVDV = k \cdot a_{RMS} \cdot t^{0.25} \tag{2}$$

where: eVDV is Estimated Vibration Dose Value [m/s$^{1.75}$], a_{RMS} is weighted equivalent value of vibration acceleration [m/s^2], t is time [s], k is nominally 1.4 for crest factors below 6.

Figure 5 shows an example of estimating the a_{RMS} value in the frequency band 12.25±7.5 Hz. Delta means the a_{RMS} value of vibration in the marked frequency band.

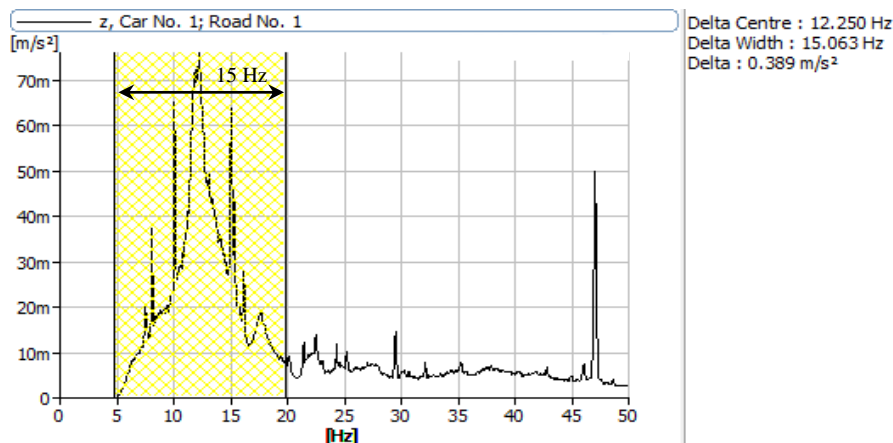Figure 6. An example of estimating the a_{RMS} value in the frequency band 12.25±7.5 Hz

Tables 1-3 presents the eVDV to the produce depending on the frequencies, acceleration amplitudes and vibration displacement for stationary vehicle and on 2

different roads. EVDV values for all vehicles were very similar, therefore results for only one vehicle (Car 1) were presented.

Table 1. Calculation of Estimated Vibration Dose Value supplied to the produce depending on the frequency; vehicle is stationary; Car 1

	Vibration frequency [Hz]	a_{RMS} [m/s^2]	Time [s]	eVDV [m/s$^{1.75}$]
Vehicle is stationary	10	0.017	3600	0.18
	29	0.021	3600	0.23
	47	0.061	3600	0.66

Table 2. Calculation of Estimated Vibration Dose Value supplied to the produce depending on the frequency; road 1

	Vibration frequency [Hz]	a_{RMS} [m/s^2]	Time [s]	eVDV [m/s$^{1.75}$]
Car 1	12.25	0.389	3600	4.22
	29	0.076	3600	0.82
	47	0.095	3600	1.03
Car 2	12.25	0.395	3600	4.28
	29	0.075	3600	0.81
	47	0.096	3600	1.04
Car 3	12.25	0.415	3600	4.50
	29	0.064	3600	0.69
	47	0.103	3600	1.12

Table 3. Calculation of Estimated Vibration Dose Value supplied to the produce depending on the frequency; road 2

	Vibration frequency [Hz]	a_{RMS} [m/s^2]	Time [s]	eVDV [m/s$^{1.75}$]
Car 1	12.25	0.482	3600	5.23
	29	0.091	3600	0.98
	47	0.111	3600	1.20
Car 2	12.25	0.384	3600	4.16
	29	0.078	3600	0.85
	47	0.092	3600	1.00
Car 3	12.25	0.314	3600	3.41
	29	0.048	3600	0.52
	47	0.106	3600	1.15

6. Conclusions

Based on the investigations of the vibration signals carried out in actual traffic during the transport of fruits in different vehicles and on two different type of road, characteristic and domination vibration frequencies were assessed that dominate in the vibration signals. Based on the spectra obtained, the following values were estimated vibration dose supplied to the produce for one hour. For stationary vehicle the highest eVDV supplied to the

produce is about 0.66 m/s$^{1.75}$ for central frequency 47 Hz and the lowest eVDV supplied to the produce is 0.18 m/s$^{1.75}$ for central frequencies 10 Hz. For the road no 1 the highest eVDV supplied to the produce is about 4.50 m/s$^{1.75}$ for central frequencies 12.25 Hz and the eVDV is significantly lower for other frequencies (Car 3). For the road no 2 the highest eVDV supplied to the produce is about 5.23 m/s$^{1.75}$ for central frequencies 12.25 Hz and is lower for other frequencies (Car 1). The lowest eVDV supplied to the produce during transport is about 0.52-0.98 m/s$^{1.75}$ for central frequencies 47 Hz. Based on the results of the research, it will be possible to build a stand for simulation of the process of fruit and vegetable transport in the vibration aspect.

Acknowledgments

References

1. L. Dauchet, P. Amouyel, J. Dallongeville, *Fruits, vegetables and coronary heart disease*, Nat. Rev. Cardiol., **6**(9) (2009) 599 – 608.

2. D. Chen, C. Huang, Z. Chen, *A review for the pharmacological effect of lycopene in central nervous system disorders*, Biomed. Pharmacother., **111** (2019) 791 – 801, doi:10.1016/j.biopha.2018.12.151.

3. I. Klein, *Cardiovascular disease and Cardiovascular Disease*, Braunwald's Hear. Dis. - A Textb. Cardiovasc. Med., (2011) 1829 – 1843.

4. L. Ma, Z. Sun, Y. Zeng, M. Luo, J. *Yang, Molecular Mechanism and Health Role of Functional Ingredients in Blueberry for Chronic Disease in Human Beings*, Int. J. Mol. Sci., **19** (2018) 2785, doi:10.3390/ijms19092785.

5. C. N. Zhao, X. Meng, Y. Li, S. Li, Q. Liu, G. Y. Tang, H. Bin Li, *Fruits for prevention and treatment of cardiovascular diseases*, Nutrients., **9** (2017) 1 – 29, doi:10.3390/nu9060598.

6. K. E. Bradbury, P. N. Appleby, T. J. Key, *Fruit, vegetable, and fiber intake in relation to cancer risk: Findings from the European Prospective Investigation into Cancer and Nutrition (EPIC)*, Am. J. Clin. Nutr., **100** (2014) 1 – 4, doi:10.3945/ajcn.113.071357.

7. A. Chothiphirat, K. Nittayaboon, K. Kanokwiroon, T. Srisawat, R. Navakanitworakul, *Anticancer Potential of Fruit Extracts from Vatica diospyroides Symington Type SS and Their Effect on Program Cell Death of Cervical Cancer Cell Lines*, Sci. World J., **2019** (2019) 1 – 9, doi:10.1155/2019/5491904.

8. Y. Jeong, J. W. Lim, H. Kim, *Lycopene Inhibits Reactive Oxygen Species-Mediated NF-κB Signaling and Induces Apoptosis in Pancreatic Cancer Cells*, Nutrients., **11** (2019) 762, doi:10.3390/nu11040762.

9. R. Reiss, J. Johnston, K. Tucker, J. M. DeSesso, C.L. Keen, *Estimation of cancer risks and benefits associated with a potential increased consumption of fruits and vegetables*, Food Chem. Toxicol., **50** (2012) 4421 – 4427.

10. A. R. Vieira, L. Abar, S. Vingeliene, D. S. M. Chan, D. Aune, D. Navarro-Rosenblatt, C. Stevens, D. Greenwood, T. Norat, *Fruits, vegetables and lung cancer risk: A systematic review and meta-analysis*, Ann. Oncol., **27** (2016) 81 – 96, doi:10.1093/annonc/mdv381.

11. J. W. Wang, C. G. Zhang, Q. L. Deng, W. L. Chen, X. Wang, J. M. Yu, *The associations of comorbidities and consumption of fruit and vegetable with quality of life among stomach cancer survivors*, Health Qual. Life Outcomes, **16** (2018) 1 – 7, doi:10.1186/s12955-018-0886-y.

12. J. H. Kim, J. Lee, I. J. Choi, Y.-I. Kim, O. Kwon, H. Kim, J. Kim, *Dietary Carotenoids Intake and the Risk of Gastric Cancer: A Case—Control Study in Korea*, Nutrients., **10** (2018) 1031, doi:10.3390/nu10081031.

13. B. Peleteiro, P. Padrão, C. Castro, A. Ferro, S. Morais, N. Lunet, *Worldwide burden of gastric cancer in 2012 that could have been prevented by increasing fruit and vegetable intake and predictions for 2025*, Br. J. Nutr., **115** (2016) 851 – 859, doi:10.1017/s000711451500522x.

14. W. Brown, I., Rosner, B., Willett, *Cholesterol-lowering effects of dietary fiber: a meta-analysis*, Am. J. Clin. Nutr., **69** (1999) 30 – 42.

15. C. E. Butterworth, *Vitamin safety: a current appraisal*, Vitam. Nutr. Inf. Serv., **5** (1994) 1 – 10.

16. W. Wang, H. Lu, S. Zhang, Z. Yang, *Damage caused by multiple impacts of litchi fruits during vibration harvesting*, Comput. Electron. Agric., **162** (2019) 732 – 738, doi:10.1016/j.compag.2019.04.037.

17. H. M. Jung, S. Lee, W.-H. Lee, B.-K. Cho, S.H. Lee, *Effect of vibration stress on quality of packaged grapes during transportation*, Eng. Agric. Environ. Food., **11** (2018) 79 – 83, doi:10.1016/J.EAEF.2018.02.007.

18. X. Wei, D. Xie, L. Mao, C. Xu, Z. Luo, M. Xia, X. Zhao, X. Han, W. Lu, *Excess water loss induced by simulated transport vibration in postharvest kiwifruit*, Sci. Hortic., **250** (2019) 113 – 120, doi:10.1016/j.scienta.2019.02.009.

19. R. Zhou, X. Wang, Y. Hu, G. Zhang, P. Yang, B. Huang, *Reduction in Hami melon (Cucumis melo var. saccharinus) softening caused by transport vibration by using hot water and shellac coating*, Postharvest Biol. Technol. **110** (2015) 214 – 223, doi:10.1016/j.postharvbio.2015.08.022.

20. R. Barczewski, G. M. Szymański, *Application of the time-frequency selection of the vibration to valve clearance assessment of a diesel engine*, Diagnostyka, **30** (2004) 18 – 22 (in Polish).

21. D. Więckowski, *Analysis domain of the time vertical vibration on account comfort child during ride in the car*, Czasopismo Techniczne, **109** (2012) 73 – 91 (in Polish).

Short Time Vibration Analysis and Parameterisation as a Tool for Machine Prototypes Testing

Roman BARCZEWSKI

Poznan University of Technology, Faculty of Mechanical Engineering,
3 Piotrowo St, 60-965 Poznan, roman.barczewski@put.poznan.pl

Abstract

The paper outlines the idea of using the short-time vibration signal processing for testing machines of a complex design, particularly the machines consisting of many subassemblies with a non-stationary (e.g. cyclic) operation modes. The method presented consists in graphic representation of vibrations of subassemblies in the form of a trace on a plane. It is created by associating instantaneous rms values of vibration acceleration and instantaneous Rice frequency values obtained as a result of short-time signal processing. On the basis of the shape, orientation of the created trajectory and / or dispersion / concentration of points on the $R_f - a_{\mathrm{rms}}$ plane, the type of non-stationarity of generated vibrations can be identified. The presented methodology can be used for testing machine prototypes. The results in the proposed form can be helpful to determine the type of vibration reduction systems for individual machine subassemblies. It is also possible to detect subassemblies for which an increase in machine capacity results in an increase in the level of generated vibrations. The location of the averaged values of measures obtained for a new machine on the $R_f - a_{\mathrm{rms}}$ plane can be a reference point for further monitoring of machine vibration and for detection of damage or malfunction of its subassemblies.

Keywords: machine vibration, non-stationarity identification, short time signal analysis

1. Introduction

A group of machines can be distinguished for which the methodology of the assessment of their technical condition on the basis of vibration measurements, specified in standards (e.g. [1, 2]) is not adequate. This may result from the range of rotation speeds or from the variety and specifics of working movements (not necessarily rotational) performed by machine subassemblies. Machines with a complex design and additionally with many drive units (e.g. electric motors, pneumatic cylinders) are used, among others in the food, textile and tobacco industry. In this case, the evaluation of machine vibrations based on the aforementioned standards is not justified. Therefore, the problem arises how to run prototype tests and how to assess the technical condition of this class of machines during operation. Methods are sought and developed that allow detection of machine malfunctions. One of possible solutions is to use the change of poles location – natural frequency and damping ratio in order to detect and localize the machine malfunctions [3].

In this paper the author proposes a slightly different approach to running vibration tests of machines of a complex design. It uses a graphic representation of results of short-time processing of vibration signals recorded at representative measuring points located on individual subassemblies of the machine. This method involves synchronous determination and visualization of the location of instantaneous rms values of vibration accelerations $a_{\mathrm{rms}}(\tau)$ and Rice frequencies $R_f(\tau)$ on the $R_f - a_{\mathrm{rms}}$ plane. This approach allows one to determine the specifics of the operation of subassemblies e.g. during prototype

testing. On the other hand, the observation of the change of the position on the $R_f - a_{rms}$ plane of the averaged $R_f(\Theta)$ and $a_{rms}(\Theta)$ values during operation time Θ can be the basis for detection of malfunctions of subassemblies.

The paper presents an outline of the proposed alternative methodology and sample results obtained during vibration tests of the prototype of a horizontal tray former. The purpose of this research (in the short term aspect) was to obtain data that can be helpful for optimizing the construction of the prototype of the former and for selection of vibration elimination systems. Test results (in the averaged values aspect) can be treated as reference values for further monitoring of the technical condition of the machine during operation.

2. The test object

The FTHT6 former (Fig. 1) is a modular machine used for the erection of cardboard trays. This machine has a cyclical operation mode. It consists of several cooperating subassemblies which make various working movements: rotations of variable speed as well as reciprocating and complex movements. Some phases of forming and bonding of a cardboard have an additional impact nature (e.g. bending, pressure during the gluing phase).
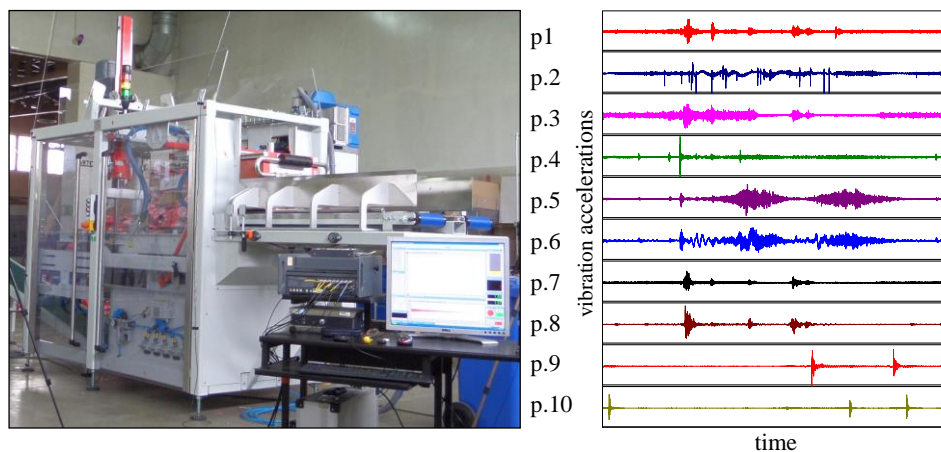

Figure 1. FTHT 6 former and vibration accelerations recorded at representative measuring points p.1 – p.10 (one machine operation cycle is presented) [4]

The research was carried out for the rated cardboard formation speed, i.e. 25 cycles per minute. Vibration accelerations were recorded at 10 representative points located on the former's prototype:

        1 – cardboard manipulator beam (lower),
        2 – cardboard manipulator rotary beam (upper),
        3 – servo drive beam,
        4 – punch gearmotor base,
        5 – punch guide,
        6 – punch,

7 – transverse beam for cardboard slide (at the end),
8 – the end of the guide (channel bar),
9 – cardboard bender,
10 – pneumatic clamp (pressure).

Their locations were determined on the basis of kinematic analysis of the machine and suggestions from the construction team. Figure 1 also shows a fragment of recorded vibration accelerations covering one cycle of operation. The variety of dynamic interactions of individual subassemblies is visible.

3. Methodology

Vibration accelerations at representative points were recorded synchronously due to the specificity of dynamic interactions, the complexity of the FTHT6 former and its high capacity. For the vibration tests of the prototype of the former eight IMI® (type 627A01, 603C01) and two MMF (type KD10) accelerometers were used. The signals from the ICP (IMI) standard transducers were recorded directly by an eight-channel recording unit TEAC LX-10. The signals from the charge transducers (KD10) were pre-conditioned in a preamplifier (Nexus B&K) and recorded by a two-channel data acquisition module VibDAQ 2+. The way the transducers were mounted and the analog-to-digital conversion parameters (sampling frequency 6 kHz, 24 bit quantization) ensured a linear vibration measurement with an appropriate dynamics in the frequency band to a minimum of 3 kHz.

The signals were analysed and parameterised in an application developed in the DASYLab (Data Acquisition System Laboratory) environment. The digital signal processing included: signal windowing, STFT (*Short Time Fourier Transform*) analysis [5, pp 46-52] as well as, basing on time-frequency (TF) maps, the determination of instantaneous rms values of vibration accelerations $a_{rms}(\tau)$, instantaneous Rice frequencies $R_f(\tau)$ and creating a display of results on the $R_f - a_{rms}$ plane. Further data synthesis and parameterization were enabled.

A rectangular time window with a size of 512 samples was used to segment the data in the process of signal processing. As a result, short-time, 0.085-second-long signal sequences were obtained. The time window shift $\Delta\tau$ in the STFT analysis was equal to the window size (overlapping = 0). TF maps were the basis for further parameterisation of vibration accelerations. An example of such a map (2D and 3D) is shown in Figure 2. The sonogram shows a broadband impulse and subsequent monoharmonic damped vibrations of the bender (measurement point no. 9) with a frequency of approx. 75 Hz.
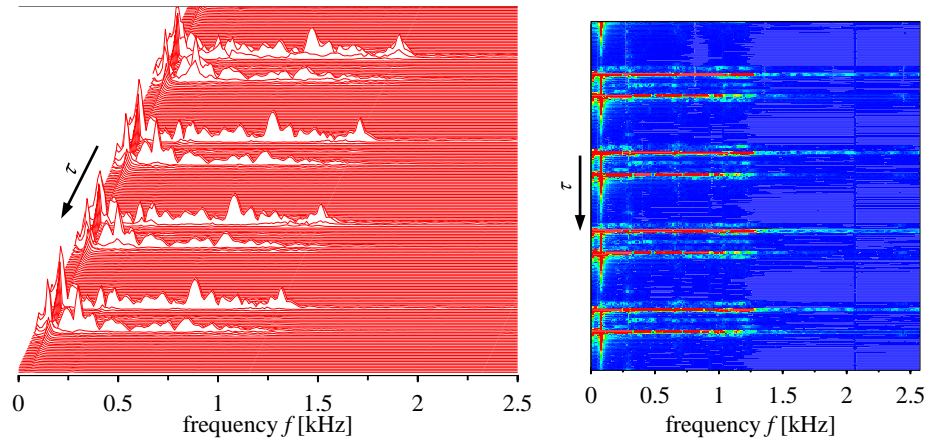
Figure 2. An example of STFT analysis covering four operation cycles of the former (accelerations recorded at the measurement point no. 9 – cardboard bender) [4]

It should be mentioned that Rice frequency R_f describes the average frequency of the analysed process [6]. It is used, among others, in the diagnostics of rolling bearings, for the detection of damage of valves in internal combustion engines [7] and cavitation [8]. The Rice frequency can be determined based on power density spectra [9 pp 84-85]. Bearing this in mind, the instantaneous Rice frequency values $R_f(\tau)$ can be obtained as a result of post-processing of subsequent short-time spectra with the following formula [10]:

$$R_f(\tau) = \left[\frac{\int_0^\infty f^2 X_a(f,\tau)df}{\int_0^\infty X_a(f,\tau)df} \right]^{\frac{1}{2}} \tag{1}$$

where:

$X_w(f,\tau)$ – sonogram obtained as a result of STFT of $a(t)$ signal,
f – frequency,
τ – shift of the analysis time window.

The properties of the obtained $R_f(\tau)$ characteristics and methods of its further parameterisation are shown in a monograph by the author [11]. Bearing in mind the Parseval's theorem [12, p. 134] instantaneous $a_{rms}(\tau)$ values can be easily determined by synthesizing short-time spectra. A similar method of determination (calculation) of the rms value of the signal from the spectrum was used in another work [13]. As part of the research, averaged values of the measures $\check{R}_f$ and $\check{a}_{rms}$, for 20 s of signal covering 10 complete machine cycles were also determined.

It should be added that the determination of the above measures based on post-processing of TF maps gives a possibility of conducting a selective analysis in any

frequency range. This is done by taking into account in the processing of components of a TF map located between arbitrarily set cutoff frequencies.

4. Results

An idea of interpreting the results of short-time parameterisation of vibrations is shown in Figure 3. It can be intuitively determined whether the signal is stationary or non-stationary in the amplitude and / or frequency terms. The proposed method can be an alternative to the methods of detecting signal instability described by Plazenet et. al [14].
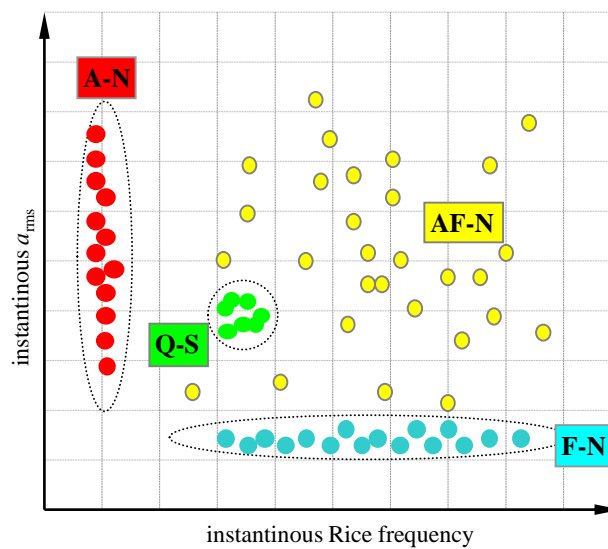

Figure 3. The idea of interpreting the results of short-time parameterisation of vibrations; a representation of various vibration signal types on the $R_f - a_{rms}$ plane:
A-N non-stationary amplitude; F-N non-stationary frequency, Q-S quasi-stationary signal, AF-F non-stationary signal in amplitude and frequency terms
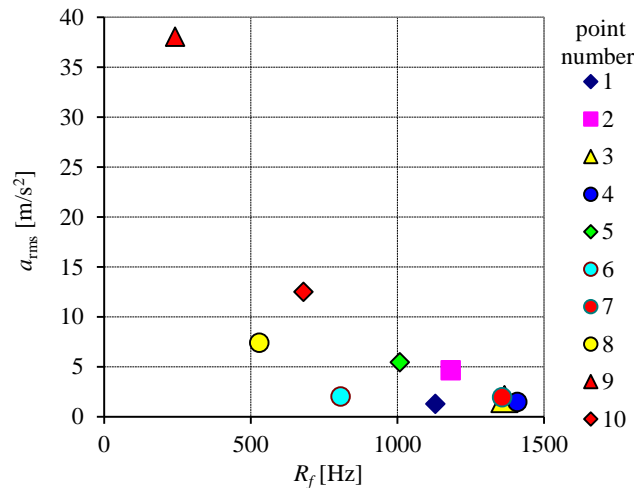
Figure 4. Results of acceleration parameterisation on the $R_f - a_{rms}$ plane, averaged values for 20 cycles of machine operation [4]

The results shown in Figure 4 allow one to estimate which subassemblies are characterized by the highest vibroactivity. The results also allow one to determine the average vibration frequency. Three subassemblies can be pointed out: cardboard bender (no. 9) pneumatic clamp (no. 10) and guide (no. 8) for which reduction of vibration levels may be considered. Signal parameterisation results (Table 1) are helpful in this aspect. The results are supplemented with acceleration peak values a_{peak} and crest factors k.

Table 1. The results of parameterization of vibration accelerations (frequency band up to 2.5 kHz) for 10 operation cycles of the FTHT6 former (approx. 20 s)

Measure [unit]	measurement point number									
	1	2	3	4	5	6	7	8	9	10
$\breve{a}_{rms}$ [m/s^2]	1.3	4.6	1.7	1.5	5.4	2.0	1.9	7.4	38.1	12.5
a_{peak} [m/s^2]	15.8	59.1	20.9	53.2	45.5	16.1	46.2	168.6	810.0	451.9
k [−]	12.5	12.7	12.0	36.3	8.4	8.0	24.0	22.8	21.3	36.2
$\breve{R}_f$ [Hz]	1130	1182	1365	1409	1008	806	1358	529	241	680

An example of a graphic representation of the short-time parameterisation of vibration accelerations on the $R_f - a_{rms}$ plane is shown in Figure 5.
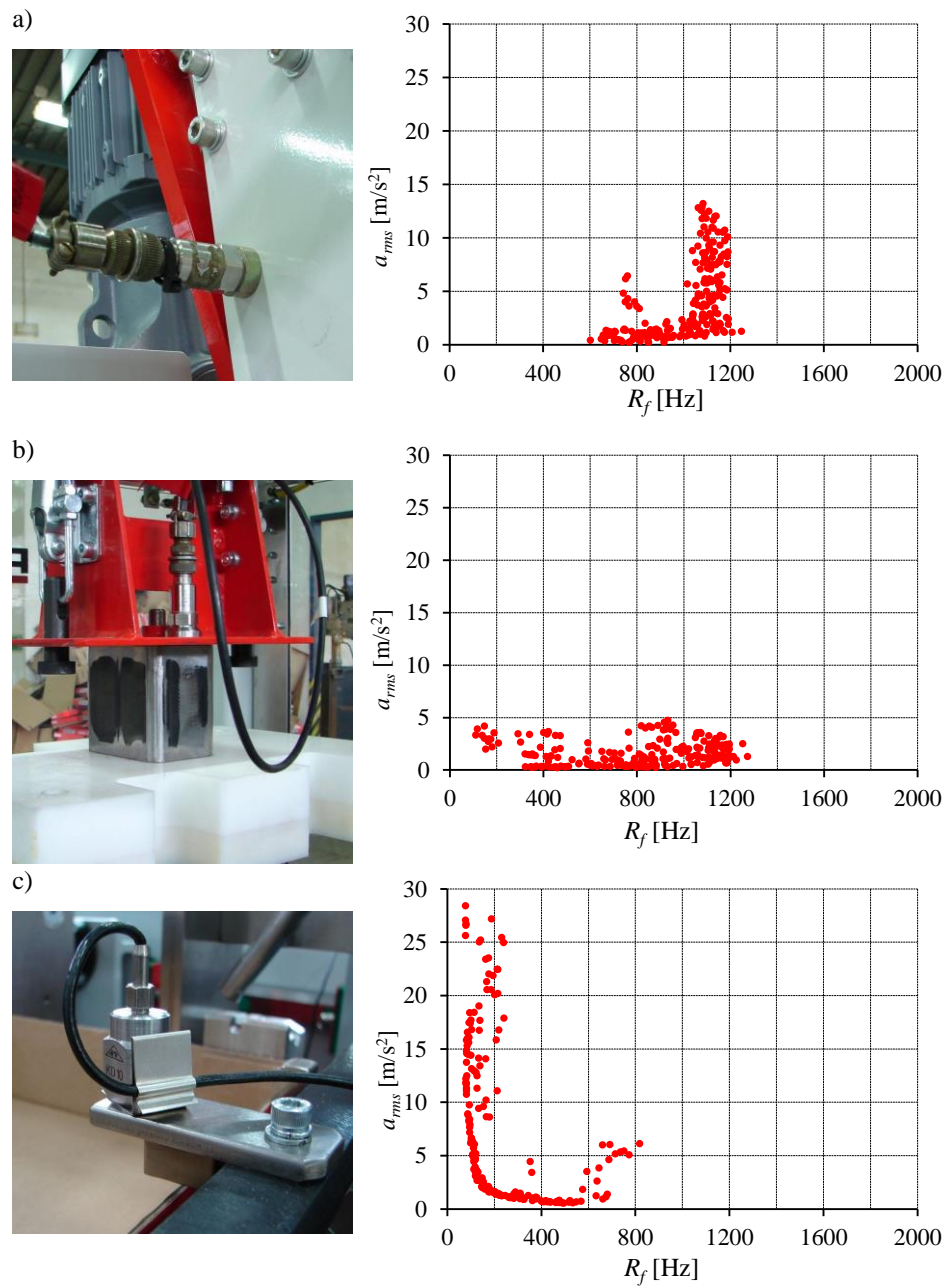
Figure 5. Example results of parametrisation of accelerations on the $R_f - a_{rms}$ plane;
a) punch gearmotor base b) punch c) cardboard bender [4]

A gearmotor is a device consisting of an electric motor and a gearing. The specificity of vibrations generated by the gearmotor is shown in Figure 5 a. Non-stationarity in both the amplitude and frequency terms is visible there. The cyclical start of this subassembly causes an increase in instantaneous $a_{\mathrm{rms}}(\tau)$ values as well as instantaneous $R_f(\tau)$ values. It should be noted that $R_f(\tau)$ takes into account all signal components in the considered frequency band. They are related to the rotation frequency, the gear meshing frequency and its superharmonics as well as components from magneto-electric phenomena (magnetostriction). In the case of the cardboard bender (Fig. 5 c), a non-stationarity in the amplitude terms is mainly visible. This is due to the cyclical activation of this subassembly (natural frequency around 75 Hz, see Fig. 2). The vibration acceleration signal recorded on the punch (Fig. 5 b) is non-stationary in the frequency terms, which is indicated by the large variability of $R_f(\tau)$ with only slight changes in $a_{\mathrm{rms}}(\tau)$.

The analysis of changes in the averaged values of $\check{R}_{f,}$ i $\check{a}_{\mathrm{rms}}$ as a function of machine capacity is important at the stage of testing the prototype of the former. One can identify subassemblies for which increased capacity changes the nature and intensity of vibrations. This type of information can be premises for optimizing the machine design.
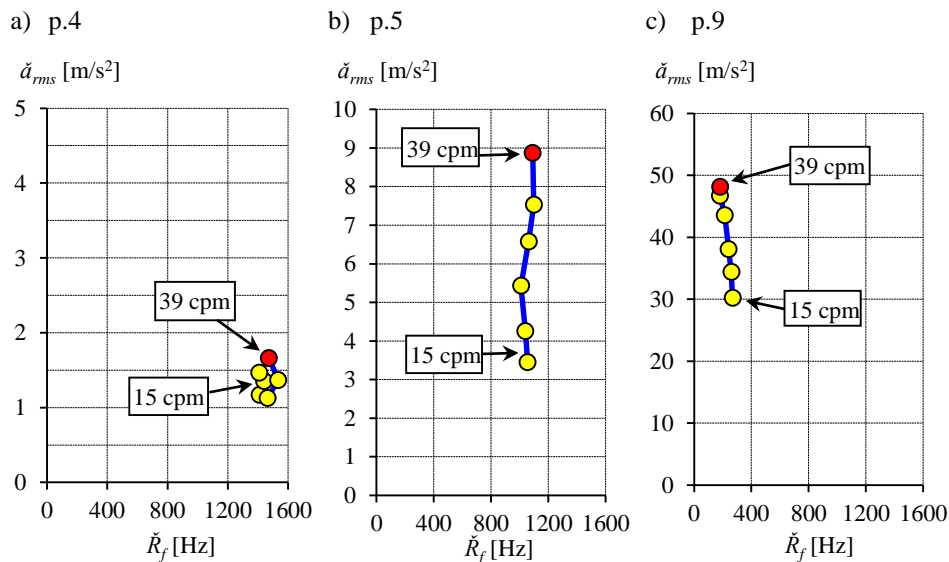
a) p.4   b) p.5   c) p.9

Figure 6. The change in the position of the result of the parameterisation of vibration accelerations on the $R_f - a_{\mathrm{rms}}$ plane resulting from the increase in machine capacity from 15 to 30 cycles per minute (cpm) a) gearmotor base b) punch guide c) cardboard bender [4]

Based on the images in Figure 6, it can be stated that an increase of the capacity of the former:
- has no significant effect on the vibration generated by the punch gearmotor (Fig. 6a),
- causes an increase in the vibration intensity of the punch guide and slightly changes the spectral composition (shift of $\check{R}_f$ towards higher frequencies, Fig. 6b)
- causes an increase in the vibration intensity of the cardboard bender and a decrease in $\check{R}_f$ due to the greater energy share of the subassembly's own frequency. This is due to the shortening of the time interval between successive excitations of the subassembly to vibrate.

5. Conclusions

The graphic representation of the $R_f(\tau)$, $a_{rms}(\tau)$ results on the $R_f - a_{rms}$ plane in the short-time terms gives information about the nature of signal instability in both amplitude and frequency terms as well as the intensity of vibrations of individual subassemblies.

The averaged values $\check{R}_f$ and $\breve{a}_{rms}$ obtained for a new machine should be treated as reference values in the vibration monitoring process. Changing the location of the point specified by $\check{R}_f$ and $\breve{a}_{rms}$ on the $R_f - a_{rms}$ plane during operation will be a signal of a change in the technical condition of the monitored subassembly. The way the results are displayed enables simultaneous monitoring of many subassemblies of the machine. The proposed method can be used to monitor complex machines with many subassemblies and drive units with different kinds of working movement.

This method can be used at the stage of machine prototypes testing as an effective tool for detection of subassemblies that increase vibroactivity along with the increase of machine capacity.

Acknowledgment

References

1. ISO 10816-1:1995, *Mechanical vibration – Evaluation of machine vibration by measurements on non-rotating parts – Part 1: General guidelines*.
2. ISO 20816-1:2016, *Mechanical vibration – Measurement and evaluation of machine vibration – Part 1: General guidelines*.
3. P. Czop, W. Staszewski, A. Jabłoński, *Parametric early warning diagnostic method for rotating machinery diagnostics*, Diagnostyka, **17**(4) (2016) 49 – 58.
4. R. Barczewski, B. Jakubek, Project: *Modular SRP packaging production system, :task 1: Vibration and noise studies*, Technical Report No r475_2019, Poznan University of Technology, 2019.
5. S. Qian, D. Chen, *Joint time frequency analysis: methods and applications*, Prentice-Hall, Upper Shaddle River, 1996.
6. C. Cempel, *Diagnostically oriented measure of vibroacoustical processes*, Journal of Sound and Vibration, **73**(4) (1980) 574 – 561.

7. P. Deuszkiewicz, D. Górnicka, *Rice Frequency as a Measure of Damage to the Combustion Engine Valve*, Przegląd Mechaniczny, **4** (2009) (in Polish).

8. F. Inoue, E. Outa, K. Tajima, T. Machiyama, *An Experimental Study on Control Valve Cavitation (1st Report Diagnostics of Cavitation Vibration at High Pressure Reduction and at Low Valve Opening)*, Transactions of the Japan Society of Mechanical Engineers Series B, **53**(485) (1987) 127 – 137.

9. C. Cempel, *Principles of vibroacoustical diagnostics of machines*, WNT, Warszawa 1982 (in Polish)

10. R. Barczewski, *Short time Rice frequency analysis (STRFA) a method of the time variant vibration signal analysis*, Vibrations in Physical Systems, **22** (2006) 79 – 82.

11. R. Barczewski, *Diagnostic oriented methods of short time processing of vibroacoustic signals*, Publishing House of Poznan University of Technology, Poznań 2013 (in Polish).

12. J. Bendat, A. Piersol, *Random data: Analysis and Measurement Procedures*, John Wiley & Sons, New York 1986,

13. M. Barczewski, R. Barczewski, T. Sterzynski, *Dynamic pressure analysis as a tool for determination of sharkskin instability by extrusion of molten polymers*, Journal of Polymer Engineering, **32** (2012), doi:10.1515/polyeng-2011-0157.

14. T. Plazenet, T. Boileau, C. Caironi, B. Nahid-Mobarakeh, *Signal processing tools for non-stationary signals detection*, 2018 IEEE International Conference on Industrial Technology (ICIT), Lyon, 2018, 1849 – 1853.